

Electromagnetic Processes at the LHC:
Nuclear Parton Distributions from Deep Inelastic Pair Production
and Exclusive Photoproduction of Single W Bosons

Inauguraldissertation

zur
Erlangung der Würde eines Doktors der Philosophie
vorgelegt der
Philosophisch-Naturwissenschaftlichen Fakultät
der Universität Basel

von

Ute Dreyer
aus
Deutschland



Basel, 2007

Genehmigt von der Philosophisch-Naturwissenschaftlichen Fakultät
auf Antrag von
PD Dr. K. Hencken, Prof. Dr. G. Baur und Prof. Dr. D. Trautmann

Basel, den 26. Juni 2007

Prof. Dr. Hans-Peter Hauri
Dekan

Abstract

Ultra-peripheral collisions at ion colliders, such as the Large Hadron Collider (LHC) at CERN, offer the possibility to study electromagnetic processes at hitherto unexplored energies. In the framework of the equivalent photon approximation (EPA), where relativistic charged particles are treated as beams of equivalent photons, the collisions of ions can be used to study two-photon ($\gamma\gamma$ collisions) or photonuclear processes (γp and γA collisions). This thesis contains two studies of processes which might be observed at the LHC. The main purpose in these studies is the estimation of the total rates of these processes at LHC energies and the investigation of their event signature, in order to find out whether an observation of these processes is feasible and what can be learnt from them.

Our first study [1] addresses the production of lepton pairs in heavy ion collisions in the region of large momentum transfer of one of the photons and the feasibility to study the quark content of nucleons and nuclei from this process. This is particularly interesting with regard to how the quark parton distributions of nucleons change when affected by nuclear modifications. However, to be able to learn from this process, it is important to isolate it experimentally. This means, one has to find a way to distinguish the deep inelastic scattering (DIS) process from possible background, mainly coming from the elastic (doubly coherent) two-photon pair production. To this purpose we calculate the cross section for two-photon lepton pair production in relativistic heavy ion collisions in the region of large momentum transfer of one of the photons in a plane wave Born approximation. We compare differential cross sections from this calculation to those of a calculation of doubly coherent pair production. We find the elastic contribution to be dominant at small momentum transfers of the photons. However, at transverse momenta of the leptons of above ~ 1 GeV the two contributions become comparable in size. Furthermore, the two processes show distinct event signatures: In the doubly coherent process, the leptons are produced back-to-back in the transverse plane, i. e. having equal transverse momenta. In the deep inelastic contribution, in contrast, the leptons show an asymmetric distribution of their transverse momenta. One lepton is produced with relatively large transverse momentum, reflecting the Q^2 distribution of the photon, while the transverse momentum distribution of the other lepton peaks at small transverse momenta.

Furthermore, lepton pair production from deep inelastic scattering in heavy ion collisions can be related to deep inelastic lepton scattering off nuclei by means of a combination of the equivalent photon approximation and photon splitting into a lepton pair. This provides an intuitive picture of the process and moreover simplifies the calculation considerably. In order to test these approximations, we calculate differential cross sections as functions of various kinematic variables in the equivalent photon approximation (EPA) and the equivalent lepton approximation (ELA) and compare the results to those of the full calculation. As result, the EPA is found to be satisfying, whereas the ELA consistently overestimates the results from the full calculation. Despite the quantitative failure of the ELA, our results confirm that it may still serve as a qualitative picture of the process.

Furthermore, we include two parameterizations which account for nuclear modifications in our full calculation in order to study their effect on the cross section. We find the differential cross section as function of the rapidity to be most sensitive to the differences between the two sets.

In our second study [2], we are concerned with the exclusive photoproduction of single W bosons in p-p or p-A collisions, where the proton is converted into a neutron, which proceeds in forward direction. This process is very sensitive to the coupling of two W bosons and a photon and thus offers the possibility to test this coupling for contributions which go beyond the Standard Model provided a reasonable rate of events can be achieved.

This study aims to estimate the total rate of events for this process at the LHC. To this purpose,

we calculate the cross section for real photoproduction of single W bosons and cross-check the results with those of former studies of this process. We extend those studies by including, in addition, a weak magnetic form factor. Convolving the photoproduction cross sections with the equivalent photon spectra of ions and protons yields the cross sections for p-p and p-A collisions. We estimate the rates of events expected at the LHC from this process within the Standard Model. Furthermore, we compare different choices of the (almost unknown) timelike weak form factors and examine how they affect the sensitivity of the total cross section to the triple gauge boson coupling.

Since the W decays almost immediately, it can only be measured through its decay products. The most important decay channel, in the sense that it has experimentally the cleanest signal, is the decay into leptons. We include the decay of the W into a light anti-lepton (e^+ or μ^+) and the corresponding neutrino into our calculations and calculate differential cross sections as functions of the energies, rapidities, and transverse momenta of all final state particles in this process. Based on the rate predicted for the p-p case, we conclude that an observation of this process should be possible in the very high-luminosity runs at the LHC.

Contents

1. Introduction	1
1.1. Ultra-Peripheral Collisions at the LHC	1
1.2. Motivation for the Study of Deep Inelastic Pair Production in UPCs	2
1.3. Motivation for the Study of Exclusive Photoproduction of Single W Bosons	2
1.4. Overview	3
2. Composite Particles	5
2.1. Introduction	5
2.2. The Electromagnetic Structure of Nucleons	5
2.3. The Electromagnetic Structure of Nuclei	12
2.4. The Weak Structure of Nucleons	16
3. Equivalent Particle Approximations	19
3.1. Introduction	19
3.2. Electron and Photon Splitting Functions	19
3.3. Equivalent Photon Approximation for Extended Objects	20
3.3.1. Elastic Equivalent Photon Spectrum of Nuclei	21
3.3.2. Elastic Equivalent Photon Spectrum of Protons	22
3.4. Two-Step Approximations	23
3.4.1. Deep Inelastic Equivalent Photon Spectrum of Protons	23
3.4.2. Equivalent Leptons in Nuclei	24
4. Lepton Pair Production from DIS	27
4.1. Introduction	27
4.2. Full Calculation	30
4.2.1. The Matrix Element of Two-Photon Pair Production in Heavy Ion Collisions	30
4.2.2. Results for Elastic and Deep Inelastic Pair Production	33
4.2.3. Nuclear Modifications	40
4.3. Lepton Pair Production from DIS in EPA and ELA	43
4.4. Conclusions	47
5. Single W Production at LHC	49
5.1. Introduction	49
5.2. Photoproduction of W Bosons	50
5.3. W Boson Production in p-p and p-A Collisions	56
5.4. Decay of W Bosons	64
5.5. Conclusions	70

A. Monte Carlo Event Generator	73
A.1. Motivation	73
A.2. Monte Carlo Event Generation	74
A.3. Pair Production in the Atomic Field	76
A.4. Conclusions	82
B. Monte Carlo Integration	87
C. Phase Space Generation	91
Bibliography	95
Curriculum Vitae	99

Introduction

1.1 Ultra-Peripheral Collisions at the LHC

At the Large Hadron Collider (LHC) at CERN protons and heavy ions will collide at hitherto inaccessible energies. The primary purpose of this collider is the search for new heavy particles, such as the higgs or supersymmetric particles, as well as the search for new physics beyond the Standard Model. Moreover, in the collision of heavy ions, one is looking for the formation and signature of a new state of hadronic matter, the Quark Gluon Plasma. The main focus in these searches will be on central collisions, i. e. collisions, where the distance between the centers of the colliding particles - the impact parameter b - is smaller than the sum of their radial extensions $b < R_1 + R_2$. Processes in these central collisions are mainly due to the strong interaction and have large cross sections. Furthermore, they are characterized by a high multiplicity of final state particles.

However, there is a main difficulty in understanding the interactions in these central collisions, since one has to deal with two objects with a complex internal structure, which has never been probed at such high energies before. For some studies this problem can be overcome by restricting oneself to more distant collisions. At impact parameter $b > R_1 + R_2$ the protons or heavy ions, respectively, interact only via the well-understood, long-range electromagnetic force. Relativistic nuclei generate strong electromagnetic fields which are equivalent to a flux of quasi-real photons. These nuclei can be treated in the equivalent photon approximation (EPA), which is described in detail in chapter 3 of this work. In the EPA the region where the nuclei interact strongly can even be excluded by using impact parameter dependent equivalent photon spectra. Thus, in these distant collisions the nuclei interact via photons and basically two types of interactions may occur. The photon from one nucleus strikes the other nucleus, these processes are referred to as photonuclear (γ -p or γ -A collisions). Alternatively, in pure electromagnetic processes, photons from both nuclei collide ($\gamma\gamma$ collisions).

These distant collisions are often referred to as ultra-peripheral collisions (UPCs). As opposed to central collisions, both nuclei (in $\gamma\gamma$ collisions) or one nucleus (in γ -p and γ -A collisions) stay intact and the final state multiplicity is, in general, much lower. UPCs at the LHC provide the possibility to study many interesting processes in new energy ranges. In particular, they are very suitable for the study of the nuclear parton structure in γ -A collisions, since photons are a clean and well-understood probe. Furthermore, they may as well contribute to the search for beyond Standard Model physics. An overview over the physics potential in UPCs can be found in [3, 4]. In this thesis, two processes will be introduced, which can be studied in UPCs at the LHC and which contribute to the understanding of nuclear structure, when probed at high energies, and electroweak couplings among gauge bosons.

1.2 Motivation for the Study of Deep Inelastic Pair Production in UPCs

For the interpretation of data from central hadron collisions, the understanding of the strong interaction dynamics underlying these processes is crucial. In particular, the parton distribution functions, which describe the momentum distribution of quarks and gluons in free nucleons (PDFs) or heavy ions (nPDFs) are important ingredients for the prediction of processes in central collisions. These parton distributions are, in principle, known from fixed target and electron-proton collider experiments. However, measurements of photon-induced processes in UPCs at the LHC could greatly expand the kinematic range, especially in the regime of small Bjorken x . Furthermore, nuclear parton distribution functions (nPDFs) are an interesting topic on their own. For example, it is not yet fully understood, how the PDFs change in the nuclear medium and what the underlying mechanisms are. Especially not in the very low x -regime which can be probed at the LHC. By comparing data from processes in γ -p and γ -A collisions, nuclear medium effects on the PDFs can be studied.

The conventional way to study nuclear structure is through deep inelastic lepton scattering. As the leptons themselves do not have an internal structure they provide a very clean probe of the structure of composite particles. In addition, the electromagnetic coupling is weak and the electromagnetic interaction can be treated in perturbation theory to very high precision. In order to study deep inelastic lepton scattering at ion colliders, we regard lepton pair production in UPCs. The main contribution to the lepton pair production cross section comes from the two-photon process where both photons are emitted coherently by the ions ($\gamma\gamma$ collisions). The cross section for this process is huge and it has been studied extensively in the past [5, 6, 7, 8]. However, to be able to probe the quark and gluon degrees of freedom of the proton or heavy nucleus, we regard those pair production events with large momentum transfer of one of the photons. Instead of applying the equivalent photon approximation to both ions, we use another equivalent particle approach. We combine the equivalent photon approximation (EPA) with photon splitting into a pair of light particles. Both methods and their combination, the equivalent lepton approximation (ELA), are described in chapter 3 of this work. In this approach, one photon is emitted coherently by a heavy ion and subsequently splits into a pair of leptons. One of these leptons interacts with the proton (γ -p) or the other heavy ion (γ -A) via deep inelastic scattering and obtains a large transverse momentum. The second lepton acts as a spectator to this process, proceeding in forward direction, i. e. with very small transverse momentum.

Concerning this process several questions arise. Does the picture provided by the ELA hold? To what extent are the approximations involved valid? In which kinematic regions can we expect viable amounts of events? Is the study of nuclear structure feasible from this process? How can deep inelastic pair production events be distinguished from the overwhelming background of doubly coherent pair production events?

In chapter 4 we will address these questions by studying deep inelastic pair production in relativistic heavy ion collisions.

1.3 Motivation for the Study of Exclusive Photoproduction of Single W Bosons

The Standard Model of particle physics has been tested extensively and has proven to be very successful in the recent years. Nevertheless, it has too many free parameters to be a truly fundamental theory. Furthermore, it fails to predict the number of particles or families. For these reasons and because it does not incorporate gravity, it is believed to be only the low energy manifestation of a more fundamental theory, which unveils itself at an energy scale Λ , which is at least around 1 TeV. This high-scale physics can be seen as well in the couplings among particles.

In particular, the couplings among gauge bosons, which are due to the non-Abelian nature of the $SU(2) \times U(1)$ gauge symmetry, provide an ideal testing ground for physics beyond the Standard Model. For one thing, up to now they could not yet be tested very well experimentally. This is due to the small cross sections of processes involving electroweak interactions. For another thing, the gauge boson coupling strengths are strongly constrained by gauge invariance and are therefore very sensitive to deviations from the Standard Model. The triple gauge boson couplings (γWW and ZWW), for example, are very sensitive to the anomalous magnetic moment of the W boson κ_W , which is very well defined in the Standard Model ($\kappa_W = 1$ at tree level), but its value is in principle free in composite models. Electroweak processes have been studied e. g. at HERA, but suffer from low statistics. As already mentioned above, the LHC is a high luminosity $\gamma\gamma$ and γ -A/p collider with an energy reach far beyond other existing machines. Thus an improvement in precision can be expected from measurements at the LHC.

W^+W^- pair production in $\gamma\gamma$ collisions and W^+ production from a proton in γ -p collisions are both sensitive to the triple gauge boson couplings. W pair production is sensitive to both, the $WW\gamma$ and the WWZ coupling, and therefore suffers from the drawback that the contributions of the two couplings have to be disentangled. In contrast, the single W photoproduction is only sensitive to the $WW\gamma$ coupling and thus provides the opportunity for an independent measurement of this coupling. The W boson can either be produced in the exclusive process $\gamma + p \rightarrow W + n$ or in the inclusive process $\gamma + p \rightarrow W + X$. The inclusive process has been studied theoretically by Baur et al. [9, 10] and experimentally by Breitweg et al. [11] at HERA. Baur et al. predicted a cross section of ~ 1 pb at HERA energies, which was confirmed by the measurements of Breitweg et al.. The cross section for this process at the LHC is estimated by Piotrkowski [12] to be ~ 40 pb. However, in this work, we will focus on the exclusive process since it provides a rather unique signature having a neutron in forward direction accompanied by the signature of the leptonic decay of the W boson, a lepton with large transverse momentum peaked at 40 GeV, as well as a large missing transverse momentum from the unobserved neutrino. In chapter 5 of this work, we investigate the feasibility of measuring the $WW\gamma$ vertex via the exclusive photoproduction of single W bosons in pp and pA collisions at the LHC.

1.4 Overview

This thesis is arranged as follows. Chapters 2 and 3 serve as an introduction into the most important tools, which we will apply in chapters 4 and 5 to the investigation of pair production from deep inelastic scattering and to the calculation of the cross section of exclusive photoproduction of W bosons.

Form factors have to be employed when photons or weak gauge bosons couple to composite particles. They account for the structure of these particles. In chapter 2 we give an introduction into the concepts of electromagnetic and weak form factors, as well as an overview over the methods to measure them at various scales of momentum transfer.

Nuclei in high energy collisions are known to generate a large flux of photons. In the equivalent photon approximation they can be replaced by a spectrum of equivalent photons. Especially in UPCs the nuclei interact only via the electromagnetic force, i. e. through photons. These photons are mainly emitted coherently and with very small momentum transfers. In such a situation, the equivalent photon approximation is valid and can be used to simplify cross sections in p-p, p-A, or A-A collisions to $\gamma\gamma$, γ -p, or γ -A collisions. In chapter 3 we introduce the equivalent photon approximation for various particles, i. e. from point-like particles, like leptons and quarks, over nucleons to nuclei. Furthermore, we explain how the equivalent particle concept can be extended to other particles as well. For example, a photon can split into a pair of light particles. Finally, we give two examples of combinations of these approximations, which will be employed in chapters 4 and 5.

After having established the foundation for the calculation of high energy cross sections in these two chapters, we proceed introducing two studies of processes, which can be studied in UPCs at the LHC.

In chapter 4 we aim to investigate the feasibility to probe the structure of nuclei in lepton pair production from deep inelastic scattering in UPCs. To this purpose, we calculate the cross section for two-photon lepton pair production in the region of large momentum transfer of one of the photons in a plane wave Born approximation. Deep inelastic lepton pair production in heavy ion collisions can be related to deep inelastic lepton scattering off nuclei by the use of the equivalent lepton approximation (ELA), which is a combination of the equivalent photon approximation and photon splitting. In order to test the validity of these approximations and the intuitive picture, they provide, we calculate differential cross sections as functions of various kinematic variables in the EPA and the ELA and compare them to the results of a full calculation. Furthermore, we include two parameterizations which account for nuclear modifications to the PDFs in our full calculation in order to study their effect on the cross sections.

In chapter 5 we study the exclusive photoproduction of single W bosons from a proton. First of all, we want to estimate the total cross section of this process in order to find out, whether enough W bosons are produced to be measured. First, we calculate the cross section for (real) photoproduction of single W bosons for various photon energies and cross-check our results against those of Fearing et al. [13, 14], who have calculated this cross section with a smaller W boson mass in mind. Next, we extend these calculations by additionally including a weak magnetic form factor and by employing the correct W boson mass. To obtain predictions for the cross section in p-p and p-A collisions at the LHC we convolve the photoproduction cross section with the equivalent photon spectra of protons and ions. Furthermore, we show how the choice of the timelike weak form factor affects the sensitivity of the total cross section to the anomalous magnetic moment of the W boson. Since it is crucial to identify the few events that occur as efficiently as possible, we include the subsequent decay of the W into leptons in our calculations as well. Finally, we present differential cross sections as functions of the energies, rapidities, and transverse momenta of all final state particles in this process.

As a byproduct of our studies of pair production from two-photon processes in chapter 4, we were able to develop a Monte Carlo event generator for electron pair production in the field of an atom. This event generator can be used in the simulation of low energy attenuation experiments. In appendix A we describe how Monte Carlo event generators are programmed in general as well as in this particular case.

Composite Particles - from Nucleons to Nuclei

2.1 Introduction

The couplings of gauge bosons to composite particles, such as nucleons and nuclei, are an important ingredient in the calculation of cross sections of processes occurring in hadronic collisions. The constituents of composite particles are held together by the strong interaction. Understanding how the structure and interactions of hadrons arise from the underlying theory of Quantum Chromodynamics (QCD) is one of the central challenges of contemporary nuclear physics and beyond the scope of this work. A convenient way, however, to handle the interaction of composite particles is their parameterization in terms of phenomenological form factors, i.e. scalar functions, which can be determined by experiment. The conventional way to gain information on the structure and couplings of extended objects is by scattering, where structureless objects, such as leptons, are used as projectiles.

This chapter serves as an introduction into the concepts of electromagnetic and weak form factors, in terms of which the elastic and inelastic scattering of nucleons and nuclei is commonly expressed. In section 2.2 the calculation of scattering amplitudes and cross sections is described in general and for the example of electron scattering off structureless particles in particular. Furthermore, the application of form factors in various regions of energy and momentum transfer is introduced using electron scattering from nucleons as an example.

The scattering off nuclei is in principle described in a similar way as the scattering off nucleons, but new effects may occur due to the two-stage composite nature of nuclei: Nuclei consist of nucleons which in turn have quarks and gluons as constituents. Section 2.3 is devoted to the description of some of these effects.

In section 2.4 we explain how the weak coupling of W bosons and nucleons can be expressed in terms of weak form factors, how it is simplified, and how the remaining form factors can be determined from neutrino scattering experiments.

Some difficulties emerge when using the couplings outlined in this chapter. For example, in chapter 5 the weak form factors are required far into the timelike region, where they are hardly known and the electromagnetic coupling is needed for off-shell nucleons. These problems will be addressed as they arise in the relevant chapters.

2.2 The Electromagnetic Structure of Nucleons

This section introduces the calculation of scattering amplitudes and cross sections, as well as the description of composite particles in terms of form factors using electron scattering as an example. Historically, the first indication of a composite nature of nucleons came from the measurement of their magnetic moments. The results of these measurements were not consistent with the

expectations for charged, point-like Dirac particles.

Scattering structureless particles, electrons for example, off nucleons is the cleanest and most effective way of gaining information on their structure. Due to the smallness of the electromagnetic coupling, the cross section of electron scattering is dominated by the one photon exchange diagram (see Fig. 2.1). The nucleon structure is probed by the exchanged virtual photon with momentum q . The resolving power of this probe is given by Heisenberg's uncertainty principle: $\lambda \sim \frac{\hbar}{Q}$. Thus the degree of structure revealed by electron scattering increases with the momentum transfer squared $Q^2 = -q^2 > 0$.

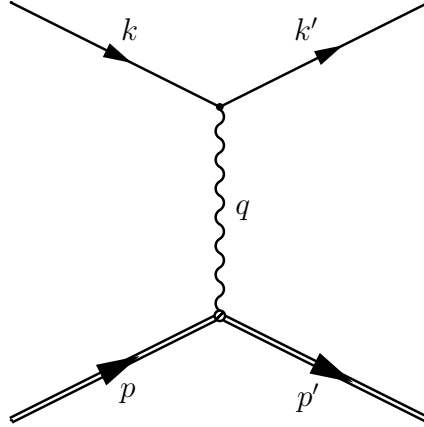


Figure 2.1: One photon exchange diagram for lepton-nucleon scattering.

Calculation of Cross Sections

The total cross section for the scattering of two incoming particles into some set of n outgoing particles is given by

$$\sigma = \frac{1}{F} \int |\mathcal{M}|^2 dPS_n \quad (2.1)$$

with F being the flux of the incoming particles and dPS_n the phase space of the n final particles given by

$$dPS_n = \prod_{i=3}^n \left(\frac{d^3 p_i}{2\epsilon_i (2\pi)^3} \right) N_i (2\pi)^4 \delta^4 \left(p_1 + p_2 - \sum_{i=3}^n p_i \right). \quad (2.2)$$

ϵ_i is the energy of the i th particle, p_i its momentum, and the factor N_i depends on the normalization of the Dirac spinors:

$$N_i = \begin{cases} 1 & \text{for } \sum_s \bar{u}(p)u(p) = 2m \\ 2m & \text{for } \sum_s \bar{u}(p)u(p) = 1. \end{cases} \quad (2.3)$$

A very efficient way to integrate over the phase space (2.2), especially for complicated many particle final states, is given in the textbook of Byckling and Kajantie [15] and we outline this method in the appendix C. The matrix element \mathcal{M} in equation (2.1) contains the dynamics of the interaction of the particles and can be computed by drawing the relevant Feynman diagrams and evaluating them using the standard Feynman rules, see e.g. [16, 17, 18].

Scattering from a Point-like Spin- $\frac{1}{2}$ Particle

The calculation of elastic electron scattering from a point-like spin- $\frac{1}{2}$ particle N of mass M and charge e (see Fig. 2.2) will serve as an example to illustrate the calculation of matrix elements. These results can be found in various textbooks, such as [19, 20]. The amplitude can be divided

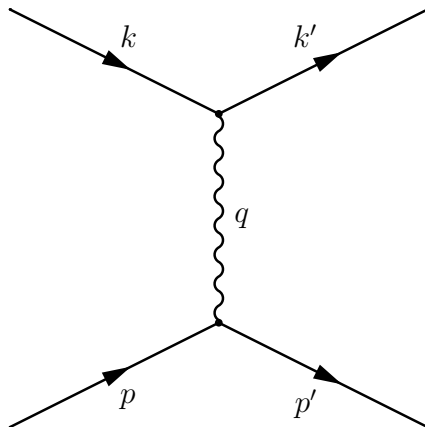


Figure 2.2: One photon exchange diagram for the scattering from a point-like spin- $\frac{1}{2}$ particle.

into three parts:

- (i) the electromagnetic current of the electron: j_e^μ ,
- (ii) the electromagnetic current of particle N : J_μ^N ,
- (iii) and the exchanged photon of momentum q .

The current matrix elements are given by

$$\langle l(k') | j_e^\mu | l(k) \rangle = \bar{u}(k') \gamma^\mu u(k) e^{-i(k-k')x} \quad (2.4)$$

for the electron and by

$$\langle N(p') | J_\mu^N | N(p) \rangle = \bar{u}(p') \gamma_\mu u(p) e^{-i(p-p')x} \quad (2.5)$$

for the Dirac particle N , where the normalization of the spinors is

$$\sum_{s=\pm\frac{1}{2}} u_s(p) \bar{u}_s(p) = \not{p} + M. \quad (2.6)$$

For unpolarized scattering the spin average over the squared matrix element gives

$$|\mathcal{M}|^2 = \frac{e^4}{q^4} \frac{1}{4} \sum_{\text{spins}} |\bar{u}(k') \gamma^\mu u(k) \bar{u}(p') \gamma_\mu u(p)|^2 = \frac{e^4}{q^4} L^{\mu\nu} N_{\mu\nu} \quad (2.7)$$

with the spin-averaged tensors for the electron

$$L^{\mu\nu} = \frac{1}{2} \text{Tr} [(\not{k}' + m) \gamma^\mu (\not{k} + m) \gamma^\nu] = 2 [k^\mu k'^\nu + k^\nu k'^\mu - g^{\mu\nu} (k \cdot k' - m^2)] \quad (2.8)$$

and for particle N

$$N_{\mu\nu} = \frac{1}{2} \text{Tr} [(\not{p}' + M)\gamma_\mu(\not{p} + M)\gamma_\nu] = 2 [p^\mu p'^\nu + p^\nu p'^\mu - g^{\mu\nu}(p \cdot p' - M^2)] \quad (2.9)$$

Using $p' = p + k - k'$ and $q = k - k'$ we obtain

$$L^{\mu\nu} N_{\mu\nu} = 8 [2(k \cdot p)(k' \cdot p) + (k \cdot k')(q \cdot p - M^2) + m^2(-2q \cdot p + M^2)] . \quad (2.10)$$

For high energy electron scattering the electron mass is negligible, $m \approx 0$:

$$L^{\mu\nu} N_{\mu\nu} = 8 [2(k \cdot p)(k' \cdot p) + (k \cdot k')(q \cdot p - M^2)] . \quad (2.11)$$

In the rest system of particle N the differential cross section can be written in the form

$$\frac{d\sigma}{d\Omega} = \frac{\alpha^2}{4\epsilon^2 \sin^4 \frac{\vartheta}{2}} \frac{\epsilon'}{\epsilon} \left(\cos^2 \frac{\vartheta}{2} - \frac{q^2}{2M^2} \sin^2 \frac{\vartheta}{2} \right) \delta \left(\nu + \frac{q^2}{2M} \right) \quad (2.12)$$

with $\nu = \epsilon - \epsilon'$ the energy transfer, where ϵ is the energy of the incoming electron, ϵ' the energy of the scattered electron, and ϑ the electron scattering angle. The factor $\frac{\epsilon'}{\epsilon}$ in equation (2.12) arises from the recoil of the target.

Elastic Scattering from a Structured Spin- $\frac{1}{2}$ Particle

The current matrix element in equation (2.5), however, is not appropriate to describe particles with an extended structure. Thus, γ_μ in J_μ^N has to be replaced by a more general Lorentz four-vector Γ_μ . The most general form for the nucleon current matrix element for on-shell nucleons is constrained by current conservation and Lorentz structure to

$$\langle N(p') | J_\mu^N(0) | N(p) \rangle = \bar{u}(p') \Gamma_\mu u(p) = \bar{u}(p') \left[F_1(Q^2) \gamma_\mu + i \kappa_N F_2(Q^2) \sigma_{\mu\nu} \frac{q^\nu}{2M} \right] u(p) \quad (2.13)$$

with κ_N the nucleon magnetic moment

$$\kappa_p = 1.79 \quad (2.14)$$

$$\kappa_n = -1.91 . \quad (2.15)$$

Current conservation $\partial_\mu J^\mu = 0$ rules out terms proportional to $(p - p')_\mu$, while terms involving $(p + p')_\mu$ can be expressed through the other terms in equation (2.13) by means of the Gordon decomposition

$$\bar{u}(p') \gamma_\mu u(p) = \frac{1}{2m} \bar{u}(p') \left((p' + p)_\mu + i \sigma_{\mu\nu} (p' - p)_\nu \right) u(p) . \quad (2.16)$$

$F_{1|2}(Q^2)$ are the Dirac and the Pauli form factor, respectively. Another set of often used form factors are the Sachs form factors:

$$G_E^N(Q^2) = F_1^N(Q^2) - \tau \kappa_N F_2^N(Q^2) \quad (2.17)$$

$$G_M^N(Q^2) = F_1^N(Q^2) + \kappa_N F_2^N(Q^2) \quad (2.18)$$

with

$$\tau = -\frac{q^2}{4M^2} = \frac{Q^2}{4M^2} \quad (2.19)$$

and their inversion

$$F_1^N(Q^2) = \frac{G_E^N(Q^2) + \tau G_M^N(Q^2)}{1 + \tau} \quad (2.20)$$

$$F_2^N(Q^2) = \frac{G_M^N(Q^2) - G_E^N(Q^2)}{\kappa_N(1 + \tau)}. \quad (2.21)$$

The Sachs form factors (2.17) and (2.18) measure the charge distribution (G_E) and the distribution of magnetization (G_M), respectively. Their normalization at $Q^2 = 0$ is given by the nucleon charges and magnetic moments

$$G_E^p(0) = 1 \quad (2.22)$$

$$G_M^p(0) = 1 + \kappa_p = 2.79 \quad (2.23)$$

for the proton and

$$G_E^n(0) = 0 \quad (2.24)$$

$$G_M^n(0) = \kappa_n = -1.91 \quad (2.25)$$

for the neutron. In the Breit frame, where the four momentum of the photon is given by

$$q^\mu = (0, \vec{q}), \quad (2.26)$$

G_E and G_M are the three-dimensional Fourier transforms of the nucleon's charge and magnetic moment density distributions, respectively. Experimentally, the Sachs form factors turn out to be consistent with a dipole fit :

$$G_E^p(Q^2) \approx \frac{G_M^p(Q^2)}{1 + \kappa_p} \approx \frac{G_M^n(Q^2)}{\kappa_n} \approx G_D(Q^2) = \left(1 + \frac{Q^2}{0.71 \text{ GeV}^2}\right)^{-2} \quad (2.27)$$

for Q^2 up to a few GeV^2 .

Inclusive Inelastic Scattering from Nucleons

While elastic scattering identifies the nucleon as a particle with an extended structure by measuring, for example, the charge radius of the proton, nothing can be learned about the nature of its constituents. In order to get an understanding of the detailed structure of the nucleon, it has to be probed with higher resolution by increasing the momentum transfer Q^2 .

The excitation of the nucleon to a series of resonances at invariant masses W of the hadronic final state around $\sim 1 - 2 \text{ GeV}$ provided a second, complementary manifestation of the intrinsic structure of the nucleon. The existence of the nucleon resonances became apparent through a series of pronounced peaks in the electron nucleon scattering cross section as function of the invariant mass W .

At even higher Q^2 , the energy transfer becomes so large, that the nucleon will most likely break up (see Fig. 2.3). Apparently, in this situation the description in terms of $\bar{u}(p')\Gamma_\mu u(p)$ is no longer adequate. The multi-particle final state cannot be described by a single-fermion Dirac spinor u . In inclusive measurements the hadronic final state remains unobserved, this corresponds to summing over all possible final states X in the calculation of the cross section. Thus, the hadron tensor is generalized to

$$W_{\mu\nu} = \frac{1}{4\pi M} \left(\frac{1}{2} \sum_s \right) \sum_X \int \prod_{n=1}^{N_X} \frac{d^3 p_n}{2E_n (2\pi)^3} \quad (2.28)$$

$$\times \sum_{s_n} \langle p, s | J_\mu^\dagger | X \rangle \langle X | J_\nu | p, s \rangle (2\pi)^4 \delta^4 \left(p - q - \sum_n p_n \right).$$

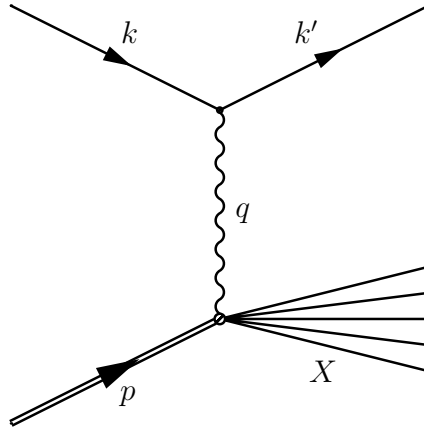


Figure 2.3: Schematic diagram of inelastic electron-nucleon scattering, where the nucleon breaks up.

This hadron tensor contains all possible transitions of the nucleon from its ground state $|p, s\rangle$ to any excited or multi-particle final state $|X\rangle$. Since the actual form of the hadron current $\langle p, s | J_\mu | X \rangle$ is not known, the hadron tensor has to be parameterized. First, it can be split into a symmetric and an antisymmetric part:

$$W_{\mu\nu} = W_{\mu\nu}^S + W_{\mu\nu}^A. \quad (2.29)$$

Lorentz invariance and current conservation give the most general form of the symmetric part in terms of two response functions:

$$W_{\mu\nu}^S = W_1 \left(-g_{\mu\nu} + \frac{q_\mu q_\nu}{q^2} \right) + \frac{W_2}{M^2} \left(p_\mu - \frac{p \cdot q}{q^2} q_\mu \right) \left(p_\nu - \frac{p \cdot q}{q^2} q_\nu \right). \quad (2.30)$$

The antisymmetric part $W_{\mu\nu}^A$ is only of interest for the scattering of polarized electrons on polarized nucleons and we will drop it hereafter. The response functions $W_{1|2}$ depend on two Lorentz invariants: $\nu = p \cdot q/M$ and Q^2 , which are now independent scalars, as opposed to elastic scattering, where $\nu_{el} = \frac{Q^2}{2M}$. The cross section for elastic scattering on a nucleon is recovered for

$$W_1(\nu, Q^2) = \tau G_M^2(Q^2) \delta \left(\nu - \frac{Q^2}{2M} \right) \quad (2.31)$$

$$W_2(\nu, Q^2) = \frac{G_E^2(Q^2) + \tau G_M^2(Q^2)}{1 + \tau} \delta \left(\nu - \frac{Q^2}{2M} \right). \quad (2.32)$$

Deep Inelastic Scattering

For large Q^2 , we enter the regime of deep inelastic scattering, where the electron no longer scatters off the nucleon as a whole, but independently off one of the constituents of the nucleon. In the description of deep inelastic scattering (DIS) processes it is common to replace the response functions $W_{1|2}(\nu, Q^2)$ by the dimensionless structure functions $F_{1|2}(\nu, Q^2)$, i. e. the form factors of the constituents,

$$F_1 = MW_1 \quad (2.33)$$

$$F_2 = \nu W_2 \quad (2.34)$$

and to use the dimensionless Bjorken variable

$$x = \frac{Q^2}{2p \cdot q}. \quad (2.35)$$

In the first measurements of deep inelastic electron scattering from protons scaling of the structure functions was observed. The structure functions $F_{1|2}$ showed no dependence on the momentum transfer squared Q^2 . Since finite objects are described by form factors, which show a Q^2 -dependence, scaling indicates the scattering from structureless objects. The scaling was already predicted by Bjorken [21] before it was observed in experiments [22, 23], but the simple physical explanation of structureless partons as constituents of the proton was given by Feynman [24].

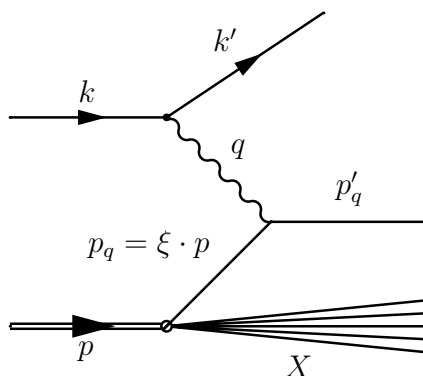


Figure 2.4: Schematic picture of deep inelastic scattering in the parton model. The electron scatters from one of the constituents of the nucleon, while the other constituents act as spectators.

The Parton Model

In the parton model the electron interacts with a single quasi-free quark inside the proton. This quark is supposed to carry a fraction ξ of the proton's momentum. Due to the large momentum transfer Q^2 in deep inelastic scattering, the struck quark receives a large transverse momentum and is finally observed as a hadronic jet with large p_\perp (see Fig.2.4). Furthermore, for large momentum transfers the interaction time is very short compared to the time-scale on which the partons, the quarks and gluons, interact among themselves. Thus, in the infinite momentum limit, the partons inside the proton can be regarded as free particles. In this limit, the cross section for electron scattering from a proton factorizes and can be written as a convolution of the cross section for electron scattering off a quark with momentum $\xi \cdot p$ and the probability density of quarks with this momentum in the proton:

$$\sigma(e(k) + N(p) \rightarrow e(k') + X) = \int_0^1 d\xi \sum_i f_i(\xi) \sigma(e(k) + q(\xi \cdot p) \rightarrow e(k') + q(p')), \quad (2.36)$$

where ξ turns out to be equal to the kinematic variable $\xi = x = \frac{Q^2}{2p \cdot q}$. This means the Bjorken variable x is just the fraction of proton momentum that a parton must have in order to absorb the virtual photon. The parton distribution function $f_i(x)dx$ gives the probability to find a parton

of flavor i with a momentum fraction between x and $x + dx$. Unlike the electron quark scattering cross section, the parton distribution functions (PDFs) f_i cannot be computed perturbatively, since they depend on soft processes. Therefore they have to be determined by experiment, see e.g. [25, 26]. The structure functions $F_{1|2}$ are given by

$$F_1 = \frac{1}{2} \sum_i e_i^2 f_i(x) \quad (2.37)$$

$$F_2 = x \sum_i e_i^2 f_i(x), \quad (2.38)$$

where e_i is the charge of parton i . The Callan-Gross relation $F_2(x) = 2xF_1(x)$ reflects the spin- $\frac{1}{2}$ nature of the quarks.

The QCD improved Parton Model

In more precise experiments Bjorken scaling turns out to be violated. This is due to the fact that the parton model as described here is only the lowest order of an expansion in the strong coupling constant α_s . For more precise calculations, the interactions of quarks and gluons among each other have to be considered, in particular at small momentum scales Q^2 . For example, radiative corrections have to be included. These corrections can be calculated perturbatively. This leads to a set of integro-differential equations for the PDFs, the DGLAP evolution equations, which determine the Q^2 -dependence of the PDFs. Once the PDFs are known at some scale Q_0 , they can be calculated at any other scale, where leading order perturbative QCD applies. The DGLAP evolution equations mathematically express the fact that a quark with momentum fraction x could have come from a quark with larger momentum fraction y , which lost momentum by radiating a gluon.

2.3 The Electromagnetic Structure of Nuclei

The scattering of electrons from nuclei can be described, in the same way as the scattering from nucleons, in terms of the hadron tensor $W_{\mu\nu}$ (see equation (2.30)). All information about the target and its response to the electromagnetic interaction is contained in the functions $W_{1|2}$. How the response functions are described depends on the momentum transfer squared Q^2 of the virtual photon.

For very low energies, when $1/Q$ is of the order of the size of the nucleus, the electrons scatter from the nucleus as a whole and the nucleus remains in its ground state. In principle, the response functions are the same as in elastic nucleon scattering (see equations 2.31 and 2.32)

$$W_1(\nu, Q^2) = \tau |G_M^A(Q^2)|^2 \delta\left(\nu - \frac{Q^2}{2M_A}\right) \quad (2.39)$$

$$W_2(\nu, Q^2) = \frac{|G_E^A(Q^2)|^2 + \tau |G_M^A(Q^2)|^2}{1 + \tau} \delta\left(\nu - \frac{Q^2}{2M_A}\right), \quad (2.40)$$

but the nucleon mass in τ is replaced by the mass of the nucleus. Therefore $\tau = \frac{Q^2}{4M_A^2}$ and $\nu_{el} = \frac{Q^2}{2M_A}$ can in general be set to zero for these small momentum transfers. This leads to

$$W_1(\nu, Q^2) = 0 \quad (2.41)$$

$$W_2(\nu, Q^2) = |G_E^A(Q^2)|^2 \delta(\nu), \quad (2.42)$$

where $G_E^A(Q^2)$ is normalized such that

$$|G_E^A(0)|^2 = Z^2. \quad (2.43)$$

For the Q^2 -dependence of G_E^A for nuclei, several parameterizations exist, including, e. g., Gaussian or dipole parameterizations [8, 27].

For slightly larger momentum transfers, the nucleus can be excited, for example to the Giant Dipole Resonance. The response functions in this case are described by the Goldhaber-Teller model, see [8, 28].

For $1/Q$ of the order of internucleon distances in the nucleus, quasi-elastic scattering gives the main contribution. In this case, the electron scatters from a nucleon in the nucleus, which is then knocked out. The response functions can be approximated in terms of the ones for nucleon scattering

$$W_i = C(t) [ZW_i^p + (A - Z)W_i^n], \quad (2.44)$$

where the factor $C(t)$ accounts for the Fermi motion of the nucleons.

Deep Inelastic Scattering from Nuclei

Finally, for momentum transfers squared of $Q^2 \gg 1\text{GeV}^2$, we enter the region of deep inelastic scattering and the virtual photon becomes sensitive to the quark structure of the nucleons inside the nucleus. In a naive picture, the nucleus is just a collection of noninteracting nucleons and its structure function is given by

$$F_2^A(x) = (A - Z) \cdot F_2^n(x) + Z \cdot F_2^p(x). \quad (2.45)$$

The response functions of the nucleus are

$$W_1 = \frac{F_2^A}{2M_A x_A} = \frac{F_2^A}{2Mx} \quad (2.46)$$

$$W_2 = \frac{F_2^A}{\nu} = \frac{2M_A x_A}{Q^2} F_2^A = \frac{2Mx}{Q^2} F_2^A. \quad (2.47)$$

For deep inelastic scattering from nuclei we have to distinguish between the momentum fraction of the nucleon x and of the nucleus $x_A = x \cdot x_{N|A}$ with $x_{N|A} = 1/A$ carried by the quark. The first measurements of the ratio

$$R = \frac{F_2^A/A}{F_2^D/2} \approx \frac{F_2^A/A}{F_2^p}, \quad (2.48)$$

however, revealed a significant deviation of the nuclear structure function per nucleon from that of free nucleons or of deuterium, which is, in principle, assumed to be a good approximation to free nucleons. Since these first measurements were carried out by the European Muon Collaboration (EMC), this effect became known as the 'EMC effect'.

There are two aspects which make the study of nuclear structure functions and nuclear parton distribution functions (nPDFs) interesting: First, knowing the behavior of the nuclear wave function at high energies provides useful information about the long-range QCD forces, which are responsible for binding the nucleons in the nucleus. Second, nuclear PDFs are an important ingredient for predicting and understanding particle production in the collisions of heavy nuclei [29].

Nuclear Modifications

Typically, two sorts of nuclear effects can occur:

- (i) the incoherent scattering from nucleons whose structure functions are modified in the presence of the nuclear medium

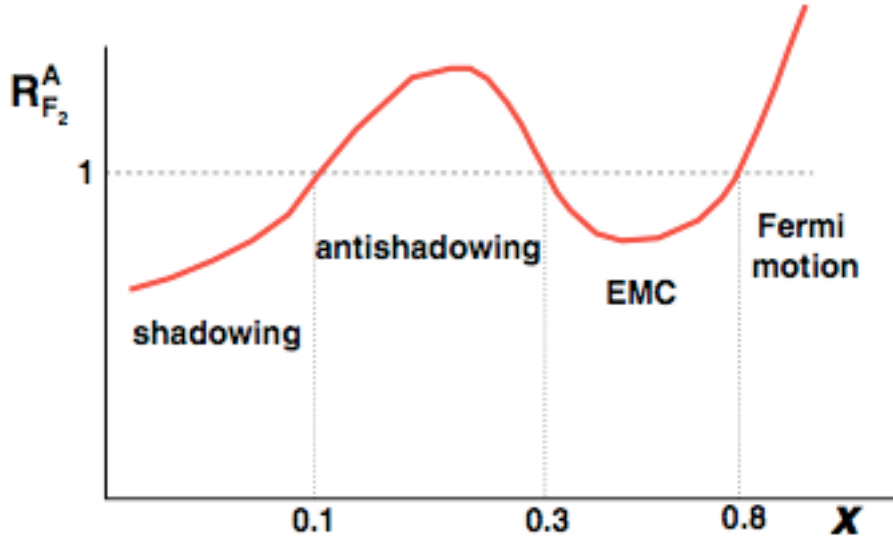


Figure 2.5: Schematic behavior of $R_{F_2}^A(x, Q^2)$ as function of x for given fixed Q^2 , taken from [30]

(ii) coherent scattering processes, where several nucleons are involved in the scattering process

Fig. (2.5) provides a schematic overview of the ratio R defined in equation (2.48) for Bjorken x between 0 and 1. As indicated in the figure, the effects in different regions of x are explained by different mechanisms:

- $x < 0.1$: nuclear shadowing regime
- $0.1 \leq x \leq 0.3$: anti-shadowing regime (small enhancement of R)
- $0.3 \leq x \lesssim 0.8$: traditional 'EMC effect' (depletion)
- $x > 0.8$: enhancement, mainly due to Fermi motion

Nuclear Shadowing and Anti-Shadowing

The nuclear shadowing in the region $x \leq 0.1$ is mainly due to strong coherence effects. Several nucleons participate in the scattering processes and interference between the scattering from different nucleons becomes important. This interference can be destructive (shadowing) or constructive (anti-shadowing). There are two approaches for obtaining nuclear PDFs in this region:

- (i) Strikman et al. [31, 32], for example, analyze the microscopic structure of nuclei and model the origin of nuclear shadowing. They relate nuclear shadowing to the diffraction cross section off a free nucleon and model multiple rescattering in terms of an attenuation factor.
- (ii) Eskola et al. [33, 34], for example, model the nuclear PDFs at some initial scale Q_0^2 , mainly by fitting the ratio R of equation (2.48) to existing data and subsequently study their Q^2 -evolution through the DGLAP equations. Since fixed target experiments measure the structure functions along a curve in the x - Q^2 -plane, the nPDFs at Q_0^2 have to be computed iteratively.

What is seen as multiple scattering in the rest frame of the nucleus corresponds to parton recombination in the infinite momentum frame [30]. In the infinite momentum frame, the wave

functions of partons from different nucleons can overlap. Thus, the interaction between partons belonging to different nucleons becomes possible. Two partons can, for example, fuse to produce a parton with higher momentum and larger x . This causes a decrease of the parton density in this region of x and at the same an enhancement at larger x ($x > 0.1$). This enhancement is known as anti-shadowing.

Traditional 'EMC effect'

The depletion known as the traditional 'EMC effect', in the region $0.3 \lesssim x \lesssim 0.8$, is mainly due to incoherent scattering, where the structure functions of the individual nucleons are modified. The deep inelastic scattering off nuclear targets is a two-step process. The virtual photon scatters off quarks, which are distributed within nucleons, which are in turn distributed within the nucleus. This can be described in a convolution model [35].

$$f_{q|A}(x_A, Q^2) = \sum_T \int_{x_A}^1 dy_A f_{q|T} \left(\frac{x_A}{y_A} \right) f_{T|A}(y_A), \quad (2.49)$$

where y_A is the fraction of the nucleus' momentum carried by the nucleon and x_A the fraction of the nucleus' momentum carried by the struck parton.

There are two possible explanations for the change in the structure functions. First, in a conventional nuclear physics model, not only the nucleons contribute to the structure function of the nucleus, but also the pions, which are responsible for binding the nucleons. They give a contribution

$$\delta^\pi F_2^N(x_A) = \int_{x_A}^1 dy_A f_{\pi|A}(y_A) F_2^\pi \left(\frac{x_A}{y_A} \right). \quad (2.50)$$

to the nuclear structure function. The main difficulty with this model is that the pions in the nucleus are off-shell and therefore the pion structure function F_2^π depends on the pion momentum squared.

Alternatively, the modification can be in the short-range physics, which is described by the parton density in the nucleon $f_{q|N}$. The intrinsic properties of nucleons in an nuclear environment are changed. This results in a modification of the parton distribution of nucleons in a nucleus. For example, a change in scale in the structure functions is observed

$$\frac{F_2^A}{A}(x, Q^2) = F_2^N(x, \xi_A \cdot Q^2). \quad (2.51)$$

The suggested explanation for this is a modification of the effective confinement scale for the quarks in the nucleus as compared to quarks in free nucleons. This change in the confinement scale cannot be explained merely by the increased radius of the nucleon in the nuclear medium, but is mainly due to the overlap of the nucleons in heavy nuclei. With this change in confinement scale the depletion in the region $0.3 \lesssim x \lesssim 0.8$ can be described.

$x \sim 1$ - region

In the region $x > 0.8$, the presentation of nuclear effects in terms of the ratio $\frac{F_2^A/A}{F_2^p}$ is misleading, since F_2^p is very small in this region and strictly vanishes for $x \geq 1$, whereas the Bjorken variable x in nuclei may take values even larger than one. In this region nuclear effects therefore appear artificially enhanced.

2.4 The Weak Structure of Nucleons

In the same way as the electromagnetic structure is probed by electron scattering from nucleons, the weak structure can, among others, be probed by the scattering of neutrinos from nucleons (see Fig. 2.6). Due to the weakness of the electroweak coupling, these reactions are much rarer and therefore difficult to measure precisely. The charged current matrix element that connects

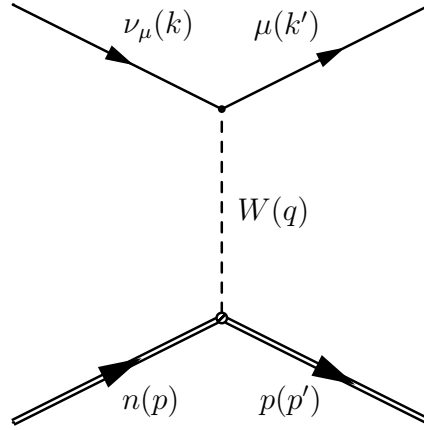


Figure 2.6: Neutrino scattering off neutrons probes the weak structure of nucleons.

the neutron and the proton can be investigated in quasielastic neutrino scattering

$$\nu_\mu + n \rightarrow \mu^- + p. \quad (2.52)$$

As in electron-nucleon scattering the matrix element for this reaction can be split into a hadronic weak current

$$\langle p(p') | J_\lambda | n(p) \rangle \propto \bar{u}_p(p') \Gamma_\lambda u_n(p), \quad (2.53)$$

a leptonic weak current

$$\langle \mu(k') | j_{\lambda'} | \nu_\mu(k) \rangle \propto \bar{u}_\mu(k') \gamma_{\lambda'} (1 - \gamma_5) u_\nu(k), \quad (2.54)$$

and a massive gauge boson propagator

$$\frac{-g^{\lambda\lambda'} + \frac{q^\lambda q^{\lambda'}}{M_W^2}}{q^2 - M_W^2}. \quad (2.55)$$

The momentum transfer in neutrino scattering is in general small compared to the mass of the W boson M_W and the W-propagator can thus be approximated by

$$\frac{g^{\lambda\lambda'}}{M_W^2}. \quad (2.56)$$

This leads to the following matrix element for neutrino scattering from a proton:

$$\mathcal{M} \propto \bar{u}_p(p') \Gamma_\lambda u_n(p) \bar{u}_\mu(k') \gamma^\lambda (1 - \gamma_5) u_\nu(k) \quad (2.57)$$

with Γ_λ being the charge current weak interaction vertex connecting the neutron and the proton. In its most general form Γ_λ can be parameterized in terms of six weak form factors

$$\Gamma_\lambda \propto [F_V(q^2)\gamma_\lambda + iF_M(q^2)\sigma_{\lambda\nu}q^\nu + F_S(q^2)q_\lambda + F_A(q^2)\gamma_\lambda\gamma_5 + iF_T(q^2)\sigma_{\lambda\nu}q^\nu\gamma_5 + F_P(q^2)q_\lambda\gamma_5]. \quad (2.58)$$

Some standard assumptions, which can be found in [20, 36] simplify the vertex:

- (i) Because of time reversal invariance, the form factors have to be real.
- (ii) The term proportional to the induced tensor form factor F_T shows opposite behavior under charge symmetry and would define a second class current. Since there are no observations of second class currents, we drop the F_T -term in our calculations. The same assumption holds for the induced scalar form factor F_S and therefore we set $F_S = 0$ as well.
- (iii) The conserved vector current hypothesis (CVC) relates F_V and F_M to the electromagnetic form factors introduced in section 2.2:

$$F_V(q^2) = F_1^p(q^2) - F_1^n(q^2) \quad (2.59)$$

$$F_M(q^2) = \frac{1}{2M}(\kappa_p F_2^p(q^2) - \kappa_n F_2^n(q^2)). \quad (2.60)$$

- (iv) The partially conserved axial current hypothesis (PCAC) relates the induced pseudoscalar form factor F_P to the axial vector form factor F_A . As a result the term proportional to F_P is negligible compared to the F_A -term when taken between nucleon states.
- (v) By analogy with the vector form factors, a dipole form is commonly assumed for the axial vector form factor F_A

$$F_A(q^2) = \frac{F_A(0)}{\left(1 + \frac{q^2}{m_A^2}\right)^2}, \quad (2.61)$$

where $F_A(0) = -1.26$ is determined from the beta decay of neutrons.

Consequently, the weak nucleon-nucleon vertex reduces to

$$\Gamma_\lambda \propto [F_V(q^2)\gamma_\lambda + iF_M(q^2)\sigma_{\lambda\nu}q^\nu + F_A(q^2)\gamma_\lambda\gamma_5]. \quad (2.62)$$

Thus, the main purpose of quasielastic neutrino scattering experiments on nucleons is to measure the weak axial vector form factor $F_A(q^2)$ and in particular the parameter m_A of the dipole fit. Mann et al. [37] obtain a value of $m_A = (0.95 \pm 0.12)\text{GeV}$, while Miller et al. [38] find $m_A = (1.00 \pm 0.05)\text{GeV}$, and Baker et al. [36] find $m_A = (1.07 \pm 0.06)\text{GeV}$. All three values are obtained with m_V fixed at $m_V = 0.84\text{GeV}$ and agree with the value $m_A = (1.15 \pm 0.27)\text{GeV}$ determined from pion electroproduction, see e.g. [39]. Both Miller et al. and Baker et al. furthermore provide a test of the validity of the CVC hypothesis by simultaneously fitting m_A and m_V to their experimental data:

$$\begin{aligned} \text{Miller et al.: } & m_V = (0.96 \pm 0.04)\text{GeV} & m_A = (0.80 \pm 0.10)\text{GeV} \\ \text{Baker et al.: } & m_V = (0.86 \pm 0.04)\text{GeV} & m_A = (1.04 \pm 0.14)\text{GeV} \end{aligned}$$

m_V can then be compared to the value $m_V = 0.84\text{ GeV}$ determined from elastic lepton scattering.

Equivalent Particle Approximations

3.1 Introduction

The parton model introduced in section 2.2 is a very useful tool for studying high energy processes. In the same way as quarks and gluons form the nucleons, photons can be regarded as the constituents of fast moving charged particles and cross sections can be approximated by the convolution of the (equivalent) photon distribution function $f_\gamma(z)$ with the cross section of the real photon subprocess

$$\sigma = \int f_\gamma(z) \sigma_\gamma dz. \quad (3.1)$$

Here z is the momentum fraction of the incident particle's energy that is carried away by the photon. The probability that the incident particle radiates a photon with a momentum fraction between z and $z + dz$ is given by $f_\gamma(z)dz$. In the equivalent photon approximation e.g. electron induced processes can be related to photon induced processes, which greatly simplifies the calculation.

3.2 Electron and Photon Splitting Functions

Historically, Fermi [40] was the first to point out that the field of a fast moving charged particle is similar to electromagnetic radiation and may therefore be interpreted as a flux of photons distributed with some density $n(\omega)$ on a frequency spectrum. Williams [41] and Weizsäcker [42] further developed Fermi's semiclassical treatment and extended it to high energy electrodynamics. Hence the equivalent photon approximation is also often referred to as Weizsäcker-Williams approximation.

The equivalent photon approximation is not only valid in the semiclassical approach used by Fermi, Williams, and Weizsäcker, but can also be derived using the methods of Quantum Electrodynamics (QED). The dependence of the equivalent photon spectrum of electrons on the photon

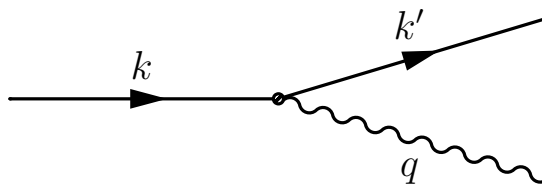


Figure 3.1: virtual photon emission vertex

frequency ω and its virtuality q^2 is unambiguously defined by the form of the electron-photon vertex $e \rightarrow e'\gamma^*$, see Fig. 3.1. Since this is a pure QED process, where perturbation theory can safely be applied, the photon PDFs can even be calculated (see e. g. [43]), as opposed to the quark and gluon PDFs introduced in section 2.2, which have to be determined by experiment. The matrix element for the splitting of an electron with energy ϵ into an electron of energy $(1-z) \cdot \epsilon$ and a photon of energy $z \cdot \epsilon$ is derived in the textbook of Peskin and Schroeder [44]. In their derivation they treat the photon pole by assuming collinear emission of a photon and an electron. This means both particles are emitted with very small transverse momentum. In their calculation, Peskin and Schroeder replace the numerator of the photon propagator by a sum over the physical polarization vectors. They decouple the photon emission vertex (Fig. 3.1) from the rest of the diagram and evaluate it explicitly between physical polarization states of massless particles. Their result for the electron splitting function,

$$\frac{1}{2} \sum_{\text{polarizations}} |\mathcal{M}(e \rightarrow e'\gamma^*)|^2 = \frac{2e^2 p_{\perp}^2}{z(1-z)} \left[\frac{1+(1-z)^2}{z} \right], \quad (3.2)$$

can be integrated over p_{\perp}^2 from the electron mass squared m_e^2 to an energy squared s , which is characteristic for the real photon subprocess. This results in

$$f_{\gamma}(z) = \frac{\alpha}{2\pi} \log \frac{s}{m_e^2} \left[\frac{1+(1-z)^2}{z} \right] \quad (3.3)$$

for the photon distribution function. Calculations of Baier et al. [45] and Chen et al. [46] yield similar results. When calculating cross sections in the equivalent photon approximation the following assumptions are made:

- (i) the virtual photon is on its mass shell $q^2 \approx 0$ and
- (ii) the virtual photon is only transversely polarized.

For most processes a dynamical cutoff Λ_{γ} exists such that for $|q^2| < \Lambda_{\gamma}^2$ the cross section of the photon induced subprocess differs only slightly from the real photon cross section and decreases quickly for $|q^2| > \Lambda_{\gamma}^2$, which permits the use of the equivalent photon approximation for $|q^2| < \Lambda_{\gamma}^2$. A similar calculation can be made for the splitting of a photon into a pair of light fermions, e.g. an electron-positron pair or a muon-antimuon pair. The corresponding photon splitting function is given in [44] by

$$f_{l|\gamma}(z) = \frac{\alpha}{2\pi} \log \frac{s}{m_l^2} [z^2 + (1-z)^2]. \quad (3.4)$$

Here z is the energy fraction of the incident photon's energy carried by the lepton. This approximation can be combined with the equivalent photon approximation for ions, for example, which we will introduce later in this chapter. In this way, ions in heavy ion collisions can be treated as equivalent lepton beams to study, for example, deep inelastic lepton scattering from heavy nuclei (see chapter 4 for details).

3.3 Equivalent Photon Approximation for Extended Objects

In the treatment of nucleons and nuclei equation (3.1) still holds, but a special situation occurs in the calculation of the corresponding photon distribution function $f_{\gamma}(z)$ of these particles. The compositeness of nucleons and nuclei gives rise to two modifications in the theoretical treatment:

- (i) Since nucleons and nuclei are not point-like particles, they have an extended charge distribution, as well as an excitation spectrum. They might even break up under the emission of the equivalent photon. These effects can be taken into account by using the appropriate form factors and thereby distinguishing between elastic and inelastic photon spectra.

- (ii) Nucleons and nuclei consist of and are themselves strongly interacting particles. The cross sections of processes due to the strong interaction are overwhelmingly large. Still, clean electromagnetic processes can be studied in ultra-peripheral collisions, where the impact parameter is large enough that the colliding particles do not overlap and therefore cannot interact via the short-range strong interaction. In the framework of the equivalent photon approximation, the region where the particles interact strongly, can be excluded in a semi-classical approach, using impact parameter dependent equivalent photon spectra. This approach works reasonably well for heavy ions.

Budnev et al. derive in their paper [47] a general equation for the equivalent photon spectrum based on a plane wave approximation

$$\frac{dn}{d\omega} = \frac{\alpha}{\pi} \frac{d(-q^2)}{|q^2|} \left[\left| \frac{q_{\perp}^2}{p^2} \right| D + \frac{\omega^2}{2E^2} C \right]. \quad (3.5)$$

$n(\omega)$ denotes the equivalent photon number, which is related to the photon distribution function used here in the following way

$$\frac{n(\omega)}{\omega} d\omega = f_{\gamma}(z) dz \quad (3.6)$$

and the photon energy ω is given in units of the incident particle's energy E :

$$\omega = z \cdot E. \quad (3.7)$$

Photon spectra for different kinds of particles can be derived from equation (3.5) by inserting different functions C and D , which are related to the form factors of the incident particles. Budnev et al. give a list of particles for which equation (3.5) is applicable together with the corresponding functions C and D . In the region of small photon energies $\omega \ll E$ (which is the dominant region here), the term proportional to C in equation (3.5) can, in general, be neglected.

3.3.1 Elastic Equivalent Photon Spectrum of Nuclei

The typical form factor behavior for elastic photon emission by nuclei is

$$F_{el}(q^2) \approx \begin{cases} Z & \text{for } |q^2| < \frac{1}{R^2} \\ 0 & \text{for } |q^2| \gg \frac{1}{R^2} \end{cases} \quad (3.8)$$

as was already pointed out in section 2.3. The form factor limits the momentum transfer squared q^2 to small values with a maximum q^2 determined by the size of the nucleus. This guarantees the applicability of the equivalent photon approximation.

As already mentioned above, for heavy ions it is important to exclude the region where they interact strongly. This can be done in a semi-classical approach using impact parameter dependent photon spectra. A quite complete description of the method in the semi-classical approach and the derivation of the photon spectrum can be found in the textbook of Jackson [48] and we will briefly outline the procedure here. The flux of equivalent photons from a projectile with charge Ze moving on a straight line with velocity β and an impact parameter b is determined from the Fourier transform of the accompanying electromagnetic field

$$N(\omega, b) = \frac{Z^2 \alpha}{\pi^2} \left(\frac{\omega}{\gamma \beta} \right)^2 \left[K_1^2(x) + \frac{1}{\gamma^2} K_0^2(x) \right], \quad (3.9)$$

where $\gamma = 1/\sqrt{1-v^2}$ is the Lorentz-factor of the projectile, $K_n(x)$ are the modified Bessel functions of n th order, and $x = \frac{\omega b}{\gamma \beta}$. The term proportional to $K_1^2(x)$ gives the flux of transversely

polarized photons. The second term, proportional to $K_0(x)^2$ gives the flux of longitudinally polarized photons and is suppressed in ultraperipheral collisions by the factor $1/\gamma^2$. Equation (3.9) provides the equivalent photon spectrum of a fast moving point charge, but it can be applied to nuclei as well assuming a spherically symmetric charge distribution and impact parameters, which are larger than the radial extension R of the nucleus. This is due to the fact that the electric field outside a spherically symmetric charge distribution depends only on the total charge inside it. The equivalent photon spectrum is obtained by an integration over the impact parameter

$$n(\omega) = \int d^2b N(\omega, b). \quad (3.10)$$

This integration is carried out from a minimum impact parameter, given by the size of the nucleus, to infinity yielding

$$\begin{aligned} n(\omega) &= \int_R^\infty 2\pi b N(\omega, b) db \\ &= \frac{2Z^2\alpha}{\pi} \left[\xi K_0(\xi) K_1(\xi) - \frac{\xi^2}{2} (K_1^2(\xi) - K_0^2(\xi)) \right] \end{aligned} \quad (3.11)$$

with $\xi = \omega R/\gamma\beta$. Equation (3.11) can be approximated, see e.g. [8], for small ξ by

$$n(\omega) \approx \frac{2Z^2\alpha}{\pi} \log\left(\frac{\gamma\beta}{\omega R}\right). \quad (3.12)$$

This approximation is quite reasonable for quick estimates and will be enough for our purposes. Vidović et al. derive the impact parameter dependent equivalent photon spectrum directly from QED [49]

3.3.2 Elastic Equivalent Photon Spectrum of Protons

The elastic photon spectrum of a proton may be described in terms of the elastic form factors of the proton, see section 2.2. Kniehl derives in his paper [50] a modified Weizsäcker-Williams approximation for the scattering of electrons off protons, where he replaces the proton by the equivalent photon distribution

$$f_{\gamma|p}(z) = -\frac{\alpha}{2\pi} z \int_{t_1}^{t_2} \frac{dt}{t} \left\{ 2 \left[\frac{1}{z} \left(\frac{1}{z} - 1 \right) + \frac{M^2}{t} \right] H_1(t) + H_2(t) \right\}. \quad (3.13)$$

Here $t = q^2$ is the momentum transfer squared of the photon and the functions H_i are related to the elastic form factors of the proton as follows

$$H_1(t) = F_1^2(t) + \tau F_2^2(t) = \frac{G_E^2(t) + \tau G_M^2(t)}{1 + \tau} \quad (3.14)$$

$$H_2(t) = (F_1(t) + F_2(t))^2 = G_M^2(t). \quad (3.15)$$

Performing the integration over t the approximate spectrum reads

$$\begin{aligned} f_{\gamma|p}^{el}(z) &= \frac{\alpha}{2\pi} z \left[c_1 u \log\left(1 + \frac{c_2}{v}\right) - (u + c_3) \log\left(1 - \frac{1}{v}\right) + \frac{c_4}{v-1} \right. \\ &\quad \left. + \frac{c_5 u + c_6}{v} + \frac{c_7 u + c_8}{v^2} + \frac{c_9 u + c_{10}}{v^3} \right] \end{aligned} \quad (3.16)$$

with

$$u = \frac{1}{2} - \frac{2}{z} + \frac{2}{z^2} \quad (3.17)$$

and

$$v = 1 + \frac{M^2}{0.71 \text{ GeV}^2} \frac{z^2}{1-z}. \quad (3.18)$$

The constants c_i are given in terms of $a = 4M^2/0.71\text{GeV}^2$ and $b = 2.78$ in [50] and their approximate values are

$$\begin{aligned} c_1 &\approx -2.76 \cdot 10^{-2} & c_6 &\approx -11.3 \\ c_2 &\approx 3.96 & c_7 &\approx -0.716 \\ c_3 &\approx 13.8 & c_8 &\approx -4.43 \\ c_4 &\approx -2.48 & c_9 &\approx 0.238 \\ c_5 &\approx -0.89 & c_{10} &\approx -2.12. \end{aligned}$$

Kniehl tests his approximation in the case of the process $e + p \rightarrow \nu + W + p$ and finds that it reproduces the exact result within better than one percent accuracy.

Another possibility is to use the proton analogue to equation (3.12) using the proton charge radius for R

$$f_{\gamma|p}^{el}(z) = \frac{\alpha}{\pi} \frac{1}{z} \log\left(\frac{0.71 \text{ GeV}^2}{z^2 M^2}\right). \quad (3.19)$$

Fig. 3.2 shows a comparison between the two elastic photon spectra for protons from equations (3.16) and (3.19) and for ions from equation (3.12) scaled with $1/Z^2$ to be comparable to the proton spectra.

3.4 Two-Step Approximations

3.4.1 Deep Inelastic Equivalent Photon Spectrum of Protons

As already mentioned above, due to the composite nature of protons, there are two contributions to the equivalent photon spectrum: the elastic contribution, discussed above ($p \rightarrow \gamma + p$) and an inelastic contribution ($p \rightarrow \gamma + X$). The contribution of deep inelastic photon emission to the equivalent photon spectrum should become relevant at high energies due to the logarithmic enhancement factor $\log\left(\frac{s}{m_q^2}\right)$, where m_q is the quark mass. In the deep inelastic equivalent photon approximation, a two-stage parton picture applies: The photon is seen as a constituent of the quark inside the proton. Accordingly, the distribution of deeply inelastic photons in the proton is obtained from the convolution of the photon distribution function of point-like particles (the quarks) with the quark PDFs of the proton

$$f_{\gamma|p}^{inel}(z) = \int dx \sum_q e_q^2 f_{q|p}(x, \langle Q^2 \rangle) f_{\gamma|q}\left(u = \frac{z}{x}\right). \quad (3.20)$$

Here z is the energy fraction of the proton carried by the photon, x denotes the quark's energy fraction and u the energy of the photon in units of the quark's energy. The quark radiates as a point-like particle. Thus, its spectrum is given by

$$f_{\gamma|q}(u) = \frac{\alpha}{2\pi} \frac{1 + (1-u)^2}{u} \log\left(\frac{Q_{max}^2}{Q_{min}^2}\right). \quad (3.21)$$

In order to simplify the equations we have already carried out the integration over q^2 and thereby neglected the dependence of the PDFs on the momentum transfer squared Q^2 . Instead we insert an average value, chosen according to Pisano in [51]

$$\langle Q^2 \rangle = \frac{Q_{max}^2 - Q_{min}^2}{\log Q_{max}^2 - \log Q_{min}^2}. \quad (3.22)$$

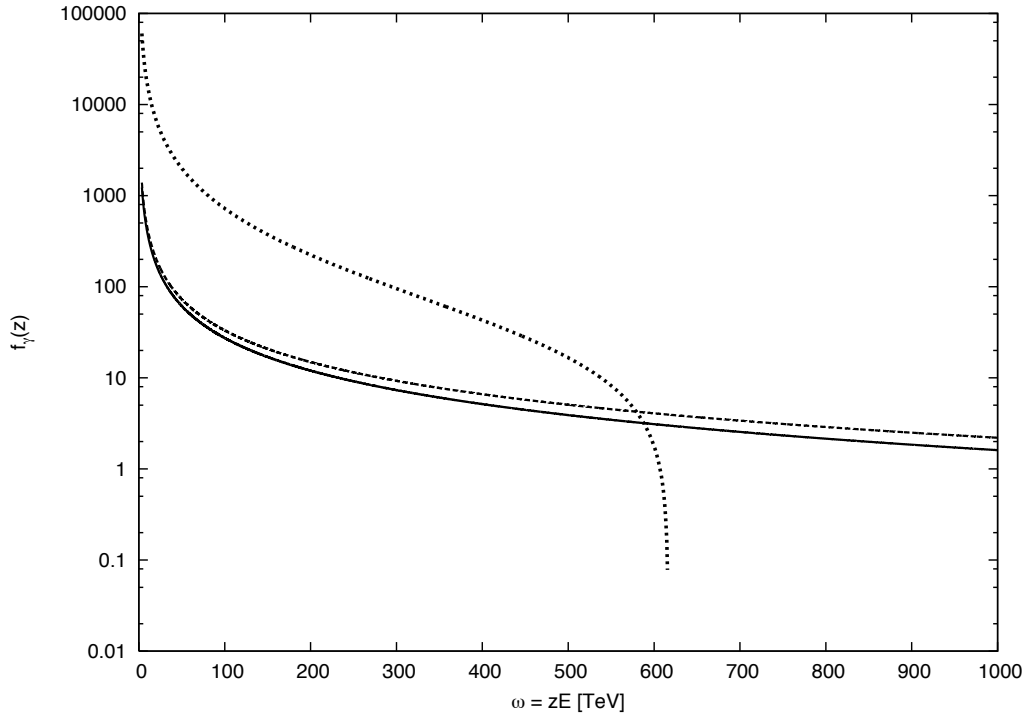


Figure 3.2: Elastic equivalent photon spectra for protons according to equation (3.16) (solid line) and equation (3.19) (dashed line), and for ions according to equation (3.12) scaled with a factor $1/Z^2$ (dotted line).

Q_{min} can, in principle, be chosen of the order of magnitude of the light quark masses. We choose a value $Q_{min} = 1$ GeV, which guarantees the applicability of the quark parton model. The choice of the value Q_{max} depends on the actual process, which is studied.

For heavy ions the contribution of deep inelastic photons is negligible as compared to the elastic contribution, since the factor Z^2 , coming from the coherent action of all protons in the nucleus, is replaced by a sum over all nucleons, which contributes only a factor $\sim A$.

3.4.2 Equivalent Leptons in Nuclei

Another two-step application of the equivalent particle approximations is the description of heavy ions in terms of equivalent leptons, which we will call the equivalent lepton approximation (ELA) henceforth. In this approximation, the ion is replaced by a spectrum of equivalent photons according to equation (3.12). These (equivalent) photons themselves may split into a pair of (equivalent) leptons, whose distribution function is the photon splitting function (3.4) introduced in section 3.2. The constituents of the daughter pair subsequently react as equivalent beams with the target system. This provides a way to study the parton structure of nuclei via deep inelastic lepton scattering in the collision of heavy nuclei. The distribution of equivalent leptons in a nucleus is given by the convolution of the two spectra

$$f_{\gamma|A}(u) = \frac{2\alpha Z^2}{\pi u} \log\left(\frac{1}{uM_K R}\right) \quad (3.23)$$

and

$$f_{l|\gamma}(\omega, z) = \frac{\alpha}{\pi} \log\left(\frac{\omega}{m}\right) [z^2 + (1-z)^2] \quad (3.24)$$

$$f_{l|A}(y) = \int \frac{du}{u} f_{\gamma|A}(u) f_{l|\gamma}(\omega = u \cdot E_A, z = \frac{y}{u}), \quad (3.25)$$

where the lepton's energy is $E_l = z \cdot \omega = z \cdot u \cdot E_A = y \cdot E_A$. The total cross section in this case is given by the convolution of the spectrum (3.25) with the lepton induced cross section σ_l

$$\sigma = \int dy f_{l|A}(y) \sigma_l. \quad (3.26)$$

Lepton Pair Production from Deep Inelastic Scattering

4.1 Introduction

Ultra-peripheral heavy ion collisions enable the study of electromagnetic processes at energies, which are neither attainable in conventional fixed target experiments nor at electron-proton colliders. Since in UPCs the ions do not meet and therefore do not interact hadronically, the cross sections of such processes are not overwhelmed by the strong interaction. The long-range electromagnetic interaction, which can be treated perturbatively in the framework of quantum electrodynamics (QED), gives the main contribution in such UPCs. The electromagnetic production of lepton pairs, which are mainly produced via the two-photon process, has a large cross section in heavy ion collisions. Up to now, consideration has focused predominantly on those processes with two coherent interactions at the nuclei, characterized by momentum transfers $Q^2 \leq \frac{1}{R^2}$ with R being the size of the nucleus [5, 6, 7, 8]. There is, however, another class of processes, which are much rarer. In these processes one of the interactions is coherent and the other involves a deep inelastic scattering with $Q^2 \gg \frac{1}{R^2}$, see Fig. 4.1. Such processes offer the possibility to study nuclear structure.

The Feynman diagrams of this process have three intermediate particles: two photons (see Fig. 4.1) and one lepton (see Fig. 4.2). Small denominators of the corresponding propagators, implying almost on-shell intermediate particles, cause large contributions to the matrix element and therefore to the cross section. To the two-photon pair production cross section two kinematic regions contribute: the double-photon pole region, where both photons are quasi-real, and the photon-lepton-pole region, where only one of the photons and the intermediate lepton are quasi-real [46]. For small transverse momenta of the leptons, the double-photon pole contribution dominates. However, if events with at least one lepton with large transverse momentum are selected, the two contributions become comparable in size. Yet they do show different event characteristics. In the double-photon pole contribution the two leptons are produced back to back in the transverse plane, that is with equal transverse momenta. In contrast, in the photon-lepton pole contribution only one of the leptons obtains a large transverse momentum from the highly off-shell photon. In [52] this is discussed in detail for a real photon, which produces a lepton pair by inelastic scattering and approximate numerical results are provided.

The asymmetry in the angular distribution of the leptons, together with the break-up of only one of the nuclei and the potential observation of the corresponding parton jet, is characteristic for deep inelastic pair production. Hence this unique event characteristic offers the possibility to differentiate between deep inelastic scattering and potential background, such as the doubly coherent process. The latter yields a more symmetric distribution of the produced leptons.

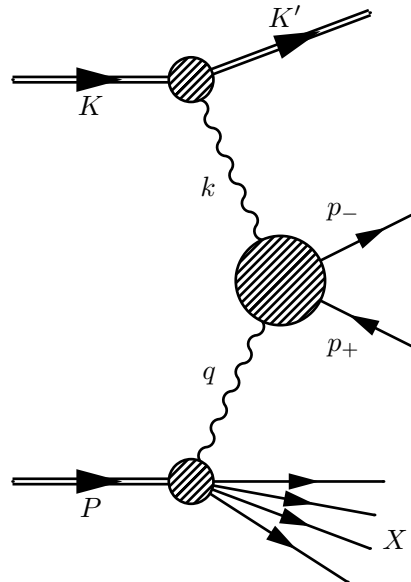


Figure 4.1: Schematic diagram for inelastic pair production in heavy ion collisions to lowest order. The shaded circle in the middle stands for the two lowest order Feynman diagrams for two-photon pair production (see Fig. 4.2).

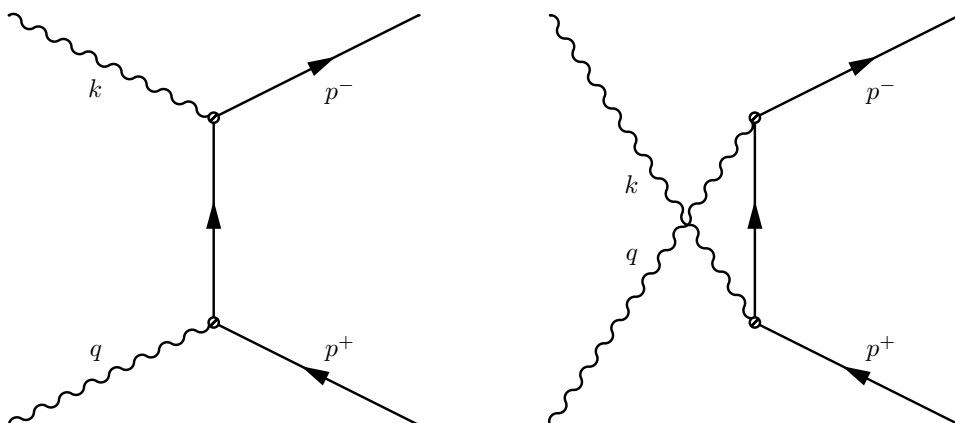


Figure 4.2: Lowest order Feynman diagrams for two-photon pair production.

As already discussed in section 2.3 of this work, the PDFs of quarks inside nucleons which are bound in a nucleus can differ considerably from those in free nucleons. The nuclear effects causing these deviations are commonly studied in fixed target deep inelastic lepton scattering experiments. The kinematic region which can be reached in fixed target experiments is, however, limited. Our study aims to examine, first, in which kinematic regions, one could expect a viable amount of events fitting the described characteristics in collider experiments such as the LHC at CERN, and second, the feasibility of studying the structure of nuclei from this process.

As already mentioned above, large contributions to the cross section come from the region, where the photon, which is emitted coherently, is almost real. This is due to the $\frac{1}{k^2}$ -dependence of the photon propagator. It was shown e. g. in [53, 47] that in such situations the equivalent photon approximation is applicable. The process then reduces to the one studied in [54] convolved with the equivalent photon spectrum of the ion (see chapter 3).

A second propagator whose denominator might become small, is the intermediate lepton propagator. Therefore we expect large contributions from the region where the intermediate lepton is close to its mass-shell. In such a situation, the photon lepton vertex can be treated as photon splitting into a lepton pair as described in [44, 45, 46]. A combination of the equivalent photon approximation and photon splitting, the equivalent lepton approximation (ELA), can be applied in this case. This simplifies the calculation considerably. Consequently, this approximation would be very useful for the calculation of processes which are similar to the one studied here. Moreover, it has already been used before [52]. Thus it is of interest to test the validity of these approximations.

In addition, the ELA provides a simple interpretation of the process studied here in terms of the parton picture: it relates electron (muon) pair production to deep inelastic electron (muon) scattering. One of the leptons, the one with larger transverse momentum, is thus directly related to the deep inelastic scattering, whereas the other acts as a spectator to this process. In principle, this means that the interference term between the two Feynman diagrams which contribute to lowest order is negligible.

Apart from the simplifications and the intuitive picture, a further advantage of the equivalent particle approach is, that impact parameter b smaller than $R_1 + R_2$, i. e. the region where the nuclei interact hadronically, can be excluded explicitly. This is not done in the plane wave approach used for the full calculation. In this respect, the cross sections calculated in the full calculation are an upper limit to the real ones. However, we do not expect the deviation to be large, since for small k^2 of the other photon the impact parameter is most likely large.

This chapter is organized in the following way. First, we calculate the matrix element for two-photon pair production up to lowest order. Integrating the squared matrix element over the appropriate phase space then yields the total cross section of pair production in the collision of two heavy ions. Depending on the choice of the form factors for the ions, we can calculate both the doubly coherent cross section as well as the one involving deep inelastic scattering at one of the ions. Thus, we can compare the event characteristics for both contributions and verify the division into two kinematic regions with distinct signatures described above. Furthermore, we include the two parameterizations of Frankfurt et al. [31, 32] and Eskola et al. [33, 34] which account for nuclear modifications on the PDFs in our calculations and compare them to the results obtained when using free PDFs. Next, we apply the EPA and the ELA to the process under consideration and compare the results, differential cross sections in particular, with those obtained in the full calculation in order to test the approximations quantitatively.

4.2 Full Calculation of Lepton Pair Production from Deep Inelastic Scattering

The total cross section for two-photon lepton pair production in heavy ion collisions is given by

$$\sigma = \frac{1}{F} \int (2\pi)^4 \delta^4(P + K - P' - K' - p_+ - p_-) |\mathcal{M}|^2 dPS. \quad (4.1)$$

F is the flux of the incoming particles with momenta P and K . P' , K' , p_+ , and p_- are the momenta of the final state particles, see Fig. 4.1. In the most general case, where both nuclei break up into a multi-particle final state denoted by X_P and X_K , respectively, the phase space is given by

$$\begin{aligned} dPS &= \frac{d^3p_+}{(2\pi)^3 2\epsilon_+} \frac{d^3p_-}{(2\pi)^3 2\epsilon_-} \prod_{n_1=1}^{N_1} \frac{d^4P_{n_1}}{(2\pi)^4} (2\pi) \delta(P_{n_1}^2 - M_{n_1}^2) \delta^4\left(P' - \sum_{n_1} P_{n_1}\right) \\ &\times \prod_{n_2=1}^{N_2} \frac{d^4K_{n_2}}{(2\pi)^4} (2\pi) \delta(K_{n_2}^2 - M_{n_2}^2) \delta^4\left(K' - \sum_{n_2} K_{n_2}\right). \end{aligned} \quad (4.2)$$

4.2.1 The Matrix Element of Two-Photon Pair Production in Heavy Ion Collisions

To compute the matrix element for this process, we split the diagram of Fig. 4.1 into three parts: one leptonic and two hadronic parts as depicted in Fig. 4.3. The squares of the amplitudes of these parts are represented by tensors. By contracting these tensors we obtain the squared matrix element $|\mathcal{M}|^2$ of equation (4.1) as function of scalar products of the momenta of the particles participating in the scattering.

The leptonic part of the matrix element is calculated from the two lowest order Feynman diagrams depicted in Fig 4.2. From these diagrams we obtain the following amplitudes

$$\mathcal{M}_1^{\mu\nu} = e^2 \frac{1}{k^2} \frac{1}{q^2} \left[\bar{u}(p_-) \gamma_\mu \frac{\not{k} - \not{p}_+ + m}{(k - p_+)^2 - m^2} \gamma_\nu v(p_+) \right] \quad (4.3)$$

$$\mathcal{M}_2^{\mu\nu} = e^2 \frac{1}{k^2} \frac{1}{q^2} \left[\bar{u}(p_-) \gamma_\nu \frac{\not{p}_- - \not{k} + m}{(p_- - k)^2 - m^2} \gamma_\mu v(p_+) \right], \quad (4.4)$$

where k and q are the momenta of the exchanged photons and m denotes the lepton mass. The tensor representing the matrix element for pair production from two virtual photons is given by the coherent sum of these amplitudes

$$M^{\mu\mu'\nu\nu'} = \sum_{s_+, s_-} \left(\bar{\mathcal{M}}_1^{\mu'\nu'} + \bar{\mathcal{M}}_2^{\mu'\nu'} \right) (\mathcal{M}_1^{\mu\nu} + \mathcal{M}_2^{\mu\nu}), \quad (4.5)$$

which, after the summation over the spins of the lepton (s_-) and anti-lepton (s_+), leads to

$$\begin{aligned} M^{\mu\mu'\nu\nu'} &= \frac{e^4}{q^4 k^4} \left\{ \frac{1}{x_2^2} \text{Tr} \left(\gamma_{\nu'} (\not{k} - \not{p}_+ + m) \gamma_{\mu'} (\not{p}_- + m) \gamma_\mu (\not{k} - \not{p}_+ + m) \gamma_\nu (\not{p}_+ - m) \right) \right. \\ &+ \frac{1}{x_1 x_2} \text{Tr} \left(\gamma_{\nu'} (\not{k} - \not{p}_+ + m) \gamma_{\mu'} (\not{p}_- + m) \gamma_\nu (\not{p}_- - \not{k} + m) \gamma_\mu (\not{p}_+ - m) \right) \\ &+ \frac{1}{x_1 x_2} \text{Tr} \left(\gamma_{\mu'} (\not{p}_- - \not{k} + m) \gamma_{\nu'} (\not{p}_- + m) \gamma_\mu (\not{k} - \not{p}_+ + m) \gamma_\nu (\not{p}_+ - m) \right) \\ &\left. + \frac{1}{x_1^2} \text{Tr} \left(\gamma_{\mu'} (\not{p}_- - \not{k} + m) \gamma_{\nu'} (\not{p}_- + m) \gamma_\nu (\not{p}_- - \not{k} + m) \gamma_\mu (\not{p}_+ - m) \right) \right\}. \end{aligned} \quad (4.6)$$

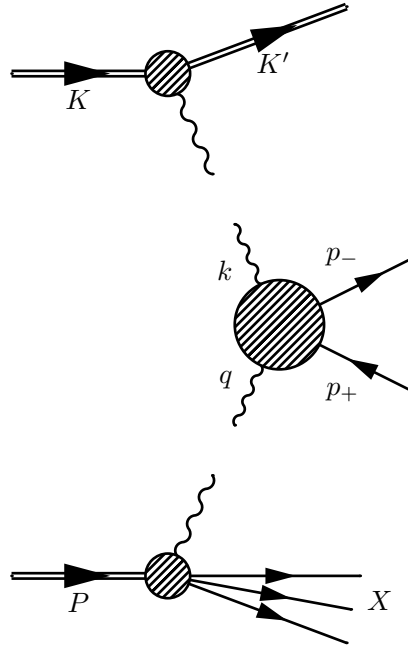


Figure 4.3: For the computation of the matrix element the whole process is split into one leptonic and two hadronic parts, the squares of their amplitudes being represented by tensors.

Here $-x_1$ and $-x_2$ are the denominators of the lepton propagators in the two diagrams

$$-x_1 = (p_- - k)^2 = k^2 - 2p_- \cdot k \quad (4.7)$$

$$-x_2 = (k - p_+)^2 = k^2 - 2p_+ \cdot k. \quad (4.8)$$

The hadronic parts are represented by the hadron tensor introduced in chapter 2. In its most general form, which accounts for all possible transitions from the ground state $|P, S\rangle$ to any excited or multi-particle final state $|X\rangle$, the hadron tensor is parameterized by

$$W_{\mu\mu'} = W_{1P} \left(-g_{\mu\mu'} + \frac{q_\mu q_{\mu'}}{q^2} \right) + \frac{W_{2P}}{M_P^2} \left(P_\mu - \frac{P \cdot q}{q^2} q_\mu \right) \left(P_{\mu'} - \frac{P \cdot q}{q^2} q_{\mu'} \right) \quad (4.9)$$

for the ion with momentum P and mass M_P . Similarly (with $q \rightarrow k$, $P \rightarrow K$, and $M_P \rightarrow M_K$), we obtain the hadron tensor $W_{\nu\nu'}$ for the ion with momentum K and mass M_K . The scalar functions W_i in the hadron tensors are functions of the two invariants q^2 (k^2) and $\nu_q = -P \cdot q / M_P$ ($\nu_k = -K \cdot k / M_K$) in the inelastic case. In the elastic case the two invariants are related via $\nu_q = -q^2 / 2M_P$. For the description of elastic and deep inelastic interactions at the ions, different functions W_i are used (see section 2.3).

The squared matrix element of the complete process is given by the contraction

$$|\mathcal{M}|^2 = M^{\mu\mu'\nu\nu'} W_{\mu\mu'} W_{\nu\nu'}, \quad (4.10)$$

which can be expressed through the scalar functions W_i and eleven independent scalar products of the momenta of the participating particles. We choose these scalar products to be x_1 and x_2 from equations (4.7) and (4.8) and

$$\begin{aligned} x_3 &= \frac{K \cdot q}{M_K}, & x_4 &= \frac{K \cdot \Delta}{M_K}, & x_5 &= \frac{P \cdot k}{M_P}, & x_6 &= \frac{P \cdot \Delta}{M_P}, & x_7 &= \frac{P \cdot K}{M_P M_K}, \\ x_8 &= \frac{K \cdot k}{M_K}, & x_9 &= k^2, & x_{10} &= \frac{P \cdot q}{M_P}, & \text{and } x_{11} &= q^2 \end{aligned} \quad (4.11)$$

with $\Delta = p_- - p_+$.

For completeness we briefly repeat the choices for the response functions W_i we use here, although most of them have already been introduced in chapter 2. For elastic scattering, the main contribution to the cross section comes from the region of small q^2 due to the $1/q^4$ dependence of the matrix element. It is therefore a good approximation to set $\nu_q = 0$, i.e. we neglect the recoil of the heavy ion. Thus the structure functions are given by

$$W_1 = 0 \quad (4.12)$$

$$W_2 = |G_E^A(q^2)|^2 \delta(\nu_q) \quad (4.13)$$

with

$$G_E^A(q^2) = Z \exp\left(\frac{q^2}{2Q_0^2}\right) \quad (4.14)$$

in the elastic case, where we set $Q_0 = 60$ MeV. By using these functions for both ions, we obtain the cross section for elastic scattering, which can be compared to the approximate analytic cross section given by Racah [6] or to other already existing results, e. g. from [7], in order to test our calculation. This cross section, to which we referred to as doubly coherent earlier, gives the dominant contribution to the production of pairs with small transverse momenta. However, if we want to probe the nuclear parton structure, we have to introduce a deep inelastic interaction at one of the nuclei. To that purpose we employ the parton model where the functions W_i are given by

$$W_1^p = \frac{1}{2Mx} F_2^p(x, Q^2) \quad (4.15)$$

$$W_2^p = \frac{2Mx}{Q^2} F_2^p(x, Q^2) \quad (4.16)$$

for a proton target, M being the mass of the proton and F_2^p being its structure function

$$F_2^p(x, Q^2) = \sum_i e_i^2 x f_i(x, Q^2). \quad (4.17)$$

For the PDFs $f_i(x, Q^2)$ of the proton we use the set provided by the Coordinated Theoretical-Experimental Project on QCD (CTEQ) [55]. For a heavy ion target the response functions W_i are given by

$$W_1^A = \frac{1}{2M_A x_A} F_2^A(x, Q^2) = \frac{1}{2Mx} F_2^A(x, Q^2) \quad (4.18)$$

$$W_2^A = \frac{2M_A x_A}{Q^2} F_2^A(x, Q^2) = \frac{2Mx}{Q^2} F_2^A(x, Q^2) \quad (4.19)$$

with the structure function

$$F_2^A = Z \cdot F_2^p(x, Q^2) + (A - Z) \cdot F_2^n(x, Q^2). \quad (4.20)$$

In F_2^p and F_2^n we can use either the free PDFs of CTEQ, assuming $f_{u(\bar{u})}^n = f_{d(\bar{d})}^p$ and $f_{d(\bar{d})}^n = f_{u(\bar{u})}^p$, or we can account for nuclear effects by multiplying the free PDFs by flavor dependent factors

$$f_i^{p|A}(x, Q^2) = R_i(x, Q^2) \cdot f_i^p(x, Q^2). \quad (4.21)$$

Two parameterizations for these factors are given by Eskola et al. [33, 34] and by Frankfurt et al. [31, 32] (for details see section 2.3).

For the generation of the phase space and the numerical integration we use the methods introduced in the appendices C and B, respectively.

4.2.2 Results for Elastic and Deep Inelastic Pair Production

As already discussed there are two kinematic regions where the cross section of pair production in the collision of two ions is enhanced: the double-photon pole region and the photon-lepton pole region. Furthermore, we discussed the different event signatures of these two processes. In the intuitive picture provided by the ELA, which we expect to be valid when deep inelastic scattering occurs at one of the ions, one of the leptons obtains a large transverse momentum from the highly virtual photon, while the other lepton acts as a spectator and proceeds in forward direction. The leptons in this process are thus expected to show an asymmetric distribution of their transverse momenta. In contrast, in the doubly coherent process are produced back to back in the transverse plane, i. e. having equal transverse momenta. We test these qualitative statements quantitatively by comparing differential cross sections as functions of the transverse momenta of the leptons from both contributions. In the calculation of the deep inelastic pair production, we sort the leptons by their transverse momenta. We refer to the lepton with the larger transverse momentum as the 'DIS lepton', because we assume it to be related to the deep inelastic interaction. The lepton with smaller transverse momentum is referred to as 'spectator lepton'. The leptons in the elastic process are sorted in the same way, although we do not expect to see a difference in the p_{\perp} -distribution of the two leptons, as already discussed above.

In Fig. 4.4 we present the differential cross section as function of the transverse momenta of the leptons in elastic and deep inelastic electron-positron pair production in Pb-Pb collisions at the LHC. This plot confirms all the above predictions. The elastic cross section is dominant at small transverse momenta of the leptons and the leptons have equal transverse momenta. However, if we select events requiring the transverse momentum of one of the leptons to be larger than 2 GeV (see Fig. 4.5 for muon pair production), the elastic and the deep inelastic cross section are similar in size. In addition, the DIS lepton is always accompanied by a lepton with smaller transverse momentum. This confirms the unique event characteristic of pair production with one elastic and one deep inelastic interaction, predicted above, and permits to distinguish between the doubly coherent and the DIS contribution.

In the following, we further investigate the pair production from DIS, since this is the process we are interested in. In Fig. 4.6 we show the differential cross section as function of the transverse momentum of the DIS lepton for muon and electron pair production in Pb-Pb collisions and for electron pair production in Pb-p collisions at the LHC. For transverse momenta larger than ~ 2 GeV electron and muon pair production have similar cross sections and are therefore of equal interest. In Fig. 4.7 we compare the differential cross sections as functions of the transverse momentum of the DIS lepton ($p_{\perp\text{max}}$), the spectator lepton ($p_{\perp\text{min}}$), and the struck quark ($p_{\perp\text{quark}}$) for electron pair production in Pb-Pb collisions. The spectator lepton distribution peaks at small values, while at large p_{\perp} it is an order of magnitude smaller than the distribution of the DIS lepton, which is, in addition, balanced by the quark transverse momentum distribution. The rapidity distributions of the muon, the anti-muon, and the struck quark in Pb-Pb collisions can be seen in Fig. 4.8. Fig. 4.9 shows the same as Fig. 4.8 but with a 2 GeV-cut applied to the transverse momentum of the DIS lepton.

Furthermore, it is interesting to investigate whether the Bjorken x -regime, in which free (Pb-p collisions) and nuclear (Pb-Pb collisions) PDFs can be studied, can be extended in Pb-Pb and Pb-p collisions as compared to fixed target experiments or electron proton colliders. In Figs 4.10 and 4.11 we present differential cross sections as functions of Bjorken x in Pb-Pb collisions for muon pair production and in Pb-p collisions for electron pair production. In the lower left of the plots, we show another plot, where we have a closer look at the $x < 0.1$ -regime. In both Pb-Pb and Pb-p collisions this is the dominant region. However, if we are interested in events with $p_{\perp\text{max}}$ larger than ~ 2 GeV for the cross section not to be overwhelmed by the doubly coherent process, the pronounced peak in the $x < 0.1$ region vanishes, as can be seen in Fig. 4.12. In Fig 4.13 we show the differential cross section as function of x for muon pair production in Pb-Pb

collisions on a logarithmic x -scale. The solid line is the 'complete' differential cross section, the dashed line is the differential cross section with a $p_{\perp max} > 2$ GeV cut applied.

In the regime $x < 0.1$ nuclear shadowing plays an important role, but this region is up to now only probed at small momentum transfers Q^2 . In order to see how the values of x and Q^2 are correlated in this process, we show the cross section for electron pair production as function of Bjorken x and the momentum transfer Q^2 in Fig. 4.14.

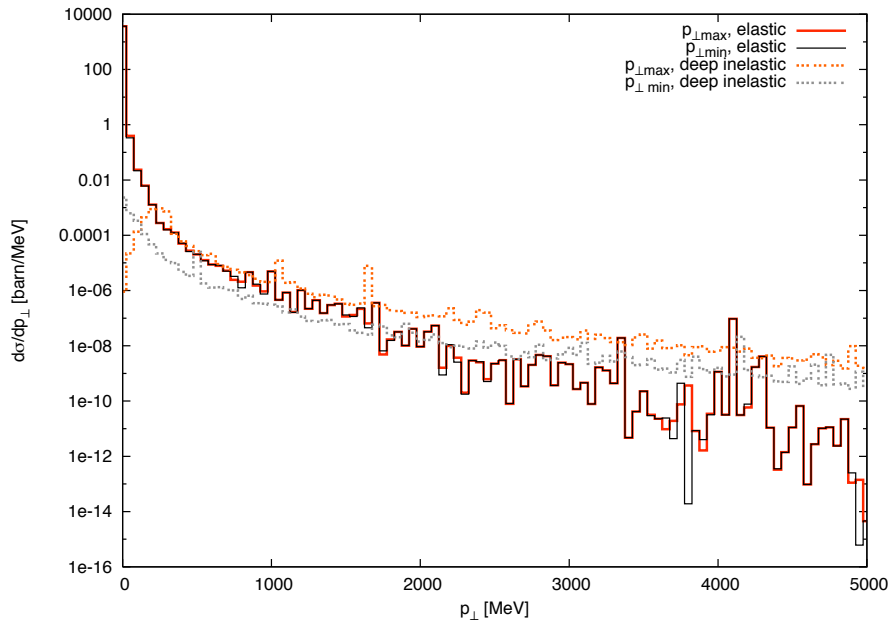


Figure 4.4: Differential cross section as function of the transverse momenta of the two leptons (sorted by the size) for electron-positron pair production from elastic and deep inelastic scattering in Pb-Pb collisions at the LHC.

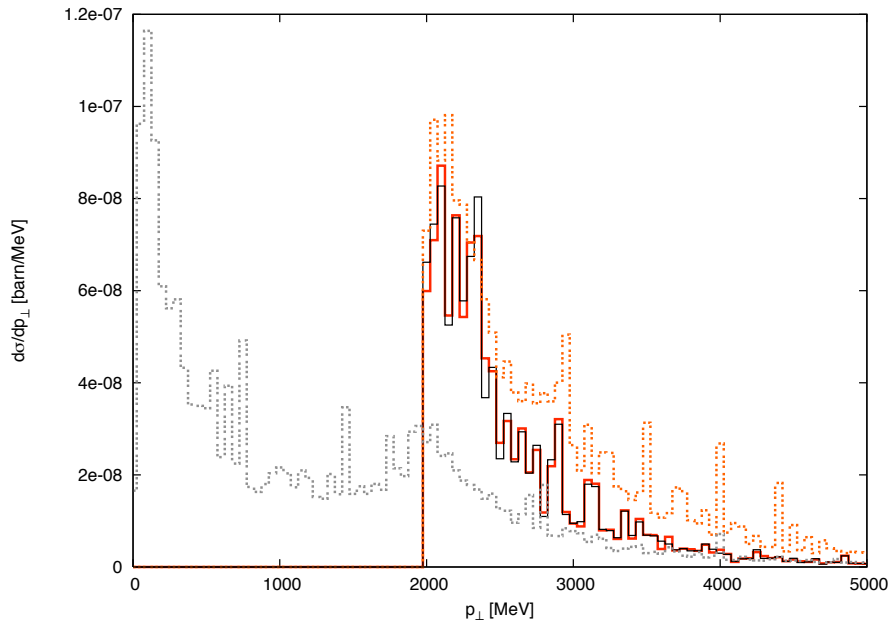


Figure 4.5: Differential cross section as function of the transverse momenta of the two leptons for muon pair production from elastic and deep inelastic scattering in Pb-Pb collisions at the LHC. Here only those events are counted, where at least one of the leptons has a transverse momentum larger than 2 GeV.

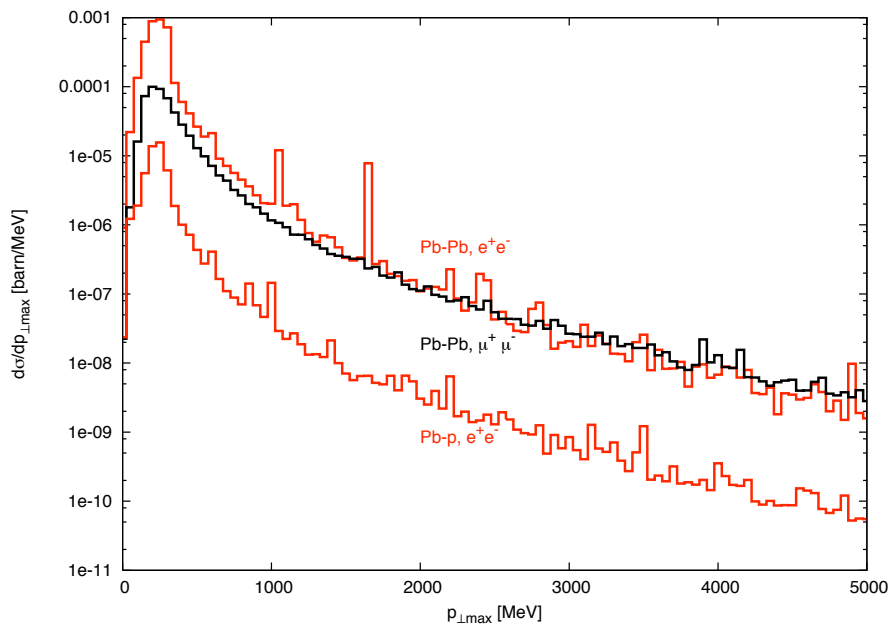


Figure 4.6: Differential cross section as function of the transverse momentum of the DIS lepton for electron and muon pair production Pb-Pb collisions and for electron pair production in Pb-p collisions at LHC energies.

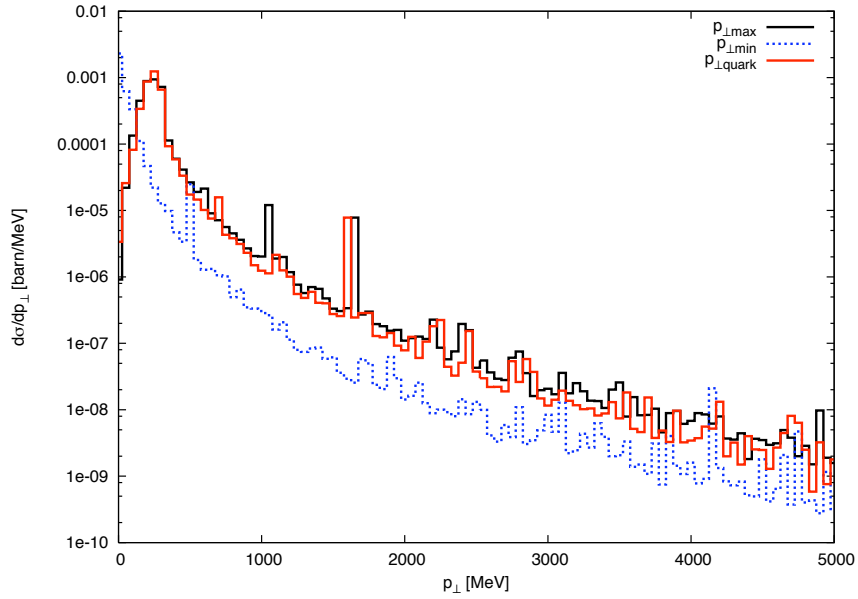


Figure 4.7: Differential cross section as function of the transverse momentum of the DIS lepton, the spectator lepton, and the struck quark for electron pair production Pb-Pb collisions at LHC energies.

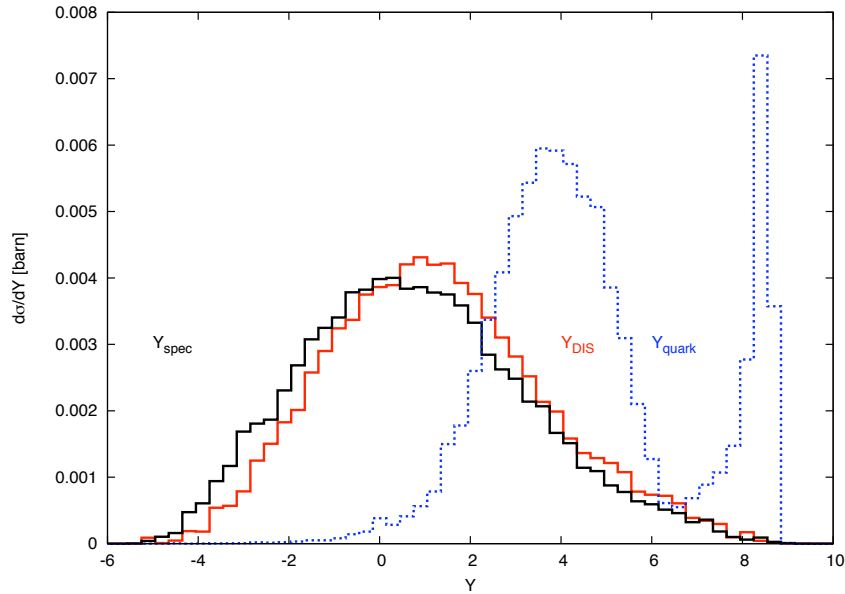


Figure 4.8: Differential cross section as function of the rapidities of the two leptons and the struck quark for muon pair production from deep inelastic scattering in Pb-Pb collisions at the LHC.

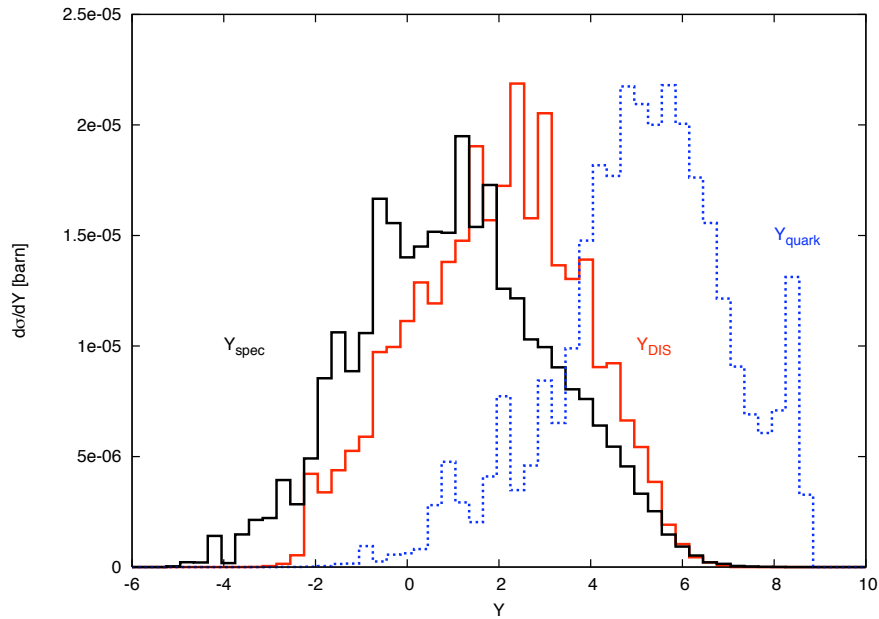


Figure 4.9: Differential cross section as function of the rapidities of the two leptons and the struck quark for muon pair production from deep inelastic scattering in Pb-Pb collisions with a $p_{\perp} > 2$ GeV-cut.

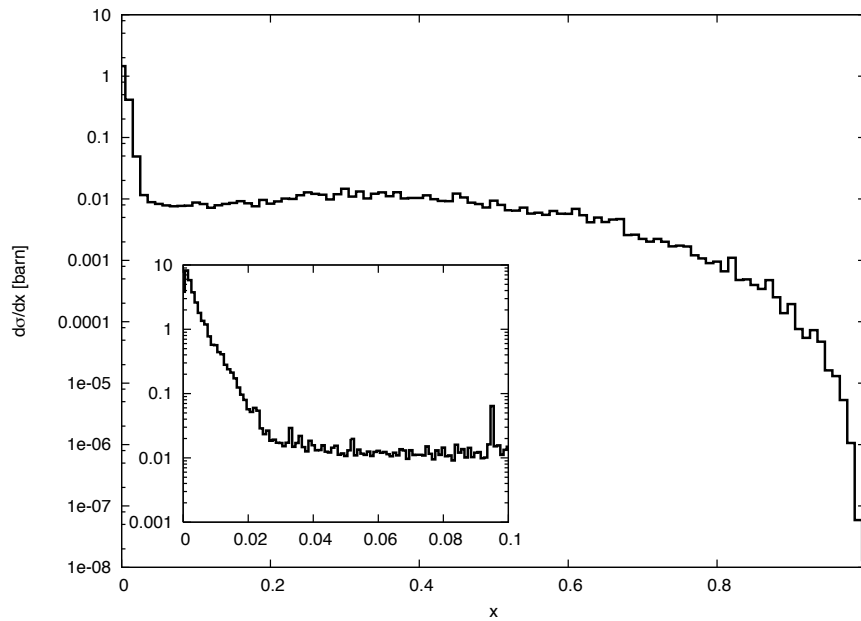


Figure 4.10: Differential cross section as function of Bjorken x for muon pair production from deep inelastic scattering in Pb-Pb collisions at the LHC.

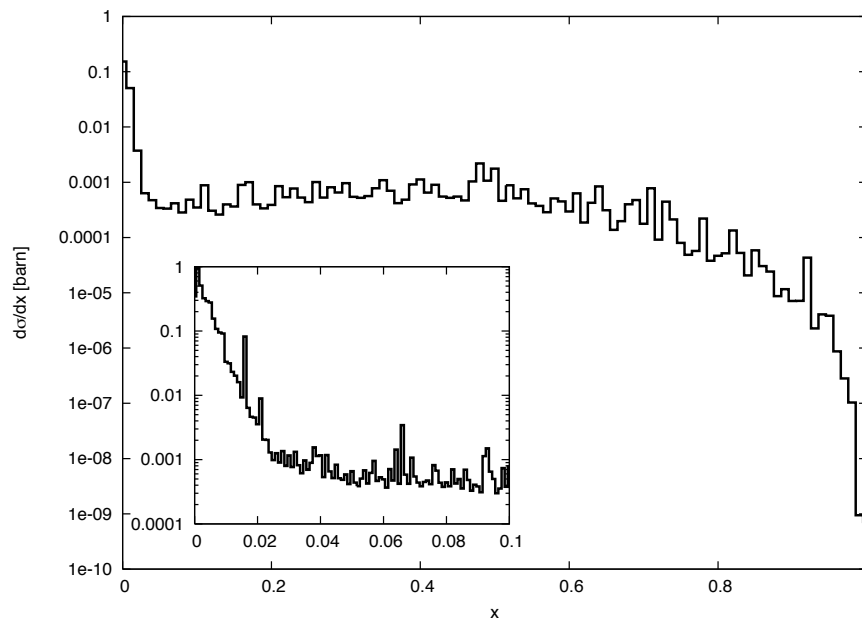


Figure 4.11: Differential cross section as function of Bjorken x for electron pair production from deep inelastic scattering in Pb-p collisions at the LHC.

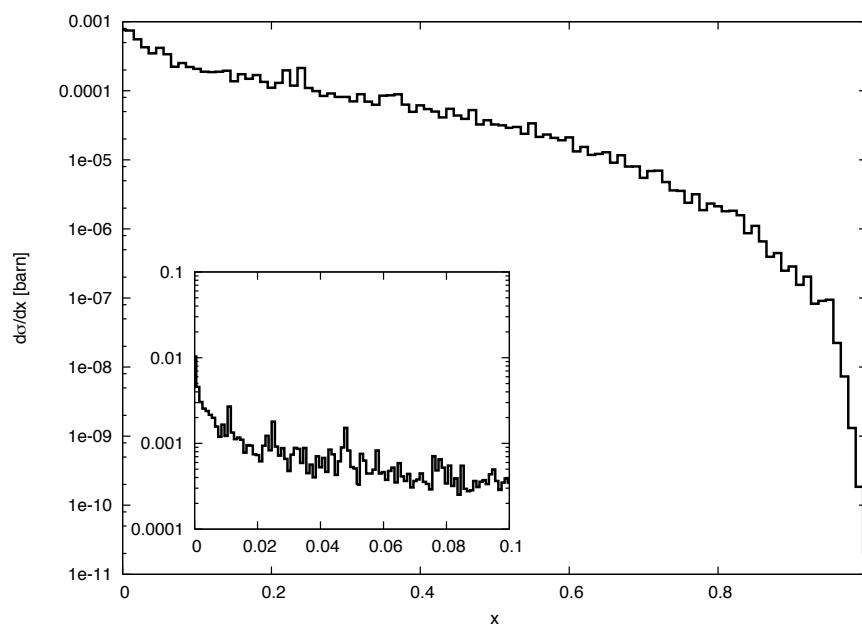


Figure 4.12: Differential cross section as function of Bjorken x for muon pair production from deep inelastic scattering in Pb-Pb collisions at the LHC with a $p_{\perp\text{max}} > 2$ GeV-cut.

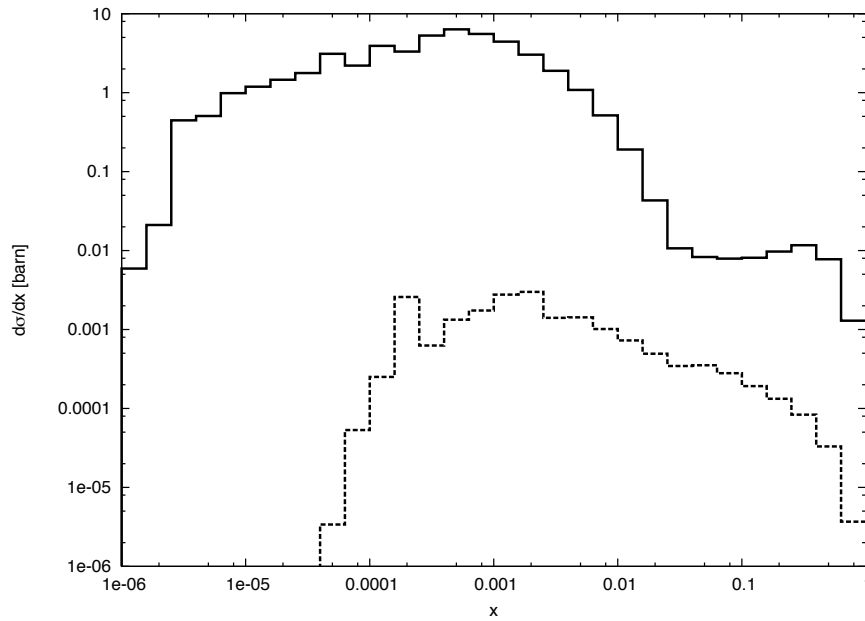


Figure 4.13: Differential cross section as function of Bjorken x for muon pair production from deep inelastic scattering in Pb-Pb collisions at the LHC on a logarithmic x -scale with (dashed line) and without (solid line) a $p_{\perp\max} > 2$ GeV-cut.

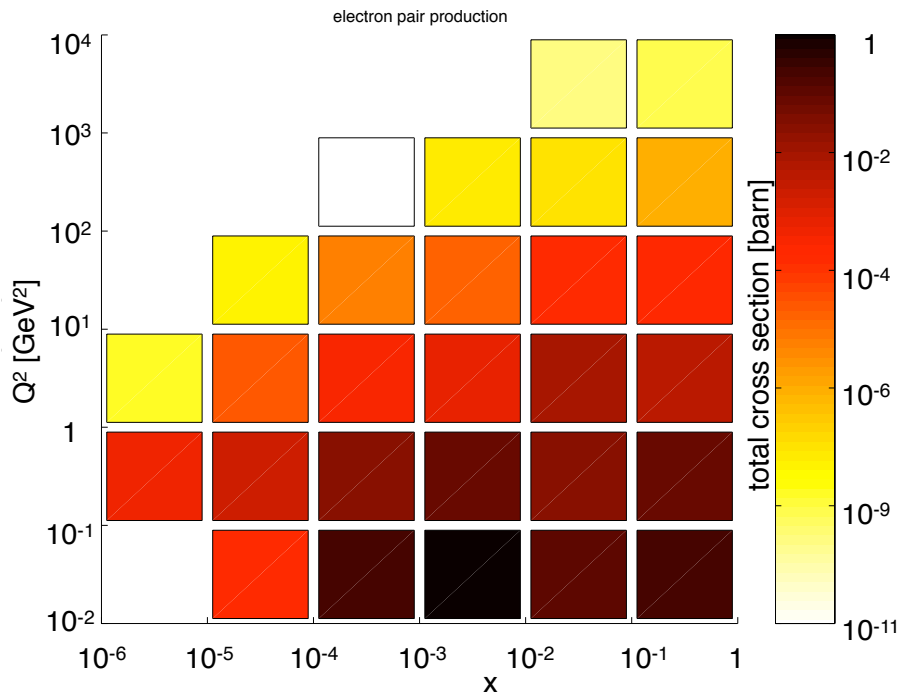


Figure 4.14: Total cross section in barn as function of Bjorken x and Q^2 for electron pair production in Pb-Pb collisions.

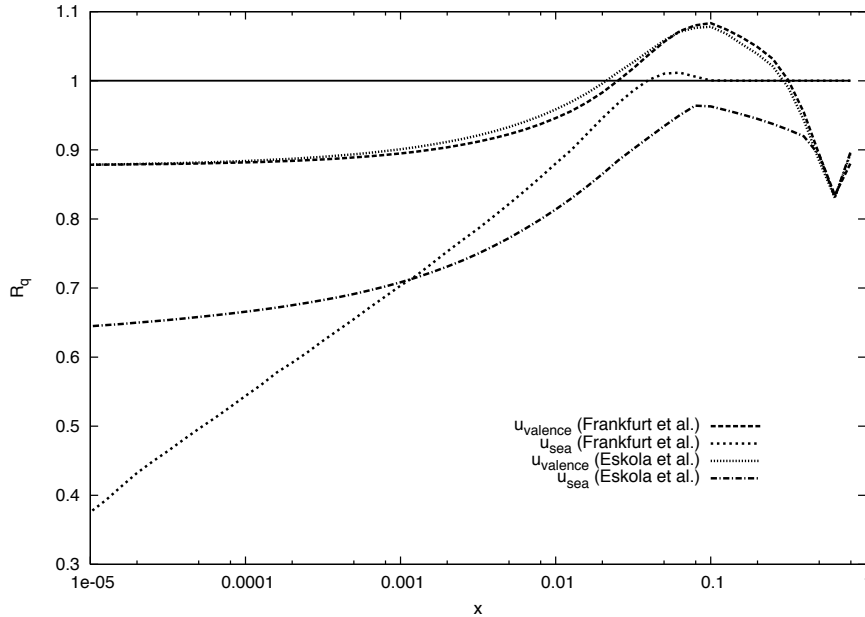


Figure 4.15: Flavor dependent factors $R_q = \frac{f_i^A(x, Q^2)}{Af_i^P(x, Q^2)}$, which account for nuclear modifications, as function of x at a fixed value of $Q = 2$ GeV, for valence and sea u-quarks from two different parameterizations.

4.2.3 Nuclear Modifications

As already mentioned above, we can account for nuclear structure by multiplying the free PDFs from CTEQ [55] by flavor dependent factors

$$f_i^{p|A}(x, Q^2) = R_i(x, Q^2) \cdot f_i^P(x, Q^2). \quad (4.22)$$

There exist two parameterizations for these factors in the kinematic region $10^{-5} \lesssim x \lesssim 1$ and $2 \text{ GeV} < Q < 100 \text{ GeV}$ provided by Frankfurt et al. [31, 32] and Eskola et al. [33, 34]. The two approaches which lead to these parameterizations are briefly discussed in section 2.3 of this work. In Fig. 4.15 we show the correction factors from both groups for valence and sea u-quarks at a fixed value of $Q^2 = 4 \text{ GeV}^2$ and as a function of Bjorken x . We now include these nuclear modifications into our calculations and compare the results with those using free PDFs in Figs. 4.16-4.18. The calculations are performed in the kinematic range given by the sets of correction factors: $2 \text{ GeV} \leq Q \leq 100 \text{ GeV}$. Since a limitation of Q also limits the transverse momentum of the DIS lepton, we additionally apply a cut on the transverse momentum of the DIS lepton $p_{\perp DIS} > 2 \text{ GeV}$. For the calculations using free PDFs to be comparable to those with the nPDFs, we have performed these calculations in the same kinematic range, i. e. $2 \text{ GeV} \leq Q \leq 100 \text{ GeV}$ and $10^{-5} \leq x \leq 0.95$. Therefore the differential cross sections using free PDFs are different from those presented in section 4.2.2, where they were calculated in the kinematic range given by the CTEQ set, i. e. $0.3 \text{ GeV} \leq Q \leq 10000 \text{ GeV}$ and $10^{-6} \leq x \leq 1$. We compare differential cross sections as function of the transverse momentum of the DIS lepton (Fig. 4.16), Bjorken x (Fig. 4.17), and the rapidity of the DIS lepton (Fig. 4.18). The sensitivity to the nuclear modifications is largest at small x and p_{\perp} and at rapidities of the DIS lepton around $Y \sim 0$.

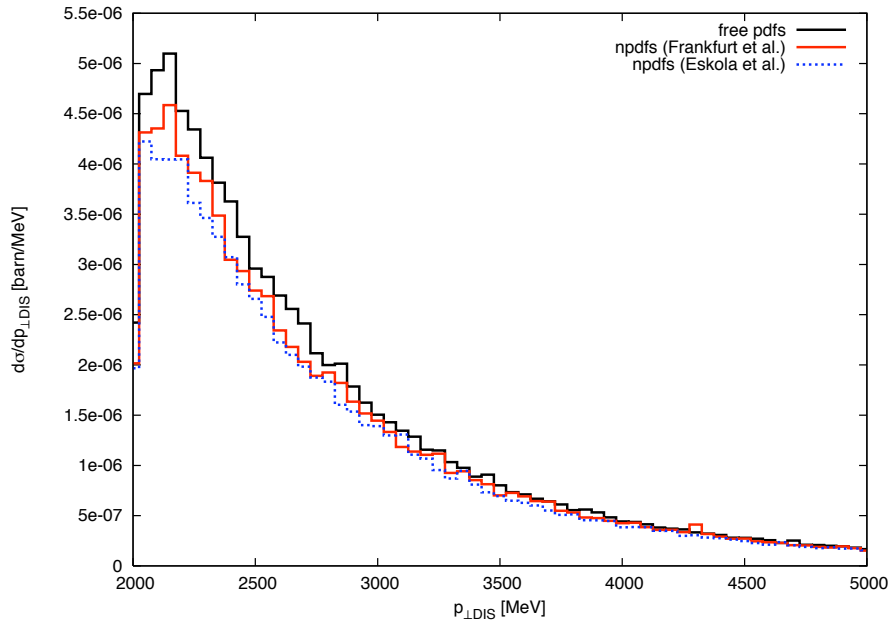


Figure 4.16: Differential cross section as function of the transverse momentum of the DIS lepton for muon pair production from deep inelastic scattering in Pb-Pb collisions. We compare the differential cross sections of calculations using free PDFs with those of calculations employing the parameterizations of Frankfurt et al. [31, 32] and Eskola et al. [33, 34] to account for nuclear modifications.

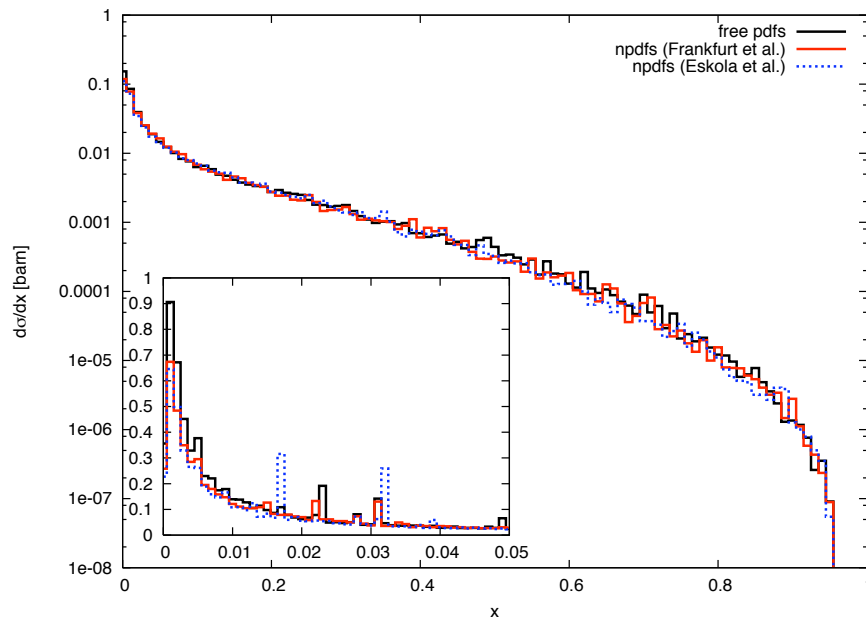


Figure 4.17: Differential cross section as function of Bjorken x for muon pair production from deep inelastic scattering in Pb-Pb collisions. We compare the differential cross sections of calculations using free PDFs with those of calculations employing the parameterizations of Frankfurt et al. [31, 32] and Eskola et al. [33, 34] to account for nuclear modifications.

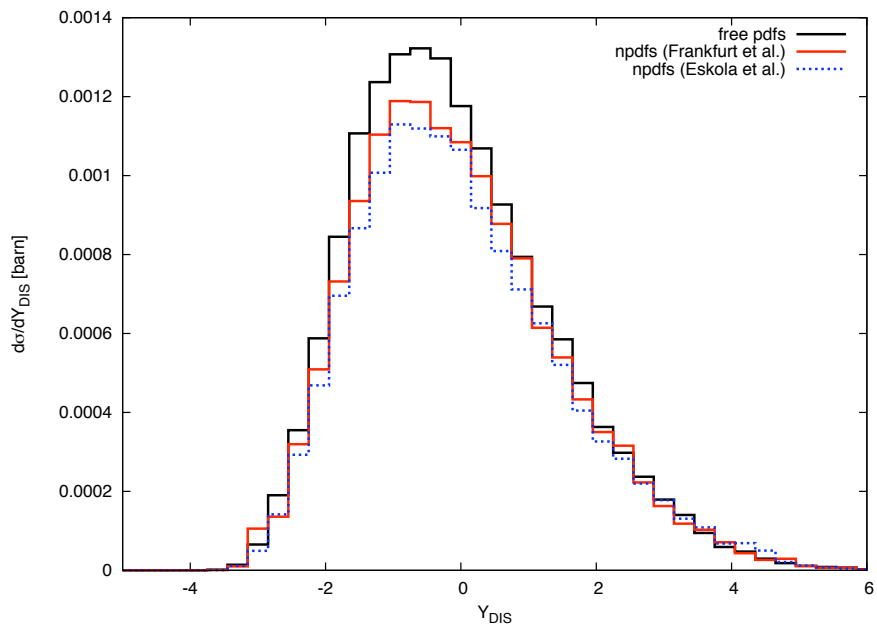


Figure 4.18: Differential cross section as function of the rapidity of the DIS lepton for muon pair production from deep inelastic scattering in Pb-Pb collisions. We compare the differential cross sections of calculations using free PDFs with those of calculations employing the parameterizations of Frankfurt et al. [31, 32] and Eskola et al. [33, 34] to account for nuclear modifications.

4.3 Lepton Pair Production from Deep Inelastic Scattering in the Equivalent Photon and the Equivalent Lepton Approximation

In the previous section we confirmed that lepton pair production from DIS indeed shows the event characteristic predicted by the ELA-picture: One lepton, the DIS lepton, obtains a relatively large transverse momentum as compared to the second lepton. The DIS lepton p_{\perp} -distribution is additionally balanced by the transverse momentum distribution of the quark. In this section, we want to examine whether the EPA and the ELA are also valid quantitatively. To this purpose we calculate the cross section for pair production from deep inelastic scattering in the equivalent photon and the equivalent lepton approximation.

Due to the coherent action of all the charges in the nucleus, relativistic nuclei have photons as important constituents. The coherence condition limits the virtuality of the photon to $-k^2 \leq \frac{1}{R^2}$, R being the size of the nucleus, which means that the wavelength of the photon is larger than the nucleus and does not resolve individual nucleons in the nucleus. This is the case for the elastic part of the pair production process, we are interested in here, and we can apply the EPA, as it is introduced in chapter 3 of this work. In this approximation, we convolve the equivalent photon spectrum

$$f_{\gamma|A}(u) = \frac{2\alpha Z^2}{\pi u} \log\left(\frac{1}{uM_K R}\right) \quad (4.23)$$

of the ion with the cross section for pair production from a real photon $\sigma_{\gamma A}$ (Fig. 4.19)

$$\sigma_{AA} = \int du f_{\gamma|A}(u) \sigma_{\gamma A}(u \cdot E_K). \quad (4.24)$$

The matrix element for pair production from a real and a virtual photon, which has already been derived by Walecka et al. in [54], is obtained by contracting the hadron tensor

$$W_{\mu\mu'} = W_{1P} \left(-g_{\mu\mu'} + \frac{q_{\mu}q_{\mu'}}{q^2} \right) + \frac{W_{2P}}{M_P^2} \left(P_{\mu} - \frac{P \cdot q}{q^2} q_{\mu} \right) \left(P_{\mu'} - \frac{P \cdot q}{q^2} q_{\mu'} \right), \quad (4.25)$$

where the structure functions W_i for deep inelastic scattering are given in equations (4.18), (4.19) and (4.20), with the leptonic tensor $M^{\mu\mu'}$ for two-photon pair production from a real and a virtual photon. For the calculation of the matrix element we proceed in an analogous manner as for the pair production from two virtual photons described in section 4.2.

A further simplification can be achieved by treating the intermediate lepton as quasi-real as well, assuming photon splitting into an almost collinear lepton pair. The spectrum of equivalent leptons in the photon can be derived from the matrix element of the lepton photon vertex, assuming small transverse momenta of the emitted particles and high energies (compare section 3.2). The equivalent lepton spectrum in a photon is given by

$$f_{l|\gamma}(\omega, z) = \frac{\alpha}{\pi} \log\left(\frac{\omega}{m}\right) [z^2 + (1-z)^2] \quad (4.26)$$

and the spectrum of leptons in the ion is given by the convolution of the distribution of leptons in the photon with the distribution of photons in the nucleus

$$f_{l|A}(y) = \int \frac{du}{u} f_{\gamma|A}(u) f_{l|\gamma}\left(\omega = uE_K, z = \frac{y}{u}\right). \quad (4.27)$$

This spectrum is convolved with the cross section for deep inelastic lepton scattering discussed in detail in chapter 2 to yield the total cross section in the equivalent lepton approximation

$$\sigma_{AA} = \int dy f_{l|A}(y) \sigma_{lA}. \quad (4.28)$$

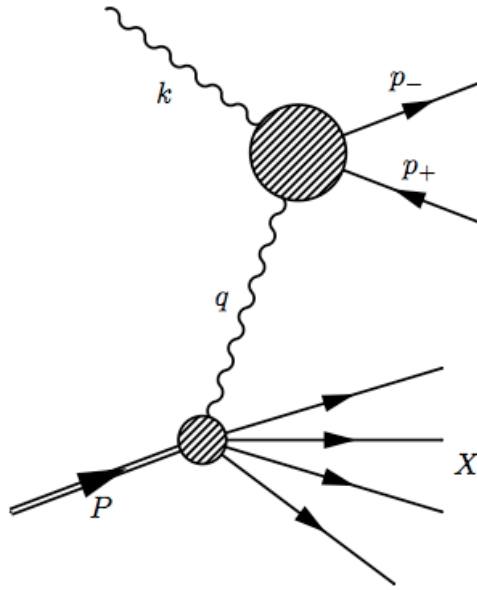


Figure 4.19: Schematic diagram for pair production from one real and one deep inelastic photon.

In Figs 4.20-4.22 we compare the differential cross sections as functions of the transverse momenta of the DIS lepton (Fig. 4.20), the rapidity of the DIS lepton (Fig. 4.21), and Bjorken x (Fig. 4.22, respectively), of the full calculation to the corresponding differential cross sections derived in the EPA and the ELA. As in the full calculation we use the transverse momentum of the leptons as criterion to distinguish between the DIS lepton and the spectator lepton in the EPA as well. In the ELA there is only one lepton: the D—S lepton. From Fig. 4.20 we conclude that the p_{\perp} -criterion for the distinction between the two leptons in the EPA and the full calculation is reasonable, as the shape of these cross sections resembles that of the ELA. However, from the differential cross sections in Figs 4.20-4.22 we see that the ELA consistently overestimates the cross section derived from the full calculation while the EPA works sufficiently well. To get an idea why the EPA succeeds in reproducing the results of the full calculation while the ELA does not, we check the validity of the approximations we made in the two methods. In the derivation of the equivalent particle approximations, the equivalent particles are assumed to have small transverse momenta. To test this assumption, we calculate the differential cross section as function of the transverse momenta of those particles in the full calculation, which are treated as equivalent particles in the EPA and the ELA. These particles are the photon from the elastic part of the process, the spectator lepton, and the intermediate lepton. In Fig. 4.23 we present the result of this study. As the equivalent particles are expected to proceed in forward direction, their transverse momenta should be close to zero for the approximations to be good. This is obviously the case for the photon. In contrast, the leptons have contributions to the cross section up to quite high transverse momenta. This behavior explains why the equivalent lepton approximation overestimates the cross section. Large transverse momenta enlarge the denominator of the propagator, which leads to a smaller value for the cross section in the full calculation than is expected in the ELA.

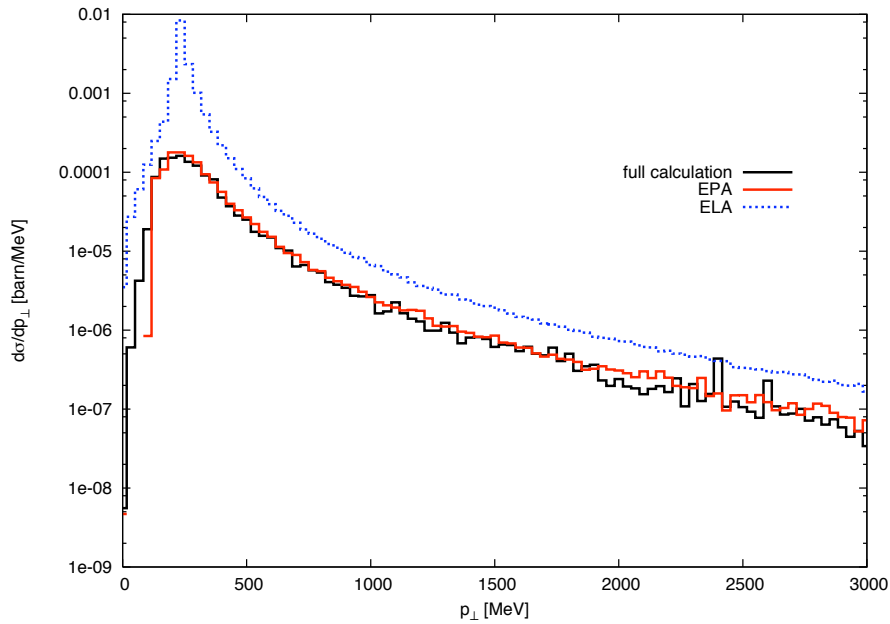


Figure 4.20: Differential cross section as function of the transverse momentum of the DIS lepton for muon pair production in Pb-Pb collisions. Comparison between the full calculation, the calculation employing the equivalent photon approximation and the calculation employing the equivalent lepton approximation.

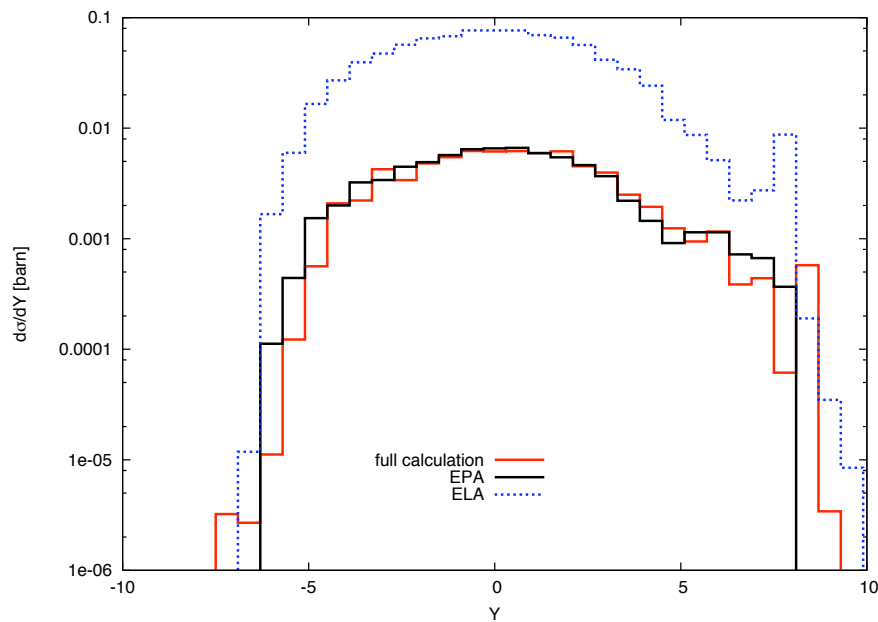


Figure 4.21: Differential cross section as function of the rapidity of the DIS lepton for muon pair production in Pb-Pb collisions. Comparison between the full calculation, the calculation employing the EPA and the calculation employing the ELA.

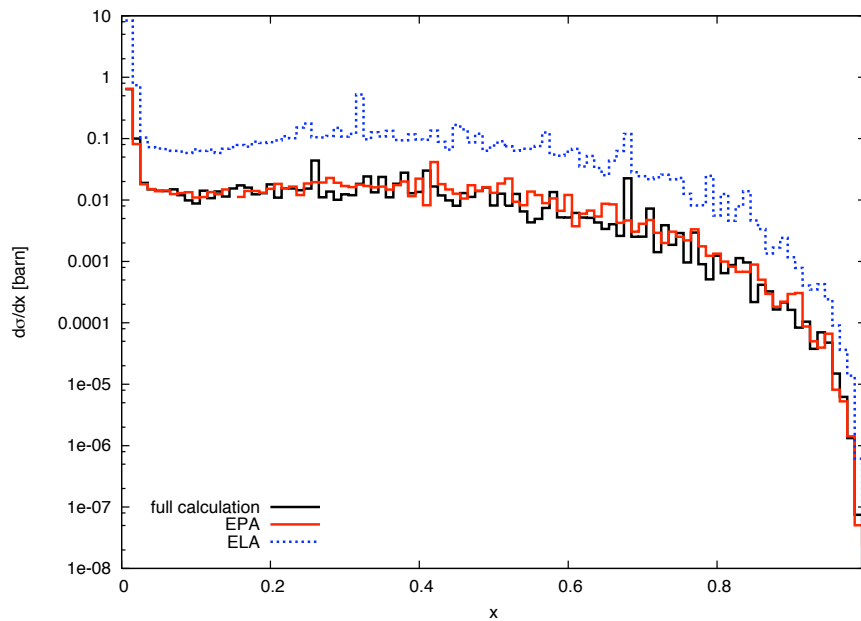


Figure 4.22: Differential cross section as function of Bjorken x for muon pair production in Pb-Pb collisions. Comparison between the full calculation, the calculation employing the EPA and the calculation employing the ELA.

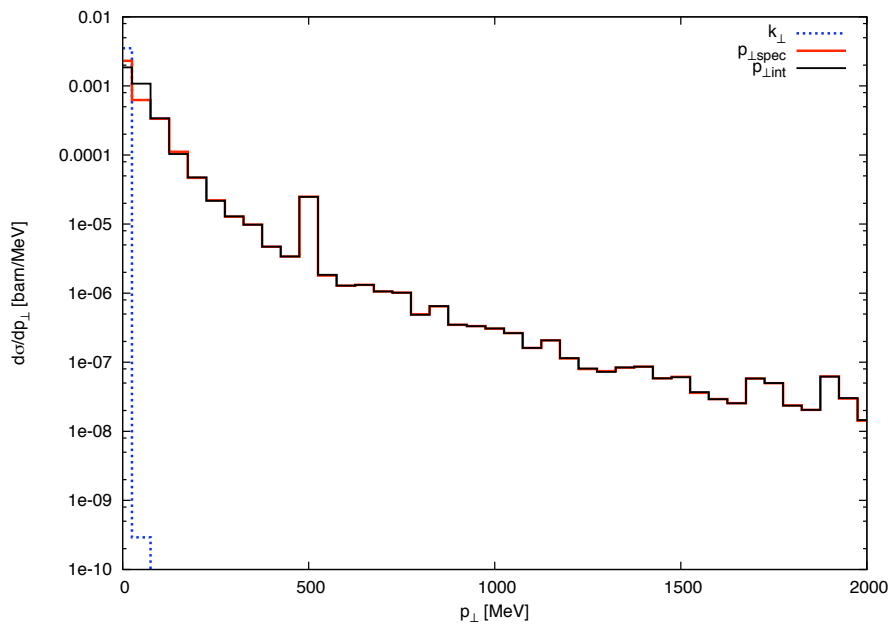


Figure 4.23: Differential cross section as function of the transverse momenta of the particles treated as equivalent particles in the EPA and the ELA for muon pair production in Pb-Pb collisions.

4.4 Conclusions

We identified two kinematic regions contributing about equally to the two-photon lepton pair production in ultra-peripheral heavy ion collisions at large transverse momenta of at least one of the leptons. The contribution with one elastic and one deep inelastic interaction at the ions is especially interesting, since it offers the possibility to study the nuclear parton content. We calculated differential cross sections for two-photon pair production in this kinematic region in order to identify the regions where viable amounts of events can be expected.

Furthermore, we performed calculations including nuclear corrections to the PDFs provided by Eskola et al. [33, 34] and Frankfurt et al. [31, 32] and compare them to calculations using free PDFs. When the nuclear corrections to the PDFs are applied, the cross sections are suppressed in nearly all regions. The differences between the two parameterizations are best seen e.g. in the differential cross section as function of the rapidity of the DIS lepton at values around $-1 \lesssim Y \lesssim 0$. In addition, we calculated differential cross sections in the equivalent photon and the equivalent lepton approximation. We compare them to the results of the full calculation and by this means provide a test of the validity of these approximations. In conclusion, the cross sections calculated in the equivalent photon approximation reproduce the ones from the full calculation quite well, whereas the equivalent lepton approximation consistently overestimates the cross sections. This is due to the fact that the assumption that the equivalent particles - the spectator and the intermediate lepton in the full calculation - fly in forward direction is scarcely fulfilled in this kind of process. There are contributions to the cross section coming from the region of quite large transverse momenta of these particles. Nevertheless, the results confirm that the intuitive picture provided by the ELA, where one of the leptons is directly related to the large momentum transfer and therefore to the deep inelastic scattering, is still applicable.

Single W Production in p-p and p-A Collisions at LHC

5.1 Introduction

The Standard Model has been checked extensively and to high precision in the last couple of decades. Only few sectors still remain unchecked, one of which is the electroweak coupling of the gauge bosons. A process which is well suited to test our understanding of the gauge boson self-interaction is the photoproduction of single W bosons off a nucleon. In particular, this process is sensitive to the triple gauge boson ($WW\gamma$) coupling and thus to the anomalous magnetic moment κ_W of the W boson.

Inclusive W production has been searched for at HERA. Breitweg et al. [11] report three events consistent with $W \rightarrow e\nu$ decay, yielding a cross section of ~ 1 pb, which is in agreement with Standard Model predictions [9, 10]. In p-p and p-A collisions at the LHC at CERN higher luminosities and therefore higher rates can be expected. In the framework of the equivalent photon approximation [40, 41, 42, 47, 8], introduced in chapter 3, the protons and ions at relativistic hadron colliders act as a source of high energy photons, which can be used to study photoproduction processes.

The production rate of single W bosons in ultraperipheral p-p or p-A collisions can be determined either from the convolution of the equivalent photon spectrum with the exclusive process

$$\gamma + p \longrightarrow W^+ + n \quad (5.1)$$

or the corresponding inclusive process. While the cross section for the inclusive process is expected to be larger [12], the exclusive process has the advantage of a rather unique signature: a neutron in forward direction with about the energy of the initial proton. Since this neutron can be detected in the Zero Degree Calorimeter, background can be reduced significantly. We will focus on the exclusive process throughout the rest of this chapter.

First, we calculate the cross section for real photoproduction of single W bosons and cross-check our results with those of Fearing et al. [13, 14], who have calculated this cross section with a smaller W boson mass in mind. Next, we extend the calculations of Fearing et al. by including a weak magnetic form factor and the correct W boson mass, and convolve the photoproduction cross section with the equivalent photon spectra of ions and protons [8, 47, 50]. We show how the choice of the weak timelike form factors affects the sensitivity of the total cross section to the anomalous magnetic moment of the W boson. Furthermore, we give an estimate of the total cross sections for p-p and p-Pb collisions at the LHC. Finally, we present differential cross sections as functions of the rapidities and energies of the neutron, the photon parent, the W boson, and the leptonic decay products of the W boson.

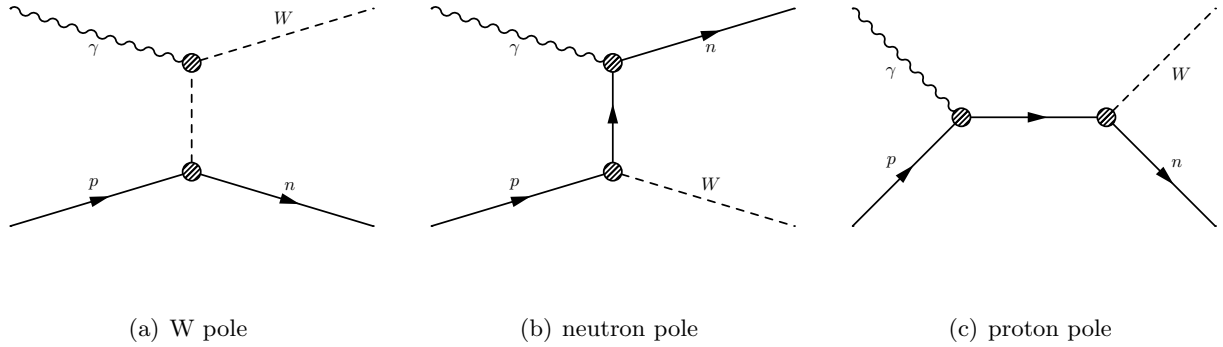


Figure 5.1: Relevant Feynman diagrams for single W boson photoproduction.

5.2 Photoproduction of W Bosons

In this section we summarize the derivation of the cross section for the photoproduction of single W bosons from a proton (5.1). We include the three diagrams of Fig. 5.1 in our calculation of the matrix element: the W boson pole (Fig. 5.1(a)), which is the one we are interested in, the neutron pole (Fig. 5.1(b)), and the proton pole (Fig. 5.1(c)) diagrams. These diagrams are expected to give the main contribution to the W production cross section [13, 14, 56]. Since in all three diagrams the W boson is produced at a hadronic vertex, appropriate electromagnetic and weak form factors have to be included in realistic calculations to account for the extended structure of the nucleons (see chapter 2 for details). In Fig. 5.1 those vertices, where we employ form factors, are indicated by shaded circles.

Interactions of Fermions and Gauge Bosons

The interactions needed to write down the matrix elements corresponding to the Feynman diagrams in Fig. 5.1 are depicted in Fig. 5.2. The electromagnetic nucleon-nucleon vertex $\Gamma_\mu^{\gamma NN}$ (Fig. 5.2(a)) has the standard form

$$\Gamma_\mu^{\gamma NN} = -ie \left[F_1^N(k^2) \gamma_\mu + i \frac{\kappa_N}{2M_N} F_2^N(k^2) \sigma_{\mu\nu} k^\nu \right] \quad (5.2)$$

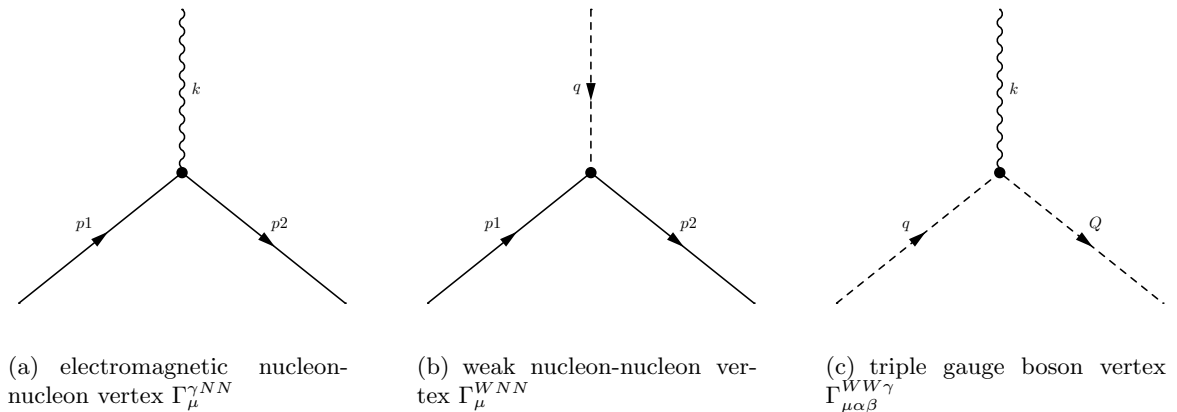


Figure 5.2: Interaction vertices needed for the calculation of the matrix element of reaction (5.1).

as introduced in section 2.2. Since the photon in this process is real or quasi-real (in the EPA), i.e. $k^2 \approx 0$, we need the electromagnetic form factors in their static limit only

$$F_1^p(0) = F_2^p(0) = F_2^n(0) = 1 \quad (5.3)$$

$$F_1^n(0) = 0. \quad (5.4)$$

The weak proton-neutron-W vertex Γ_μ^{WNN} (Fig. 5.2(b)) is given by

$$\Gamma_\mu^{WNN} = \frac{-ig \cos \vartheta_C}{2\sqrt{2}} [F_V(q^2)\gamma_\mu + iF_M(q^2)\sigma_{\mu\nu}q^\nu + F_A(q^2)\gamma_\mu\gamma_5] \quad (5.5)$$

with $g^2 = 8M_W^2 G_F/\sqrt{2}$, the Fermi constant $G_F = 1.1664 \cdot 10^{-5} \text{GeV}^{-2}$, $\cos \vartheta_C = 0.98$, the W boson mass M_W^2 , and the form factors in the spacelike region as explained in section 2.4. For the axial weak form factor $F_A(q^2)$ we use a dipole form with the parameter $m_A = 0.95 \text{GeV}$ obtained by Mann et al. [37]. In the timelike region, which is the important region for the diagrams in Figs. 5.1(b) and 5.1(c), where we have a momentum transfer of $Q^2 = M_W^2$, the form factors are almost unknown. Fearing et al. [13, 14] and Kallianpur [56] present in their papers results for two choices of timelike form factors:

- (i) constant timelike form factors $F_{V|M|A}(Q^2) = F_{V|M|A}(0)$ and
- (ii) dipole timelike form factors with the same dipole form as in the spacelike region.

We will discuss both choices.

For the triple gauge boson vertex (Fig. 5.2(c)) we use the following form

$$\Gamma_{\mu\alpha\beta}^{WW\gamma} = ie \{F_1^W(k^2) [(q+Q)_\mu g_{\alpha\beta} - Q_\alpha g_{\mu\beta} - q_\beta g_{\mu\alpha}] + \kappa_W F_2^W(k^2) [k_\beta g_{\mu\alpha} - k_\alpha g_{\mu\beta}]\} \quad (5.6)$$

which allows for an arbitrary magnetic moment of the W boson [57]. κ_W can be used as a parameter to test the sensitivity of the cross section to the $WW\gamma$ coupling. The Standard Model $WW\gamma$ coupling is recovered for $\kappa_W = 1$. The form factors F_i^W of the W boson could, in principle, account for the structure of the W boson. However, for the process (5.1) they are needed in their static limit only:

$$F_1^W(0) = F_2^W(0) = 1. \quad (5.7)$$

Calculation of the Amplitude

Using these interactions, the amplitude corresponding to the Feynman diagrams in Fig. 5.1 is given by

$$\mathcal{M}_{fi} = -ige \cos \vartheta_C \epsilon_\mu(k, \lambda') M^{\mu\beta} \epsilon_\beta^W(Q, \lambda). \quad (5.8)$$

Here $\epsilon_\mu(k, \lambda')$ is the polarization vector of the initial photon and $\epsilon_\beta^W(Q, \lambda)$ is the polarization vector of the final W boson. The tensor $M^{\mu\beta}$ is given by the sum of the contributions of the individual diagrams

$$M^{\mu\beta} = M_{(a)}^{\mu\beta} + M_{(b)}^{\mu\beta} + M_{(c)}^{\mu\beta}. \quad (5.9)$$

The individual amplitudes are

$$M_{(a)}^{\mu\beta} = \frac{-1}{(Q-k)^2 - M_W^2} \bar{u}(p_2) [F_V(q^2)\gamma^\rho + F_A(q^2)\gamma^\rho\gamma_5 - iF_M(q^2)\sigma^{\rho\eta}q_\eta] u(p_1) \times \left(-g_{\alpha\rho} + \frac{q_\alpha q_\rho}{M_W^2} \right) [(q+Q)^\mu g^{\alpha\beta} - Q^\alpha g^{\mu\beta} - q^\beta g^{\mu\alpha}] + \kappa_W [k^\beta g^{\mu\alpha} - k^\alpha g^{\mu\beta}], \quad (5.10)$$

$$M_{(b)}^{\mu\beta} = \frac{1}{(p_1 - Q)^2 - M^2} \bar{u}(p_2) \left[F_1^n(k^2) \gamma^\mu + i \frac{\kappa_n}{2M} F_2^n(k^2) \sigma^{\mu\lambda} k_\lambda \right] (\not{p}_1 - \not{Q} + M) \times \left[F_V(Q^2) \gamma^\beta + F_A(Q^2) \gamma^\beta \gamma_5 - i F_M(Q^2) \sigma_{\beta\eta} Q^\eta \right] u(p_1), \quad (5.11)$$

and

$$M_{(c)}^{\mu\beta} = \frac{-1}{(p_1 + k)^2 - M^2} \bar{u}(p_2) \left[F_V(Q^2) \gamma^\beta + F_A(Q^2) \gamma^\beta \gamma_5 - i F_M(Q^2) \sigma^{\beta\eta} Q_\eta \right] \times (\not{p}_1 + \not{k} + M) \left[F_1^p(k^2) \gamma^\mu + i \frac{\kappa_p}{2M} F_2^p(k^2) \sigma^{\mu\lambda} k_\lambda \right] u(p_1). \quad (5.12)$$

Here M denotes the nucleon mass and we neglect the mass difference between neutrons and protons. p_1 is the momentum of the initial state proton, p_2 the momentum of the final state neutron, and Q denotes the momentum of the final state W boson.

Gauge Invariance

Gauge invariance requires that if the photon polarization vector ϵ_μ is formally replaced by the photon four momentum k_μ the matrix element must vanish. We test our matrix element for gauge invariance and see that the term $k_\mu M^{\mu\beta} \epsilon_\beta^W$ does not vanish.

$$k_\mu M^{\mu\beta} \epsilon_\beta^W = -F_1^W(0) \bar{u}(p_2) \left[F_V(q^2) \gamma^\beta + F_A(q^2) \gamma^\beta \gamma_5 - i F_M(q^2) \sigma^{\beta\eta} q_\eta \right] u(p_1) \epsilon_\beta^W + (F_1^p(0) - F_1^n(0)) \bar{u}(p_2) \left[F_V(Q^2) \gamma^\beta + F_A(Q^2) \gamma^\beta \gamma_5 - i F_M(Q^2) \sigma^{\beta\eta} Q_\eta \right] u(p_1) \epsilon_\beta^W \quad (5.13)$$

For structureless particles, where no weak form factors $F_{V|A|M}$ are needed and, especially, no magnetic term occurs, the sum of the three diagrams of Fig. 5.1 is gauge invariant. The extra term coming from diagram 5.1(b) vanishes, since $F_1^n = 0$ and the extra terms of diagrams 5.1(a) and 5.1(c) cancel each other. If we introduce weak form factors, the extra term of diagram 5.1(b) is still zero, but the two other diagrams do not cancel anymore, since their form factors are evaluated in momentum transfer regions far apart. The form factors of diagram 5.1(a) are evaluated in the spacelike region $q^2 < 0$, while the form factors of diagram 5.1(c) are evaluated far in the timelike region at $Q^2 = M_W^2$. Even if we assume that the weak form factors are constant over the whole region, which contradicts the conserved vector current hypothesis, there would remain a spare term proportional to the weak magnetic form factor F_M

$$-F_1^W(0) \bar{u}(p_2) (i F_M \sigma^{\beta\eta} k_\eta) u(p_1) \epsilon_\beta^W. \quad (5.14)$$

A similar problem occurs in pion electroproduction, where usually a term

$$\Delta M^\mu = \frac{-k^\mu}{k^2} k_\alpha M_\pi^\alpha \quad (5.15)$$

is added to make the matrix element gauge invariant. This choice is convenient since it does not contribute to the physical matrix element, because of $k^\mu \epsilon_\mu = 0$.

Berends and West [58] justify this term by using the appropriate half-off-shell vertices for the nucleons and pions. The equation of continuity $k_\mu J^\mu = 0$ for the electromagnetic current is only fulfilled if the vertex of equation (5.2) is taken between on-shell nucleon states. If one of the nucleons is off its mass-shell, a more general vertex, as introduced in [58, 59, 60], has to be used, for example

$$\Gamma_\mu^{\gamma NN} \propto \left[F_1^+ \gamma_\mu - i \frac{F_2^+}{2M} \sigma_{\mu\nu} k^\nu + F_3^+ k_\mu \right] (\not{p}_1 + \not{k} + M) + \left[F_1^- \gamma_\mu - i \frac{F_2^-}{2M} \sigma_{\mu\nu} k^\nu + F_3^- k_\mu \right] (-\not{p}_1 - \not{k} + M) \quad (5.16)$$

for an on-shell initial and an off-shell final nucleon. In this general case, the Ward-Takahashi identity [61] guarantees the conservation of charge and relates the form factors used in equation (5.16) to each other. Together with a more general vertex for the pion nucleon coupling, Berends and West [58] can explain the extra term (5.15) which is necessary to recover gauge invariance in pion electroproduction. However, this does not work in our case. For photoproduction of W bosons we have $k^2 = 0$ and a term proportional to $1/k^2$ as in equation (5.15) would lead to an extra term ΔM , which is much larger than the original matrix element. This would be a contradiction to our assumption that the diagrams of Fig. 5.1 are the relevant Feynman diagrams for the process (5.1). In pion electroproduction $k_\alpha M_\pi^\alpha$ vanishes for $k^2 = 0$ and therefore the singularity $1/k^2$ introduced in (5.15) does not affect the results.

Here, we follow the procedure of Fearing et al. [13] who introduce a general term $\Delta M^{\mu\beta}$ which is added to the matrix element $M^{\mu\beta}$ to preserve gauge invariance. This general term has to fulfill certain requirements:

- (i) ΔM should cancel the extra terms arising in $k_\mu M^{\mu\beta} \epsilon_\beta^W$,
- (ii) ΔM should not contain any new singularities in the physical region, and
- (iii) ΔM should satisfy $\Delta M \ll M$.

The term

$$\begin{aligned} \Delta M^{\mu\beta} = & \bar{u}(p_2) \left\{ -F_1^W(0) \left[F_V(q^2) \gamma^\beta + F_A(q^2) \gamma^\beta \gamma_5 - i F_M(q^2) \sigma^{\beta\eta} q_\eta \right] \right. \\ & \left. + (F_1^p(0) - F_1^n(0)) \left[F_V(Q^2) \gamma^\beta + F_A(Q^2) \gamma^\beta \gamma_5 - i F_M(Q^2) \sigma^{\beta\eta} Q_\eta \right] \right\} u(p_1) \\ & \times \frac{(-2Q + k)^\mu}{(Q - k)^2 - M_W^2} \end{aligned} \quad (5.17)$$

constructed according to the one introduced by Fearing et al. in [13] meets all three conditions. The gauge invariant amplitude is thus given by

$$\mathcal{M}_{fi} = -ig e \epsilon_\mu \underbrace{(M^{\mu\beta} + \Delta M^{\mu\beta})}_{M_{tot}^{\mu\beta}} \epsilon_\beta^W. \quad (5.18)$$

To obtain the total cross section, we average the squared amplitude over initial and sum over final state spins

$$\sum' |\mathcal{M}_{fi}|^2 = \frac{1}{4} g^2 (4\pi\alpha) (-g_{\mu\nu}) M_{tot}^{\mu\beta} \bar{M}_{tot}^{\nu\alpha} \left(-g_{\alpha\beta} + \frac{Q_\alpha Q_\beta}{M_W^2} \right) \quad (5.19)$$

and integrate over the phase space

$$\sigma_\gamma = \frac{1}{(2\pi)^2 2\lambda^{1/2}(s, M^2, M_W^2)} \int \frac{d^3 p_2}{2E_2} \frac{d^3 Q}{2Q_0} \sum' |\mathcal{M}_{fi}|^2 \delta^4(p_1 + k - p_2 - Q) \quad (5.20)$$

with

$$\lambda(x, y, z) = (x - y - z)^2 - 4yz. \quad (5.21)$$

The numerical integration over the phase space is done using the method of Byckling and Kajantie [15] for the generation of the phase space (see appendix C) and the Monte Carlo integration routine VEGAS [62, 63] (see appendix B).

Comparison with Fearing et al.

In order to test our results against those of Fearing et al., we have to make the following modifications: First, Fearing et al. computed their cross sections with a much lower W boson mass in mind. They give results for $M_W = 5$ GeV and $M_W = 10$ GeV. Second, they neglect the weak magnetic form factor F_M . This simplifies the discussion of gauge invariance. Next, they use $F_V = F_1^p$ instead of $F_V = F_1^p - F_1^n$. Finally, they use the same parameter $m_A^2 = m_V^2 = 0.71$ GeV² for the dipole fit for the vector and the axial vector weak form factor. In Fig. 5.3 we compare our results to the numeric values given in [14] for $M_W = 5$ GeV and $\kappa_W = -1, 0$, and 1 using dipole spacelike and timelike form factors and find them to be in good agreement.

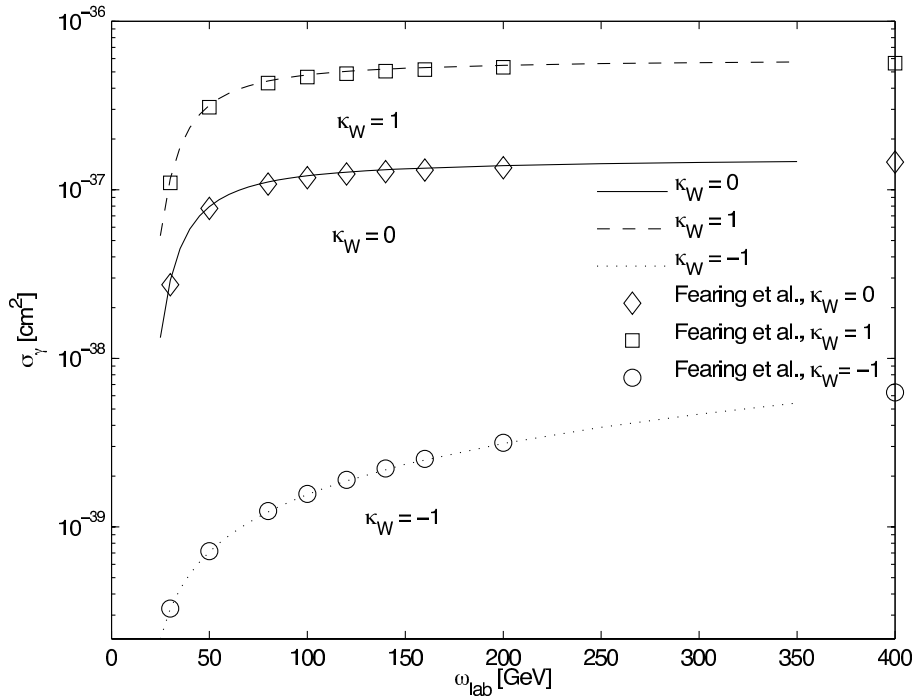


Figure 5.3: Total cross section for W photoproduction in cm^2 as function of the photon energy ω (lines) compared with the results of Fearing et al. [14] (symbols) with a W boson mass of $M_W = 5$ GeV and $\kappa_W = -1$ (dotted line and open circles), $\kappa_W = 0$ (solid line and open circles), and $\kappa_W = 1$ (dashed line and open squares).

Photoproduction Results

Having checked our results against those of Fearing et al. [14], we now proceed presenting the results for single W boson photoproduction using the correct W boson mass. First, we examine the effect of the aforementioned modifications on our results. For this purpose, we investigate how our results differ from those of Fearing et al. apart from the effect which is caused by using a larger W boson mass. In Fig. 5.4 we compare the total cross section for W photoproduction as function of the photon energy for the choice of form factors according to Fearing et al., the cross sections, when the modifications are switched on individually, and the cross section with our choice of form factors. In this way, we can estimate the effect of each modification on the cross section. Taking $F_V = F_1^p$ instead of $F_V = F_1^p - F_1^n$, as well as taking the same fit parameter $m_V^2 = m_A^2 = 0.71$ GeV² for the dipole form of the vector and the axial vector weak form factor, both change the cross section by around 20%. The inclusion of an additional weak form factor

F_M changes the cross section by around 30%. The overall difference between the cross sections with the form factor choice of Fearing et al. and our choice is $\sim 60 - 70\%$.

To illustrate the impact of the form factor choice on the total cross section, we present in Fig. 5.5

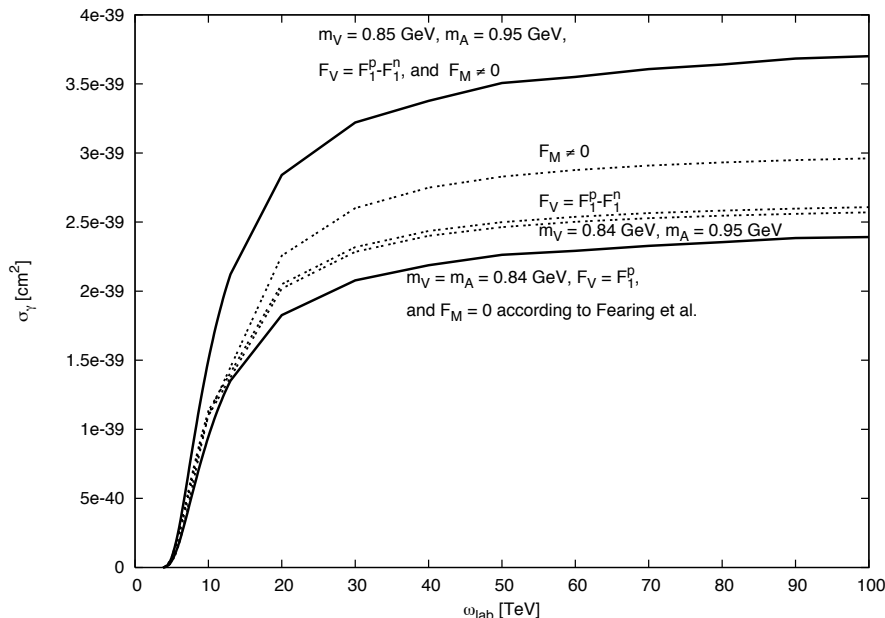


Figure 5.4: Total cross section for W photoproduction in cm^2 as function of the photon energy ω in the proton rest frame for the form factor choice of Fearing et al. (lower solid line), the cross sections when the modifications are switched on individually (dashed lines) and cross sections with our choice of form factors (upper solid line).

the total cross section as function of the photon energy for different choices of the form factor. The cross sections are almost the same for the cases where constant timelike form factors are employed and where no form factors are used at all. The cross section becomes much smaller when dipole weak timelike form factors are used. These observations can be understood by looking at the individual contributions of the diagrams of Fig. 5.1. The method Fearing et al. used to make the matrix element gauge invariant, allows to make the contribution to the matrix element of each diagram in Fig. 5.1 gauge invariant individually. Hence it is reasonable to plot the cross section of each diagram and the interference terms individually. In Figs 5.6(a) and 5.6(b) we present the individual contributions of the diagrams in Fig. 5.1 and the interference terms for constant and dipole weak timelike form factors for the Standard Model value $\kappa_W = 1$. For constant timelike form factors, the contributions of the nucleon pole diagrams (Figs 5.1(b) and 5.1(c)) dominate. Therefore the results do not differ from calculations where no form factors are used at all. Apart from that, the cross sections are not very sensitive to the anomalous magnetic moment of the W boson κ_W and thus to the $WW\gamma$ coupling. Including dipole form factors in the calculations affects the results in two ways: First, the cross sections are strongly suppressed by the restriction to small momentum transfers. Second, the W pole diagram (Fig. 5.1(a)) becomes the dominant contribution and thus the cross section is very sensitive to the form of the $WW\gamma$ coupling. Finally, in Fig. 5.7, we show the total cross section as function of the photon energy for dipole timelike form factors for various choices of the anomalous magnetic moment of the W boson: $\kappa_W = -1, 0, 1$. The most significant observation is that the cross section for $\kappa_W = -1$ is strongly suppressed as compared to the cross section for other choices of κ_W . This is due to the fact that the matrix element for the contribution of diagram 5.1(a) is approximately proportional to $(\kappa_W + 1)$. Hence in the case $\kappa_W = -1$, diagrams 5.1(b) and 5.1(c) become dominant again.

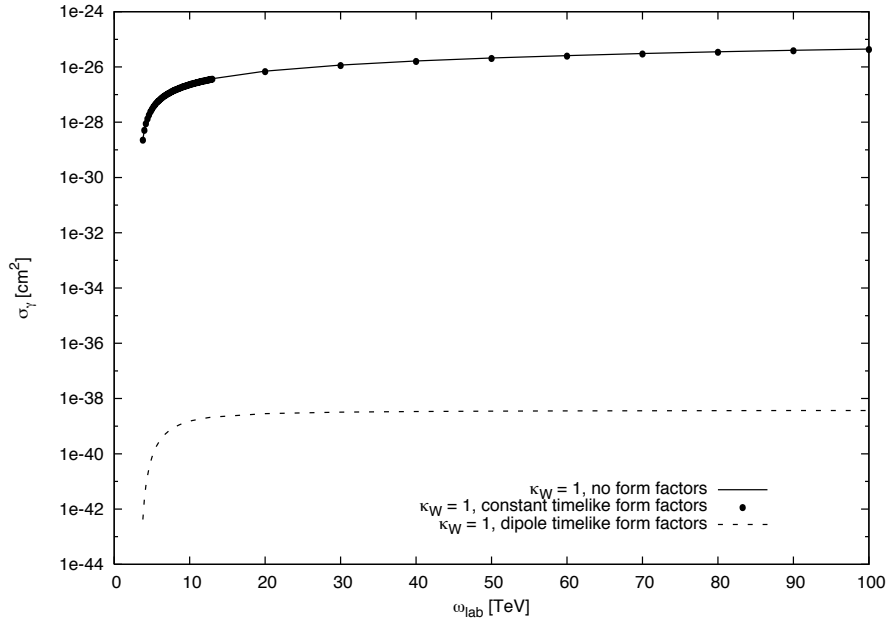


Figure 5.5: Total cross section for W photoproduction in cm^2 as function of the photon energy ω in the proton rest frame with no form factors (solid line), constant timelike form factors (points) and dipole timelike form factors (dashed line).

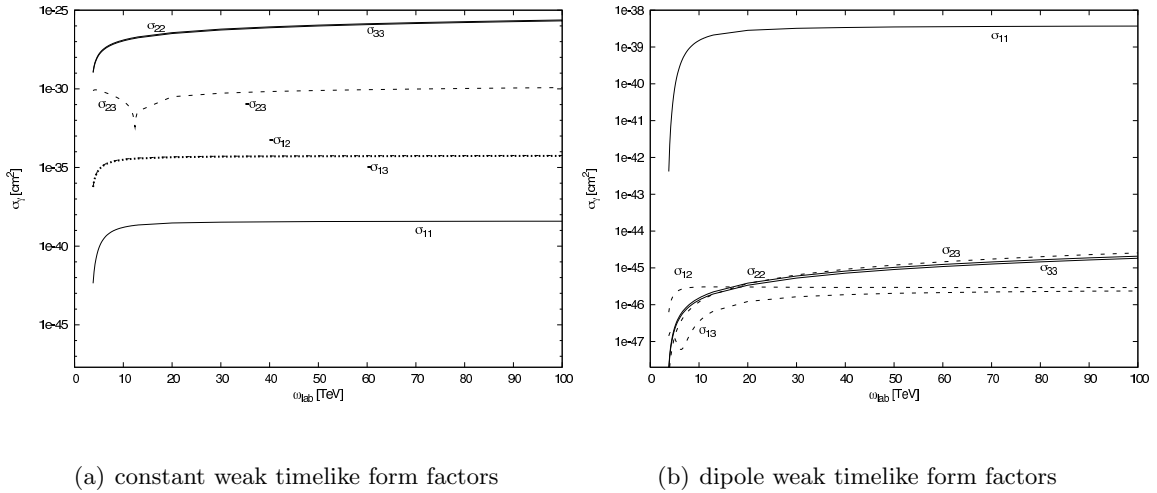


Figure 5.6: Total cross section for W photoproduction in cm^2 as function of the photon energy ω in the proton rest frame plotted for each diagram of Fig. 5.1 (solid lines) and the interference terms (dashed lines) individually for constant and dipole weak timelike form factors and the Standard Model value $\kappa_W = 1$.

5.3 W Boson Production in p-p and p-A Collisions

In order to obtain predictions for cross sections in collider experiments, for example for proton-proton (p-p) and proton-ion (p-A) collisions at the LHC, we have to convolve the photoproduction cross sections σ_γ derived in the previous section with the equivalent photon spectrum of protons

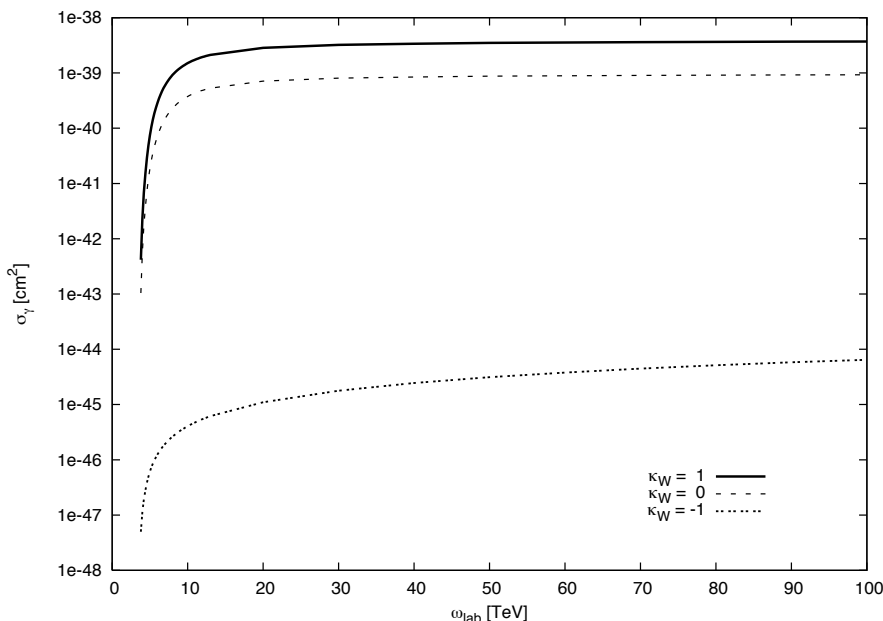


Figure 5.7: Total cross section for W photoproduction in cm^2 as function of the photon energy ω in the proton rest frame with dipole timelike form factors for different choices of the anomalous magnetic moment κ_W of the W boson: $\kappa_W = 1$ (solid line), $\kappa_W = 0$ (dashed line), and $\kappa_W = -1$ (dotted line)

or ions as introduced in chapter 3

$$\sigma = \int dz f_{\gamma|p/A}(z) \sigma_\gamma. \quad (5.22)$$

The photoproduction cross section σ_γ is evaluated at photon energies $\omega = z \cdot E_{p/A}$ and the integration over all possible photon energies is carried out.

Single W production from elastic photon emission in p-Pb collisions

For the calculation of the cross section of exclusive single W production in p-Pb collisions at the LHC, the photoproduction cross section is convolved with the equivalent spectrum for elastic photon emission by a nucleus as introduced in section 3.3.1

$$f_{\gamma|A}(z) = \frac{2Z^2\alpha}{\pi} \frac{1}{z} \log\left(\frac{1}{zM_AR}\right) \quad (5.23)$$

with charge number $Z = 82$, mass number $A = 208$, and radius $R = 1.2\text{fm}A^{1/3} \approx 7\text{fm}$ for lead. This yields an approximate total cross section for exclusive single W production in p-Pb collisions of $\sim 9 \cdot 10^{-37}\text{cm}^2$. This cross section corresponds to at least ~ 0.2 events per month assuming a minimum achievable luminosity of $\mathcal{L}_{\text{p-Pb}} \approx 10^{29}\text{cm}^{-2}\text{s}^{-1}$ [64]. Experiments in the p-Pb mode will run for only around a month. Therefore, measuring single W production in this mode will only be feasible if the luminosities exceed the minimum value given above by several orders of magnitude or if the measurement time is extended significantly. In Fig. 5.8 we display the total cross section of single W production in p-Pb collisions as a function of the anomalous magnetic moment κ_W of the W boson. This demonstrates the sensitivity of the total cross section to κ_W and, thus, to the triple gauge boson coupling. In Fig. 5.9 we present the differential cross section as function of the energy of the W boson and the neutron for the Standard Model value $\kappa_W = 1$.

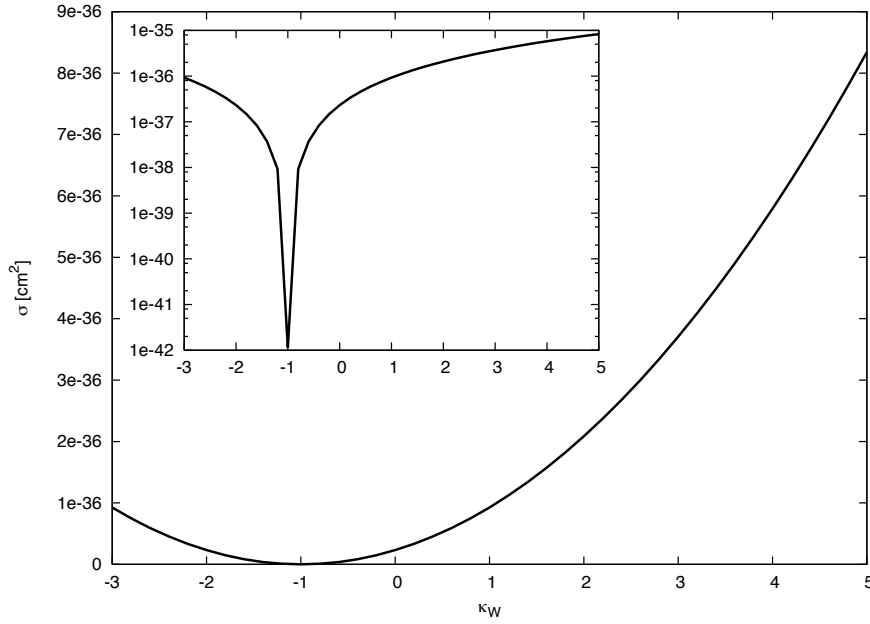


Figure 5.8: Total cross section for W production in cm^2 in proton lead collisions at the LHC as function of the anomalous magnetic moment κ_W of the W boson on a logarithmic and a linear scale.

The W boson is produced almost at rest and the neutron obtains about the energy of the initial proton ($E_p = 7$ TeV). Fig. 5.10 shows the differential cross section of single W production as function of the rapidity of the W boson and the neutron at $\kappa_W = 1$. For comparison, the initial proton has rapidity $Y_p = -9.5$ and the initial lead ion has rapidity $Y_{Pb} = 8.6$.

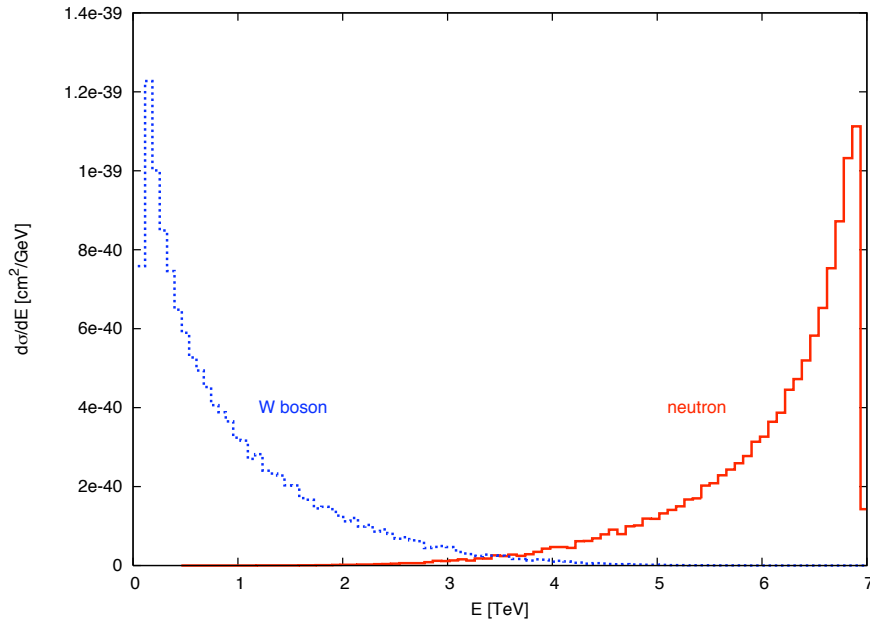


Figure 5.9: Differential cross section for W production in cm^2/GeV in p-Pb collisions at the LHC as function of the energy of the W boson and the neutron for $\kappa_W = 1$.

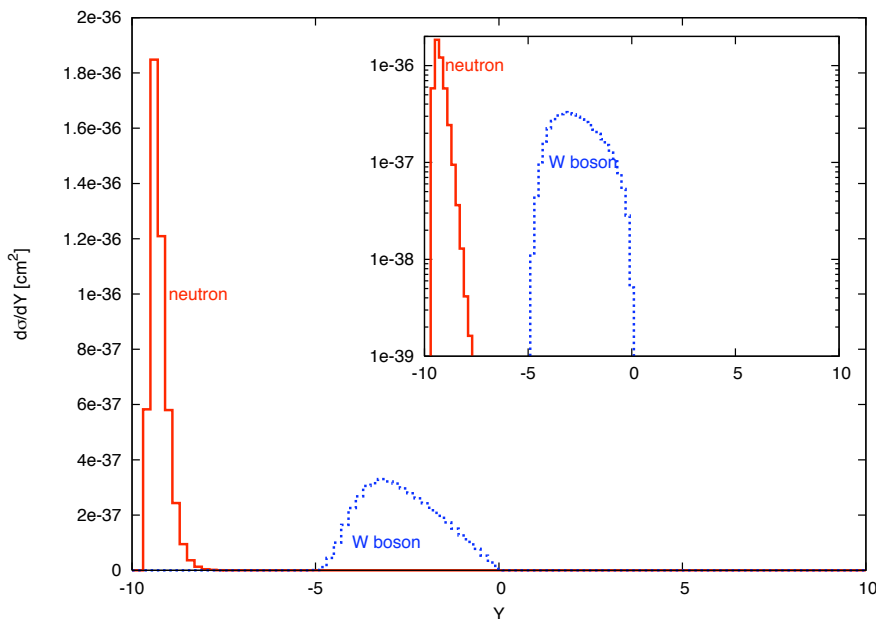


Figure 5.10: Differential cross section for W production in cm^2 in p-Pb collisions at the LHC as function of the rapidity of the W boson and the neutron for $\kappa_W = 1$ on a logarithmic and a linear scale.

Single W production from elastic photon emission in p-p collisions

As already explained in chapter 3 several possibilities exist for protons: elastic and several types of inelastic photon emission. Considering elastic photon emission only, the appropriate photon spectrum is the one derived by Kniehl [50]. Convoluting the photoproduction cross section σ_γ with this photon spectrum yields a total cross section of $\sim 5 \cdot 10^{-40} \text{ cm}^2$ for exclusive single W production. The luminosity for p-p collisions at the LHC is expected to be between $\mathcal{L}_{pp} \approx 10^{29} \text{ cm}^{-2}\text{s}^{-1}$ and $\mathcal{L}_{pp} \approx 10^{34} \text{ cm}^{-2}\text{s}^{-1}$, which gives between $\sim 1.5 \cdot 10^{-3}$ and ~ 150 events per year. Consequently, exclusive single W production is only observable in the high luminosity runs, where event identification becomes difficult due to pile-up events, as one single bunch may produce several events. Therefore, a clean and unique event signature is essential.

Fig. 5.11 shows the differential cross section as function of the energy of the neutron, the W boson and the proton which emitted the photon, for the Standard Model value $\kappa_W = 1$. The proton which emitted the elastic photon, emerges at almost its initial energy $E_p = 7 \text{ TeV}$. In Fig. 5.12 we present the differential cross section as function of the rapidity of all the final particles: the neutron, the W boson, and the photon parent proton, again for the value $\kappa_W = 1$. The rapidities of the initial protons are $Y_p = \pm 9.5$.

Single W production from deep inelastic photon emission in p-p collisions

For large momentum transfers $Q_k^2 = |k^2|$ of the photon, the proton acts as a collection of partons, rather than one single particle. These partons then radiate like point-like particles. This is described by a two-step convolution

$$\sigma = \int dx \int du \sum_{q_i} e_i^2 f_{q_i|p}(x, \langle Q_k^2 \rangle) f_{\gamma|q_i}(u) \sigma_\gamma \quad (5.24)$$

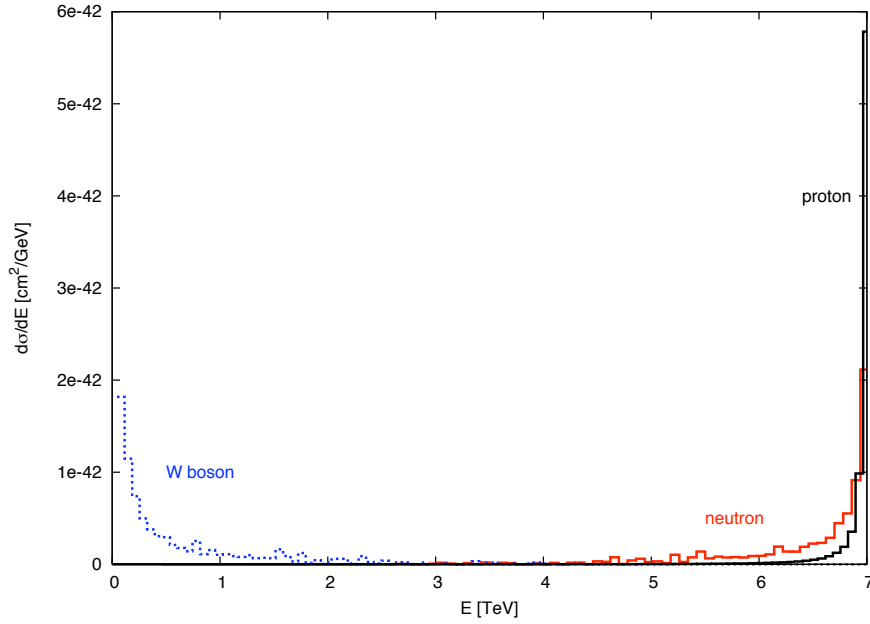


Figure 5.11: Differential cross section for W production in cm^2/GeV in p-p collisions at the LHC as function of the energy of the W boson, the neutron, and the proton which emitted the elastic photon, for $\kappa_W = 1$.

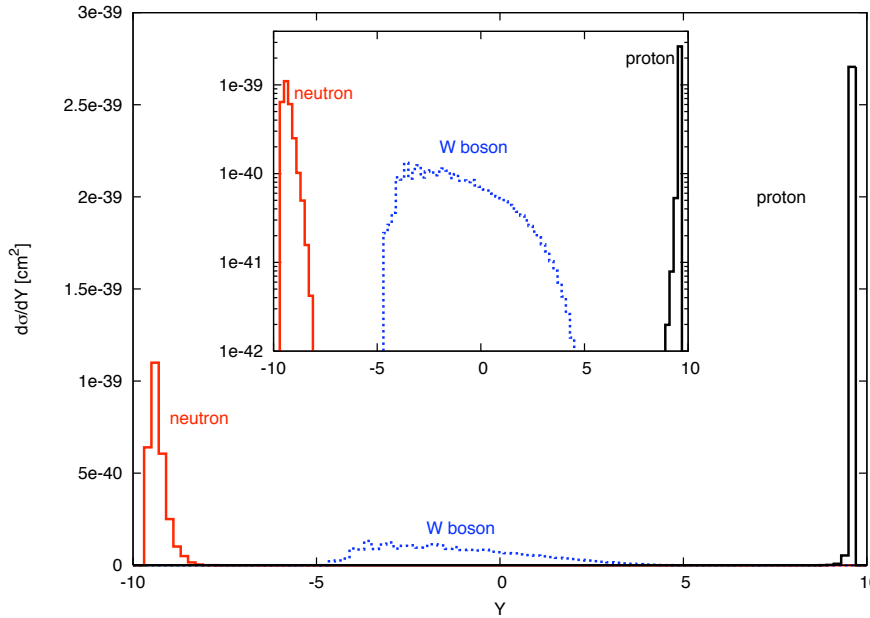


Figure 5.12: Differential cross section for W production in cm^2 in p-p collisions at the LHC as function of the rapidity of the W boson, the neutron, and the proton which emitted the elastic photon, for $\kappa_W = 1$ on a logarithmic and a linear scale.

with the equivalent photon spectrum of quarks

$$f_{\gamma|q}(u) = \frac{\alpha}{2\pi} \frac{1 + (1-u)^2}{u} \log\left(\frac{Q_{max}^2}{Q_{min}^2}\right) \quad (5.25)$$

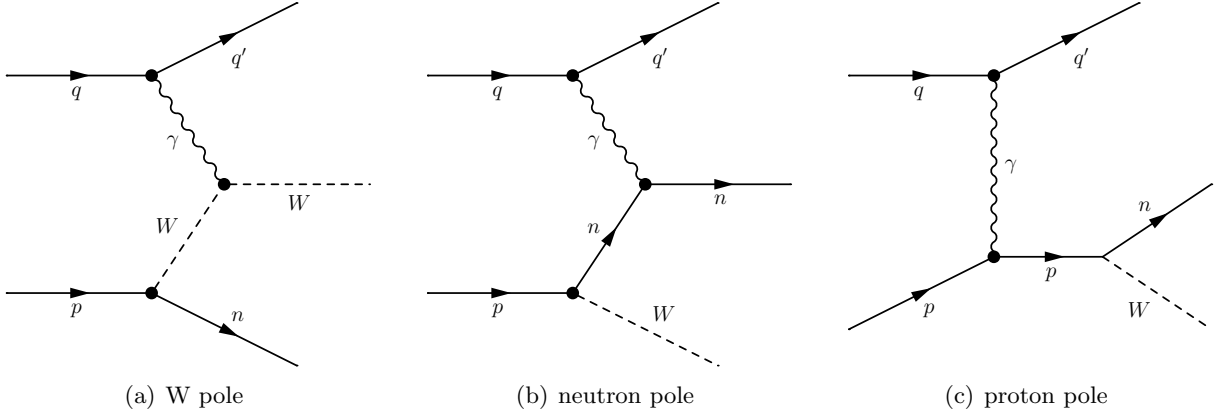


Figure 5.13: Feynman diagrams corresponding to those of Fig. 5.1 for single W boson production, where the photon is emitted by a quark inside the proton.

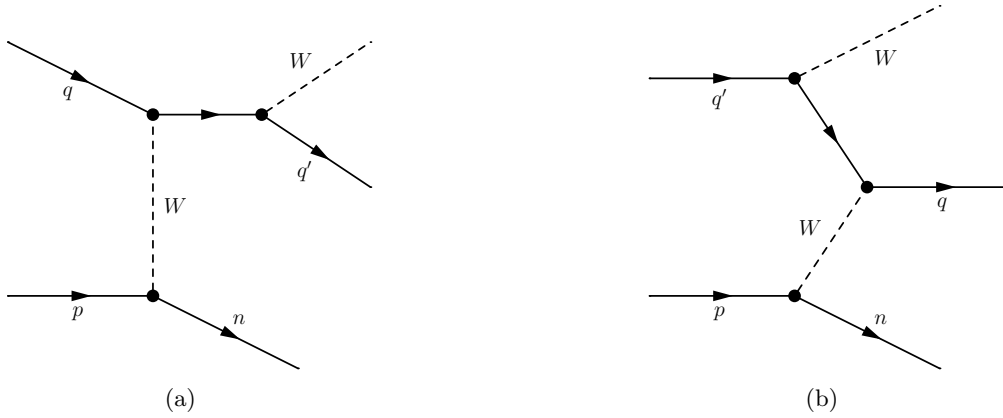


Figure 5.14: Two additional Feynman diagrams, which contribute to single W boson production from quarks.

as described in section 3.4.1. For Q_{min} we choose a value of 1 GeV, which guarantees the quark parton model to be applicable. As upper limit Q_{max} we take the W boson mass M_W .

Fig. 5.13 shows the diagrams, which correspond to those of Fig. 5.1, but instead of being real, the photon is emitted by a quark. In section 5.2 we found that for real photons the contributions of the neutron pole (Fig. 5.1(b)) and the proton pole (Fig. 5.1(c)) diagrams are suppressed when dipole timelike form factors are used. These two diagrams (Figs 5.13(b) and 5.13(c)) are even more suppressed for larger momentum transfers of the photon $Q_k^2 = |k^2| \gg 0$ due to the electromagnetic form factors, which fall off with increasing Q_k^2 . Anyhow, we would expect to have a deep inelastic process at both ends of the photon line. Thus, for exclusive W production, where we require the neutron to be detected, the nucleon pole diagrams (Figs 5.1(b) and 5.1(c)) can safely be neglected. Instead, two new diagrams may contribute. These are depicted in Fig. 5.14. However, due to the large mass of the weak gauge bosons, the range of the weak interaction is limited to $\sim 10^{-18}$ m, which is too short for the W boson to leave the proton. Thus, diagrams of the type as those depicted in Fig. 5.13 do not contribute in our case, where we are interested in peripheral collisions only. Consequently, we consider only the diagram of Fig. 5.13(a) in our prediction for the cross section of single W production from a deep inelastically emitted photon. Using the definition of Pisano [51]

$$\langle Q_k^2 \rangle = \frac{Q_{max}^2 - Q_{min}^2}{\log Q_{max}^2 - \log Q_{min}^2} \quad (5.26)$$

as an average momentum transfer in the parton distribution functions, we obtain a value of $\sim 1.7 \cdot 10^{-39} \text{cm}^2$, which is approximately a factor 3 larger than the cross section for elastic photon emission by a proton. However, the size of the total cross section from deep inelastic photon emission depends on the choice of the upper limit Q_{max}^2 of the integration. This makes the deep inelastic photon spectrum less suitable for reliable estimates. In Fig. 5.15 we demonstrate how the total cross section varies as function of the choice of $Q_{av} = \sqrt{\langle Q_k^2 \rangle}$ for values between $Q_{min} = 1 \text{ GeV}$ and $Q_{max} = M_W$. This tests how sensitive our calculation is to the approximation that the PDFs are evaluated at a fixed value of momentum transfer. Since the variation is not too large - the values lie between $1.2 \cdot 10^{-39} \text{cm}^2$ and $1.9 \cdot 10^{-39} \text{cm}^2$ - this approximation is good enough for our purpose.

In Figs. 5.16 and 5.17 we present the differential cross section as function of the energy and

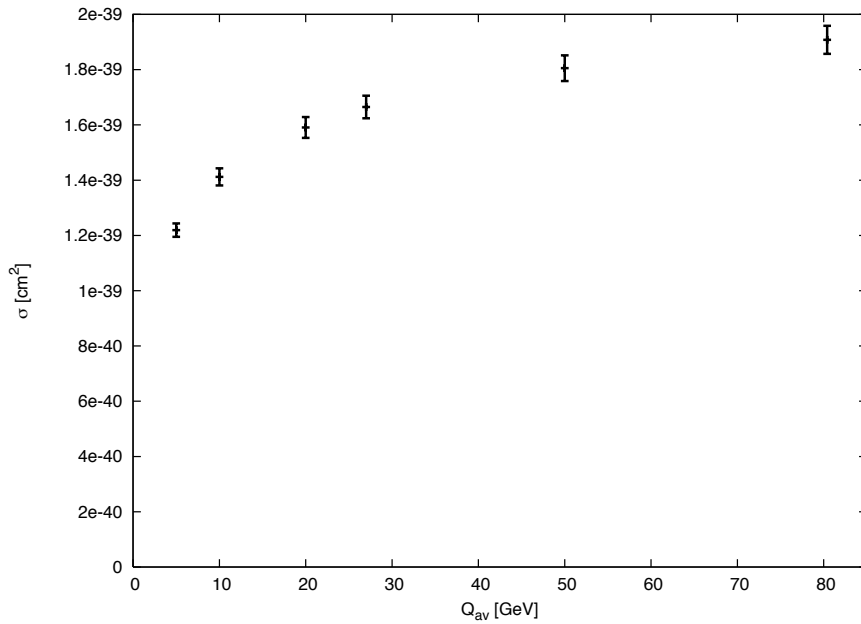


Figure 5.15: Total cross section for W production from deep inelastic photon emission from protons as function of the momentum transfer Q_{av} , at which the quark distribution functions are evaluated.

rapidity of the neutron and the W boson. Apart from the height of the distributions, they do not differ from those for elastic photon emission, since they depend only on the subprocess $\gamma + p \rightarrow n + W$, which is calculated assuming a real photon in both calculations. The main difference between the two is that in the deep inelastic case the proton which emits the photon breaks up and thus is not detected as one particle in the final state, but as a parton jet.

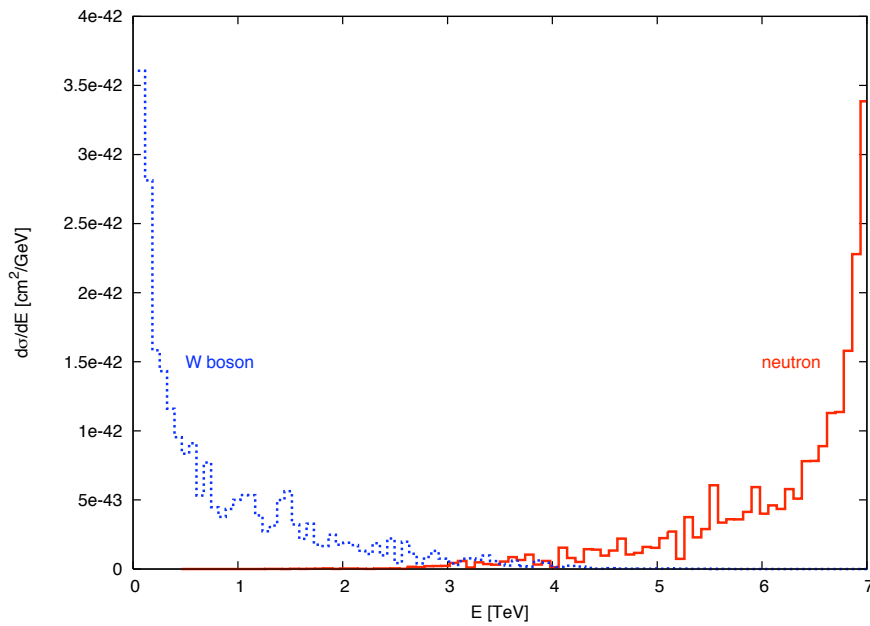


Figure 5.16: Differential cross section for W production in cm^2/GeV in p-p collisions at the LHC as function of the energy of the W boson and the neutron for deep inelastic photon emission by the proton for $\kappa_W = 1$.

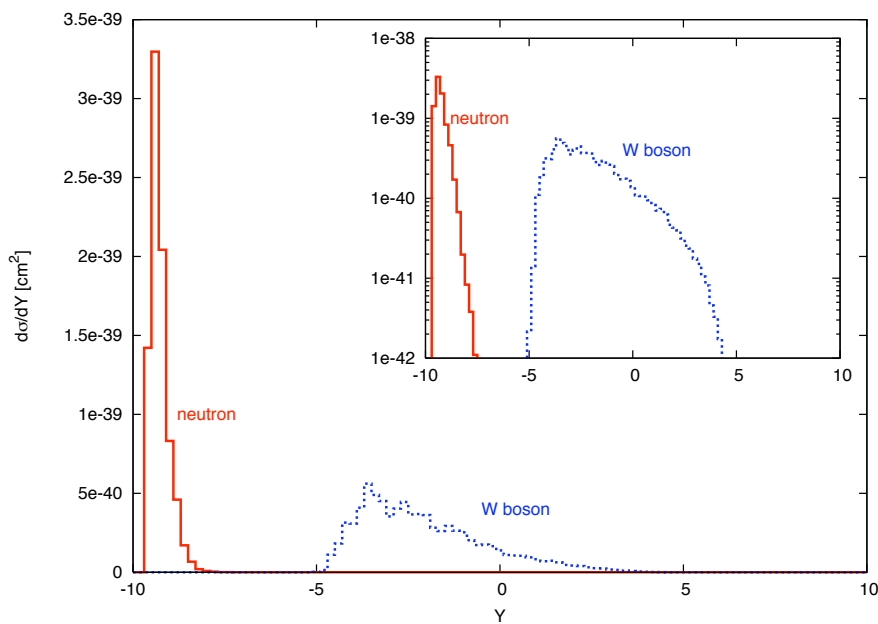


Figure 5.17: Differential cross section for W production in cm^2 in p-p collisions at the LHC as function of the rapidity of the W boson and the neutron for deep inelastic photon emission by the proton for $\kappa_W = 1$ on a logarithmic and a linear scale.

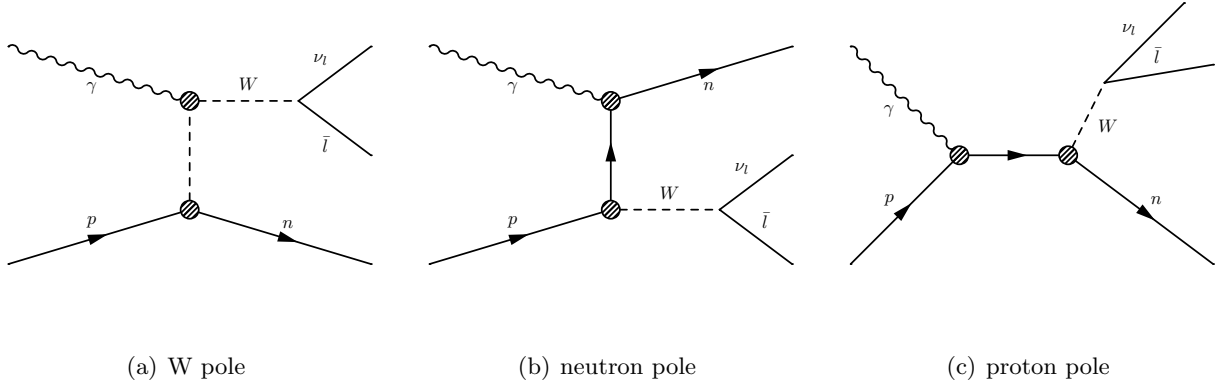


Figure 5.18: Feynman diagrams corresponding to those of 5.1 for single W boson photoproduction including also the decay of the W boson.

5.4 Decay of W Bosons

The W boson cannot be detected as a free particle, since it decays almost immediately (after $\sim 10^{-25}s$). Hence, the properties of W bosons must be measured through their decay products. Experimentally, the W bosons are best measured through their decay to a charged lepton and a neutrino. Approximately 22% of the W^+ bosons decay into a positron or an anti-muon and the corresponding neutrino. The amplitude of single W photoproduction including also the decay into an anti-lepton and a neutrino reads (see Fig. 5.18):

$$\mathcal{M}_{fi} \propto \epsilon_\mu(k, \lambda') M^{\mu\beta} \frac{(-g_{\beta\delta} + \frac{Q_\beta Q_\delta}{M_W^2})}{Q^2 - M_W^2} \bar{u}(p_4) \gamma^\delta (1 - \gamma_5) v(p_3), \quad (5.27)$$

with $M^{\mu\beta}$ as defined by equations (5.9) - (5.12). Here p_3 denotes the momentum of the anti-lepton and p_4 the momentum of the neutrino. Including the decay of the W boson complicates the discussion of gauge invariance even more, since now both W bosons in diagram 5.18(a) may be off their mass-shells. To overcome this difficulty and to simplify the calculation, we restrict ourselves to the production of an on-shell W boson and its subsequent decay into an anti-lepton and a neutrino, for details see [65]. The W boson propagator in (5.27) can be rewritten as

$$\frac{-g_{\beta\delta} + \frac{Q_\beta Q_\delta}{M_W^2}}{Q^2 - M_W^2} = \sum_\lambda \frac{\epsilon_\beta^W(\lambda) \epsilon_\delta^W(\lambda)}{Q^2 - M_W^2}. \quad (5.28)$$

This propagator gives rise to a pole when the W boson is treated as a stable particle on its mass-shell. This can be cured by introducing a finite decay width for gauge bosons and the denominator of the propagator $Q^2 - M_W^2$ is replaced by $Q^2 - M_W^2 + i\Gamma_W M_W$. The amplitude (5.27) can now be written as

$$\begin{aligned} \mathcal{M}_{fi} &\propto \sum_\lambda \epsilon_\mu(k, \lambda') M^{\mu\beta} \frac{\epsilon_\beta^W \epsilon_\delta^W}{Q^2 - M_W^2 + i\Gamma_W M_W} \bar{u}(p_4) \gamma^\delta (1 - \gamma_5) v(p_3) \\ &\propto \underbrace{\sum_\lambda \epsilon_\mu(k, \lambda') M^{\mu\beta} \epsilon_\beta^W(\lambda)}_{\propto \mathcal{M}_{Wprod}} \frac{1}{Q^2 - M_W^2 + i\Gamma_W M_W} \underbrace{\epsilon_\delta^W(\lambda) \bar{u}(p_4) \gamma^\delta (1 - \gamma_5) v(p_3)}_{\propto \mathcal{M}_{decay}} \end{aligned} \quad (5.29)$$

The total cross section for this process is given by

$$\sigma = \frac{1}{F} \int \frac{d^3 p_2}{2E_2 (2\pi)^3} \frac{d^3 p_3}{2E_3 (2\pi)^3} \frac{d^3 p_4}{2E_4 (2\pi)^3} (2\pi)^4 \delta^4(p_1 + k - p_2 - p_3 - p_4) \sum |\mathcal{M}_{fi}|^2 \quad (5.30)$$

Inserting the unity

$$1 = \int d^4Q \delta^4(Q - p_3 - p_4) \quad (5.31)$$

and rewriting the integration over dQ_0 as

$$dQ_0 = \frac{1}{2Q_0} dQ^2 \quad (5.32)$$

equation (5.30) can be cast into the form

$$\begin{aligned} \sigma = & \sum_{\lambda} \frac{1}{F} \int \frac{d^3p_2}{(2\pi)^3 2E_2} \frac{d^3Q}{(2\pi)^3 2Q_0} \underbrace{\sum' |\mathcal{M}_{Wprod}|^2 (2\pi)^4 \delta^4(k + p_1 - Q - p_2)}_{\sigma_{Wprod}^{\lambda}} \underbrace{\frac{dQ^2}{(2\pi)} \frac{1}{(Q^2 - M_W^2 + i\Gamma_W M_W)^2}}_{(\star)} \\ & \times \underbrace{\int \frac{d^3p_3}{(2\pi)^3 2E_3} \frac{d^3p_4}{(2\pi)^3 2E_4} \sum' |\mathcal{M}_{decay}|^2 (2\pi)^4 \delta^4(Q - p_3 - p_4)}_{2M_W \Gamma_W^{\lambda}} \end{aligned} \quad (5.33)$$

where \sum' stands for averaging over initial and summing over final particle spins. σ_{Wprod}^{λ} is the total cross section for the production of an on-shell single W boson with a given polarization λ , Γ_{decay}^{λ} is the decay width of an on-shell W boson with a given polarization λ into an anti-lepton and a neutrino. Next, the integration over dQ^2 can be carried out and the expression (\star) can be evaluated yielding

$$\frac{1}{2\pi} \int_{-\infty}^{\infty} dQ^2 \frac{1}{(Q^2 - M_W^2 + i\Gamma_W M_W)^2} = \frac{1}{2\Gamma_W M_W}. \quad (5.34)$$

Thus, the cross section of the complete process is given by the product

$$\sigma = \sum_{\lambda} \sigma_{Wprod}^{\lambda} \frac{1}{\Gamma_W} \Gamma_{decay}^{\lambda} \quad (5.35)$$

with $\Gamma_W = 2.0817\text{GeV}$. This product, however, has to be calculated for each polarization of the W boson independently and the summation can only be carried out afterwards. Therefore, we have to calculate the cross section for W production for each polarization vector of the W boson individually. For a W boson with four momentum

$$Q = (Q_0, 0, 0, |\vec{Q}|), \quad (5.36)$$

where the spatial momentum points into the z -direction, a set of polarization vectors is given by

$$\epsilon_L = \frac{1}{M_W} (|\vec{Q}|, 0, 0, Q_0) \quad (5.37)$$

$$\epsilon_1 = (0, 1, 0, 0) \quad (5.38)$$

$$\epsilon_2 = (0, 0, 1, 0). \quad (5.39)$$

ϵ_L is the longitudinal polarization, $\epsilon_{1,2}$ are the transverse polarizations. First, we rotate these polarization vectors into a system, where the spatial momentum of the W boson points into an arbitrary direction

$$Q = (Q_0, Q_x, Q_y, Q_z). \quad (5.40)$$

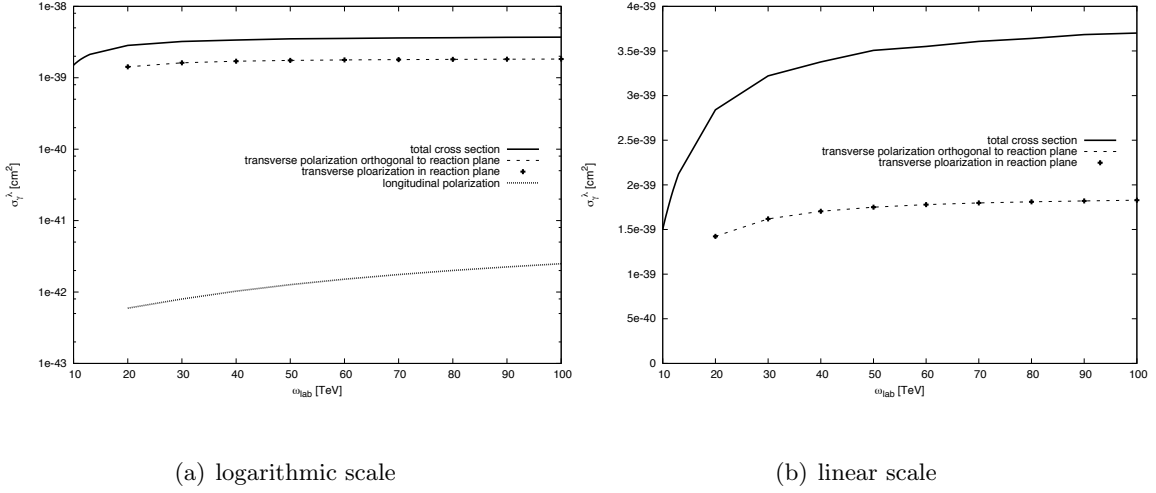


Figure 5.19: Comparison between the total cross section for the photoproduction of single W bosons and the cross sections for each polarization of the W boson individually as function of the photon energy ω_{lab} in the proton rest frame. The total cross section is the sum over the individual contributions of all polarizations. The cross sections are given for the Standard Model value $\kappa_W = 1$.

The polarization vectors in this system are

$$\epsilon_L = \frac{1}{M_W} (|\vec{Q}|, \frac{Q_0}{|\vec{Q}} \vec{Q}) \quad (5.41)$$

$$\epsilon_1 = \frac{1}{|\vec{Q}| \sin \Theta} (0, -Q_y, Q_x, 0) \quad (5.42)$$

$$\epsilon_2 = \frac{1}{|\vec{Q}|^2 \sin \Theta} (0, -Q_x \cdot Q_z, -Q_y \cdot Q_z, |\vec{Q}|^2 \sin^2 \Theta) \quad (5.43)$$

with Θ being the angle between the spatial directions of the photon and the W boson. Next, we insert them into our cross section calculation. The total cross section as calculated in the previous sections, should be reproduced as the sum over the contributions of all three polarizations. The contribution of the longitudinal polarization to the cross section turns out to be negligible as compared to the contributions of the transverse polarizations. The contributions of the transverse polarizations are equal and amount half of the total cross section each. This can be seen in Fig. 5.19 for the photoproduction cross section of single W bosons at various photon energies. This persists even if we rotate the transverse polarizations about the \vec{Q} -axis by an arbitrary angle. We calculate the decay of the W^+ in its rest-frame with the longitudinal polarization pointing into the z-direction.

$$\begin{aligned} \Gamma^\lambda(W^+(Q, \lambda) \rightarrow l^+(p_3) + \nu_l(p_4)) &= \frac{1}{2M_W} \frac{e^2}{2 \sin^2 \Theta_W} \int |\mathcal{M}_\lambda|^2 \\ &\times (2\pi)^4 \delta^4(Q - p_3 - p_4) \frac{d^3 p_3}{2E_3 (2\pi)^3} \frac{d^3 p_4}{2E_4 (2\pi)^3}, \end{aligned} \quad (5.44)$$

which can be rewritten in the form

$$\Gamma^\lambda(W^+(Q, \lambda) \rightarrow l^+(p_3) + \nu_l(p_4)) = \frac{1}{2M_W} \frac{e^2}{2 \sin^2 \Theta_W} \frac{1}{8(2\pi)^2} \int d\Omega_l |\mathcal{M}_\lambda|^2 \quad (5.45)$$

according to Byckling and Kajantie [15], see appendix C. The amplitude for the decay of a polarized W^+ boson is given by

$$\mathcal{M}_\lambda = \epsilon_\lambda^\mu \bar{u}(p_4) \gamma_\mu \frac{1 - \gamma_5}{2} v(p_3) \quad (5.46)$$

squaring and summing over the lepton spins yields

$$|\mathcal{M}_\lambda|^2 = \frac{1}{4} \text{Tr} [\not{p}_4 \not{\epsilon}_\lambda (1 - \gamma_5) \not{p}_3 (1 + \gamma_5) \not{\epsilon}_\lambda] \quad (5.47)$$

$$= 4(p_3 \cdot \epsilon_\lambda)(p_4 \cdot \epsilon_\lambda) + 2(p_3 \cdot p_4). \quad (5.48)$$

The W boson decays into an anti-lepton and a neutrino with four momenta

$$p_3 = \left(\frac{M_W}{2}, \frac{M_W}{2} \sin \Theta_l \cos \varphi_l, \frac{M_W}{2} \sin \Theta_l \sin \varphi_l, \frac{M_W}{2} \cos \Theta_l \right) \quad (5.49)$$

$$p_4 = \left(\frac{M_W}{2}, -\frac{M_W}{2} \sin \Theta_l \cos \varphi_l, -\frac{M_W}{2} \sin \Theta_l \sin \varphi_l, -\frac{M_W}{2} \cos \Theta_l \right), \quad (5.50)$$

where we neglect the lepton mass. Θ_l and φ_l denote the angles of the decay products in the rest frame of the W boson with respect to the z-direction. Employing these four vectors the decay widths for the transverse polarizations are given by

$$\Gamma_{decay}^1 = \frac{\alpha M_W}{32\pi \sin^2 \Theta_W} \int d\Omega_l (1 - \sin^2 \Theta_l \cos^2 \varphi_l) \quad (5.51)$$

and

$$\Gamma_{decay}^2 = \frac{\alpha M_W}{32\pi \sin^2 \Theta_W} \int d\Omega_l (1 - \sin^2 \Theta_l \sin^2 \varphi_l). \quad (5.52)$$

The weak mixing angle Θ_W is fixed by the ratio $\cos^2 \Theta_W = 1 - \sin^2 \Theta_W = \frac{M_W^2}{M_Z^2}$. However, since both transverse polarizations make up half of the total W production cross section each

$$\sigma_{Wprod}^1 = \sigma_{Wprod}^2 = \frac{1}{2} \sigma_{Wprod}, \quad (5.53)$$

we can finally rewrite the total cross section including the decay as

$$\sigma = \frac{1}{\Gamma_W} \sigma_{Wprod} \Gamma_{decay} \quad (5.54)$$

with

$$\Gamma_{decay} = \frac{1}{32} \frac{\alpha}{\sin^2 \Theta_W} M_W \int (1 + \cos^2 \Theta_l) \sin \Theta_l d\Theta_l = \frac{\alpha M_W}{12 \sin^2 \Theta_W}. \quad (5.55)$$

We still have to boost and rotate the four momenta p_3 and p_4 from the rest system of the W boson into the collider frame to obtain the differential distributions of the anti-lepton and the neutrino. In Figs 5.20 and 5.21 we show the differential cross section as function of the energies and the rapidities of the produced anti-lepton and neutrino. The differential cross sections as function of the rapidities of the decay products can be seen in the context of the rapidities of the other final particles and of the intermediate W boson in Fig. 5.22. In order to reconstruct the properties of the W boson, the transverse momenta of its decay products have to be known as well. In Fig. 5.23 we present the differential cross section as function of the transverse momentum of the anti-lepton and the neutrino. The decay products are produced with about equal transverse momenta. Thus, the transverse momentum of the neutrino, which cannot be measured in the experiment, can easily be reconstructed from the transverse momentum of the anti-lepton.

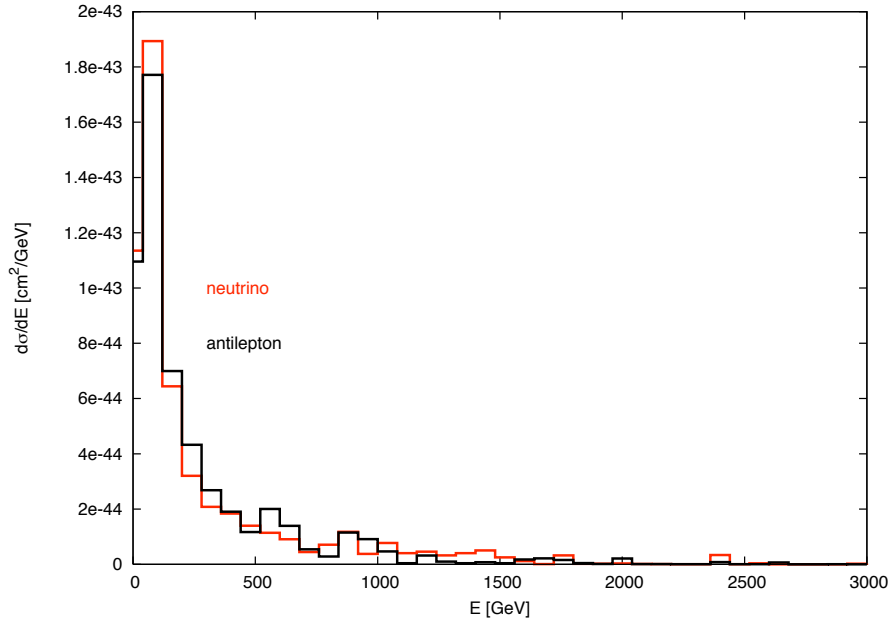


Figure 5.20: Differential cross section as function of the energy of the leptonic decay products of the W for $\kappa_W = 1$ in p-p collisions at LHC.

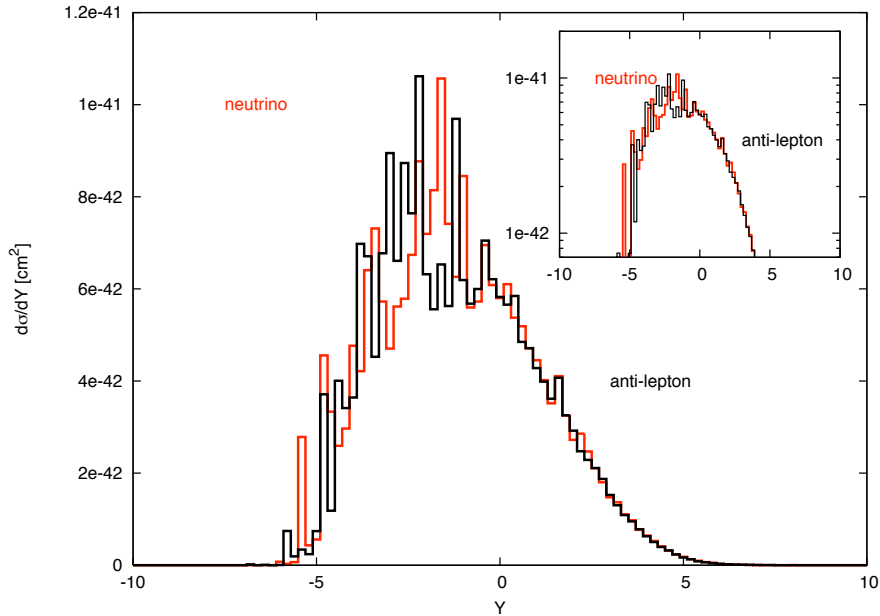


Figure 5.21: Differential cross section as function of the rapidity of the leptonic decay products of the W for $\kappa_W = 1$ in p-p collisions at LHC on a logarithmic and a linear scale.

We have to bear in mind, however, that the diagrams of Fig. 5.24 have the same initial and final particles as the diagrams in Fig. 5.18 and thus have to be taken into account as background to the process under consideration. A contribution of the diagrams of Figs 5.24(a) and 5.24(b) is ruled out in UPCs again due to the short range of the weak interaction. Therefore we only have

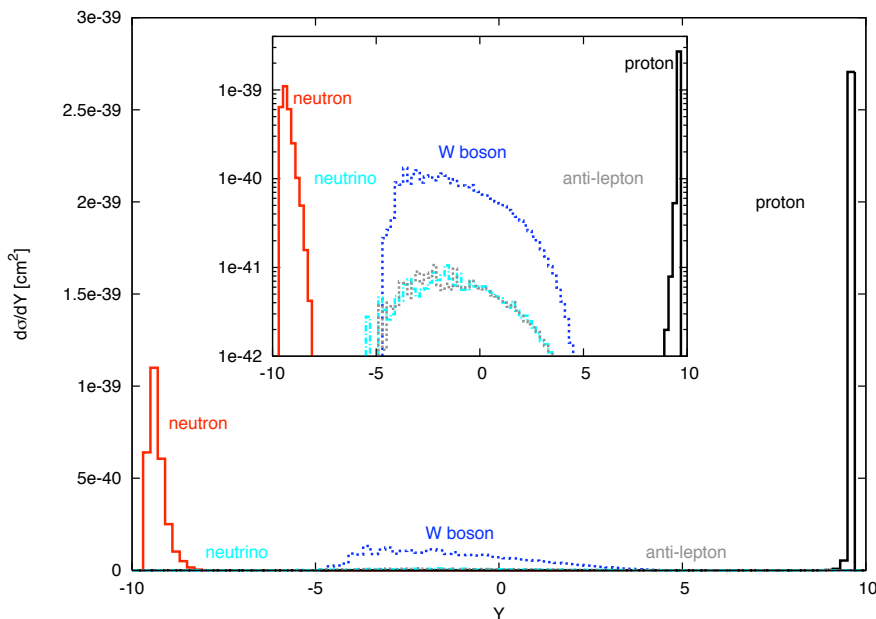


Figure 5.22: Differential cross section as function of the rapidity of the leptonic decay products of the W, the intermediate W boson, the neutron, and the proton, which emitted the photon, for $\kappa_W = 1$ in p-p collisions at LHC on a logarithmic and a linear scale.

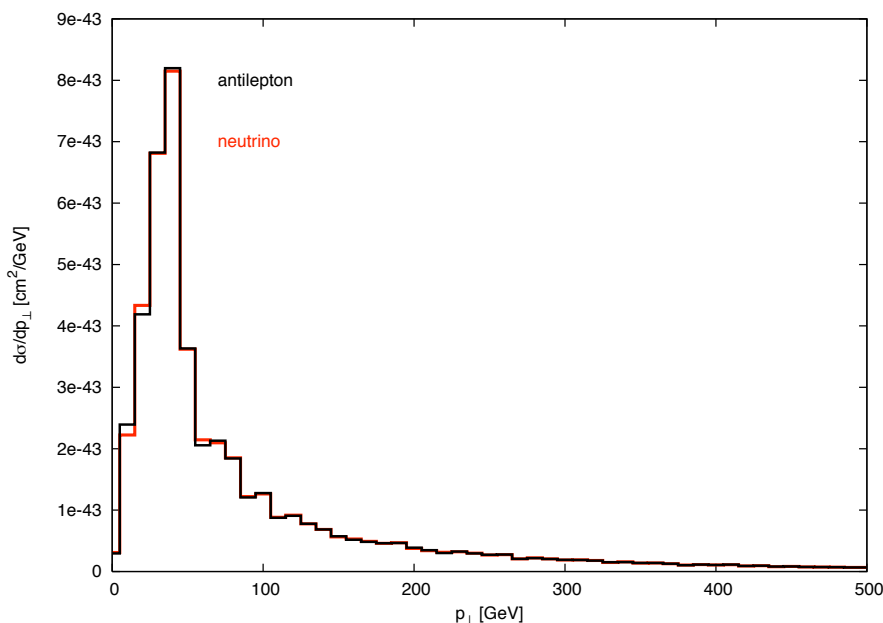


Figure 5.23: Differential cross section as function of the transverse momentum of the leptonic decay products of the W for $\kappa_W = 1$ in p-p collisions at LHC.

to check the contribution of the diagram of Fig. 5.24(c). The amplitude of this diagram is largest if the momentum transfers of the photon and the W boson k^2 and q^2 , respectively, are as small as possible. Therefore the lepton pair invariant mass is most likely very small. The invariant mass of the anti-lepton and the neutrino produced according to the diagrams in Fig. 5.18 is, in

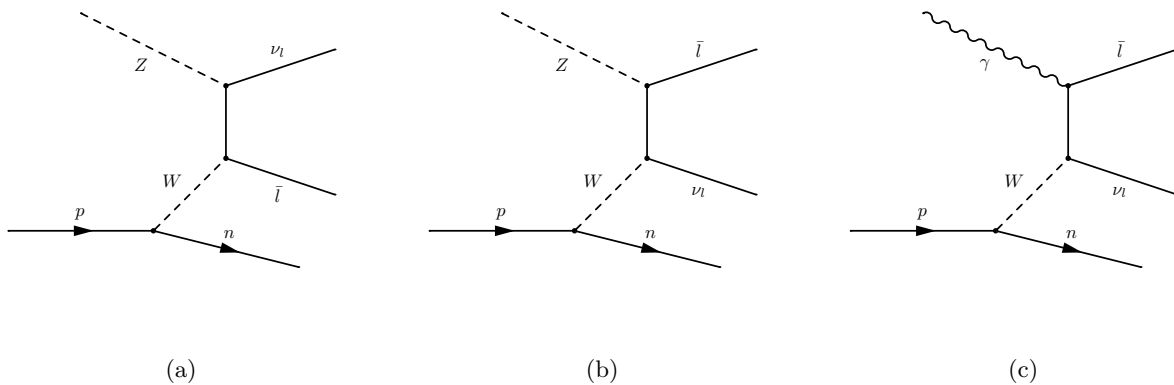


Figure 5.24: Additional Feynman diagrams, which contribute to single W boson production when the the subsequent decay is taken into account.

contrast, approximately the W boson mass. Likewise, Breitweg et al. [11] state in their paper that the diagrams of Fig 5.24 primarily give rise to low p_{\perp} charged leptons and lepton-neutrino invariant masses far from the W mass. Therefore, contributions of the diagrams of the type of those in Fig. 5.24 should be well distinguishable from those we are interested in here.

5.5 Conclusions

We calculated the cross section for (real) photoproduction of single W bosons and cross-checked our results against those of Fearing et al. [13, 14], who have calculated this cross section but with a smaller W boson mass in mind. We then extended these calculations by additionally including a weak magnetic form factor and the correct W boson mass. Furthermore, we examined how the choice of the (almost unknown) timelike weak form factor affects the photoproduction cross section. We follow the works of Fearing et al. [13, 14] and Kallianpur [56], who gave results for constant and dipole timelike form factors. When constant timelike form factors are used, the results do not differ from results of calculations where no form factors are used at all. Moreover, cross sections calculated with constant timelike form factors are not sensitive to the $WW\gamma$ coupling. Employing dipole timelike form factors affects the results in two ways: First, the cross sections are strongly suppressed due to the restriction to small momentum transfers. Second, the contribution of the diagram involving the $WW\gamma$ coupling becomes dominant and, thus, the total cross section becomes sensitive to the $WW\gamma$ coupling.

We convolved the photoproduction results with the equivalent photon spectra of ions and protons in order to obtain an estimate of the cross sections in p-p and Pb-p collisions at the LHC. The total cross section in Pb-p collisions at the LHC turns out to be $\sim 10^{-36}$ cm², which is, regarding an expected luminosity in Pb-p collisions of $\mathcal{L}_{\text{Pb-p}} \approx 10^{29}$ cm⁻²s⁻¹ and a planned measurement time of only one month, too low to yield viable amounts of events.

For p-p collisions there are two possibilities: The equivalent photon can either be radiated elastically, i. e. by the proton as a whole, or it can be radiated deep inelastically, i. e. by an individual quark inside the proton. We calculated cross sections for both and obtained total cross sections of the order of $\sim 10^{-39}$ cm² in both cases. From this, ~ 100 events per year can be expected in the very high luminosity p-p runs.

Since the W decays almost immediately, it can only be measured through its decay products. The most important decay channel, in the sense that it has the cleanest signal in experiments, is the leptonic decay. Therefore, we included the decay of the W^+ into an anti-lepton and the corresponding neutrino in our calculations. However, if we regard only the decay of the W bosons into μ^+ and ν_{μ} , we end up with ~ 10 events per year. Still, this number can be multiplied by a

factor of two since the protons in p-p collisions can be both: either projectile or target. Based on these rates, this process can likely be observed in p-p collisions at the LHC.

A Monte Carlo Event Generator for Low Energy Photo-Absorption Experiments

A.1 Motivation

The total cross section for the nuclear absorption of photons of defined energies is a testing ground for the validity of nuclear model calculations as well as for model independent sum rules. In particular, theoretical calculations employing nuclear potentials in few body systems need to be tested experimentally.

A way to measure the total photon absorption cross section of atoms [66, 67] is by the attenuation method sketched in Fig. A.1. The basic equation of this method,

$$N(E) = N_0(E) \exp(-n \sigma_{tot}(E)) , \tag{A.1}$$

gives the rate of photons after a piece of matter (absorber), which is characterized by the number of nuclei (atoms) n and the total photon absorption cross section $\sigma_{tot}(E)$ at a given photon energy. The ratio $N(E)/N_0(E)$ is obtained by measuring the photon flux with and without absorber in the beam. The total photon absorption cross section consists of two parts: the nuclear photo-absorption cross section, which is the one of interest, and the 'electronic' cross section, which has to be subtracted. The electronic cross section in the energy region of interest is mainly composed of the Compton cross section and the cross section for electron pair production in the (shielded) nuclear field and in the field of the electrons (Triplet production). Other possible contributions like the atomic photo-effect, for example, are negligible in the photon energy range of these experiments ($E_\gamma \approx 10 - 200$ MeV). As part of the simulation of the experiment an event generator for electron pair production in the field of the atomic nucleus is needed. Here, we

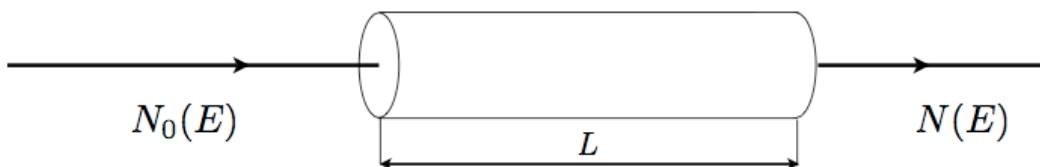


Figure A.1: Schematic view of the attenuation method.

explain how an event generator is developed in general (section A.2) as well as in this particular case (section A.3).

A.2 Monte Carlo Event Generation

The term Monte Carlo methods refers to a wide range of numerical methods which are based on random numbers. On the one hand, an important application of Monte Carlo methods is the numerical evaluation of multidimensional integrals with complicated boundaries, introduced in Appendix B. On the other hand, Monte Carlo methods are used to mimic 'random' processes. In particle physics, for example, Monte Carlo event generators are used to generate scattering events, i. e. sets of outgoing particles produced in the interactions between two incoming particles. Particle physics event generators are often used for the design and study of the physics potential of future experiments. In this context, the term event refers to a phase space point, given by a set of independent variables which define the phase space. The number of independent variables determining the phase space mainly depends on the number of outgoing particles. Each such variable is generated randomly according to a given probability density function $p(x)$ which fulfills

$$\int_{-\infty}^{\infty} p(\xi) d\xi = 1 \quad (\text{A.2})$$

and is derived from the underlying interactions in the process.

Transformation Method

In order to generate random numbers according to a given probability density $p(x)$ we proceed as follows. First, we calculate the distribution function $\Phi(x)$ as the indefinite integral of the density $p(x)$

$$\Phi(x) = \int_{-\infty}^x p(\xi) d\xi \quad (\text{A.3})$$

and its inverse Φ^{-1} . Then, we generate uniformly distributed random numbers r ($0 \leq r \leq 1$). Finally, the random numbers generated according to the probability density $p(x)$ are given by

$$x = \Phi^{-1}(r). \quad (\text{A.4})$$

This method is often referred to as the transformation method. However, this requires the probability density to be analytically integrable and to have an integral, which can be analytically inverted. These are strong constraints which, in general, do not hold. An approximation to this method would be to evaluate the integral numerically and perform inverse interpolation on the computed values. Below, we will introduce two further methods, which are widely used for Monte Carlo generators in particle physics [68].

Rejection Method

To use the rejection method [69], the following prerequisites have to be fulfilled

- (i) We can find an upper bound $f(x)$ to the density $p(x)$

$$0 \leq p(x) \leq f(x). \quad (\text{A.5})$$

- (ii) The definite integral of the function $f(x)$ is known

$$A := \int_{-\infty}^{\infty} d\xi f(\xi) \geq \int_{-\infty}^{\infty} d\xi p(\xi) = 1. \quad (\text{A.6})$$

(iii) The indefinite integral

$$F(x) := \int_{-\infty}^x d\xi f(\xi) \quad (\text{A.7})$$

of $f(x)$ is invertible.

In order to generate events according to the density $p(x)$, we use the following algorithm, described in [69]

(1) Generate two random numbers r_1, r_2 from a uniform distribution.

(2) Calculate

$$x := F^{-1}(A \cdot r_1) \quad (\text{A.8})$$

and

$$y := f(x) \cdot r_2. \quad (\text{A.9})$$

(3) If

$$y \leq p(x) \quad (\text{A.10})$$

is satisfied, the event is accepted, otherwise it is rejected and we have to restart from step (1) in the algorithm.

In this algorithm, points in the x - y -plane which lie below the curve $f(x)$ are uniformly sampled and those points which do not lie below the curve $p(x)$ are rejected, i. e. do not count in the further analysis. The fraction of accepted events

$$\frac{\int_{-\infty}^{\infty} d\xi p(\xi)}{\int_{-\infty}^{\infty} d\xi f(\xi)} = \frac{1}{A} \quad (\text{A.11})$$

is a measure of the efficiency of the rejection algorithm. In an alternative notation a weight

$$w(x) = \frac{p(x)}{f(x)} \quad (\text{A.12})$$

can be assigned to each event. The rejection condition (A.10) then reads

$$r_2 \leq w(x). \quad (\text{A.13})$$

In this notation the term 'constant weight method', which is often used to refer to the rejection method, becomes obvious.

Variable Weight Method

Instead of rejecting events according to their weight, we can also keep all events, which are generated according to the probability density $f(x)$, and assign the weight $w(x)$ to each event. For further analysis this weighing factor has to be taken into account.

Multivariate Probability Densities

In the simulation of scattering processes the probability density, according to which events are generated, is proportional to the differential cross section $\frac{d^n\sigma}{dx^n}$, which, in general, is a function of several variables. Therefore, we have to generalize the concepts introduced so far to multidimensional settings. This can be done assuming that we can factorize the multivariate probability density

$$\frac{1}{\sigma} \frac{d^n\sigma}{dx^n} = p_1(x_1) \cdots p_n(x_n), \quad (\text{A.14})$$

where the functions $p_1(x_1), \dots, p_n(x_n)$ are proportional to the corresponding differential cross sections $d\sigma/dx_1, \dots, d\sigma/dx_n$. Next, one of the methods described above or a combination of them can be applied to generate the individual density functions $p_j(x_j)$. To each event i , consisting of n random numbers representing the n variables $x_1^{(i)}, \dots, x_n^{(i)}$, the weight

$$w_i(x_1^{(i)}, \dots, x_n^{(i)}) = \frac{d^n\sigma/dx^n}{p_1(x_1^{(i)}) \cdots p_n(x_n^{(i)})} \quad (\text{A.15})$$

is assigned. The total cross section can be estimated by summing up all weights $\sum_i w_i$ and dividing by the total number of generated events N .

A.3 Pair Production in the Atomic Field

In this section we discuss the application of the methods introduced in section A.2 to electron pair production events in the field of an atom. In this context, the term event refers to an electron-positron pair, where the particles are defined by their spatial momenta in a given Lorentz frame. The cross section for electron-positron pair production in the field of an atom

$$\gamma + A \longrightarrow e^+ + e^- + A \quad (\text{A.16})$$

is given by

$$\sigma = \frac{1}{F} \int |\mathcal{M}|^2 \frac{d^3P'}{2E'_0 (2\pi)^3} \frac{d^3p_+}{2\epsilon_+ (2\pi)^3} \frac{d^3p_-}{2\epsilon_- (2\pi)^3}, \quad (\text{A.17})$$

where P' is the momentum of the atom after the collision, p_- and p_+ are the momenta of the electron and the positron, respectively. The matrix element \mathcal{M} in this case is the one derived in chapter 4, which is used in the calculation employing the equivalent photon approximation. However, the form factors have to be replaced by those for an atom. We use the form factors provided by Salvat et al. in [70]. The phase space is defined by five independent variables, which we choose to be:

- $M_{e^+e^-}$, the invariant mass of the pair,
- Θ_1 and φ_1 , the angles defining the direction of the spatial momentum of the electron and the positron in the rest frame of the pair,
- Θ_2 and φ_2 , the angles defining the direction of the spatial momentum of the recoiling atom in the photon-Atom (γA) collider frame

according to the method introduced in appendix C.

For the realization of an event generator for this process, we employ a combination of the methods introduced in the preceding section. First, we assume the differential cross section

$$\frac{d\sigma}{dM_{e^+e^-} d\cos\Theta_1 d\cos\Theta_2 d\varphi_1 d\varphi_2} \propto |\mathcal{M}|^2 \quad (\text{A.18})$$

to factorize approximately and to be approximated by the product of five functions $f_1 \cdots f_5$, which approximate the differential cross sections as functions of the corresponding variable

$$\frac{1}{\sigma} \frac{d\sigma}{dM_{e^+e^-}} \approx f_1(x_1 = M_{e^+e^-}) \quad (\text{A.19})$$

$$\frac{1}{\sigma} \frac{d\sigma}{d \cos \Theta_1} \approx f_2(x_2 = \cos \Theta_1) \quad (\text{A.20})$$

$$\frac{1}{\sigma} \frac{d\sigma}{d \cos \Theta_2} \approx f_3(x_3 = \cos \Theta_2) \quad (\text{A.21})$$

$$\frac{1}{\sigma} \frac{d\sigma}{d\varphi_1} \approx f_4(x_4 = \varphi_1) \quad (\text{A.22})$$

$$\frac{1}{\sigma} \frac{d\sigma}{d\varphi_2} \approx f_5(x_5 = \varphi_2). \quad (\text{A.23})$$

The angles φ_1 and φ_2 are generated uniformly in the interval $[0, 2\pi]$. In the following, we outline how we obtain approximate expressions f_1 , f_2 , and f_3 . In all three cases we make use of the equivalent photon approximation, introduced in chapter 3, by replacing the field of the atom by a spectrum of equivalent photons and, thus, reducing the cross section to the one of pair production from two real photons. For the two-photon pair production cross section, an analytical form is given, e.g. in [8, 71]

$$\sigma_{\gamma\gamma} = \frac{4\pi\alpha^2}{s} \left[\left(2 + \frac{8m^2}{s} - \frac{16m^4}{s^2} \right) \log \left(\frac{\sqrt{s} + \sqrt{s - 4m^2}}{2m} \right) - \sqrt{1 - \frac{4m^2}{s}} \left(1 + \frac{4m^2}{s} \right) \right], \quad (\text{A.24})$$

with $s = M_{e^+e^-}^2$ and m the mass of the electron. We approximate $d\sigma/dM_{e^+e^-}$ by convolving the equivalent photon spectrum, given in [53],

$$n(\omega_2) = \frac{Z^2\alpha}{\pi} \log \left(\left(\frac{\delta}{\xi} \right)^2 + 1 \right) \quad (\text{A.25})$$

with the two-photon cross section of equation (A.24)

$$\int \sigma_{\gamma\gamma} n(\omega_2) \frac{d\omega_2}{\omega_2} = \int \sigma_{\gamma\gamma} n(s) \frac{2dM_{e^+e^-}}{M_{e^+e^-}}. \quad (\text{A.26})$$

In equation (A.25) $\delta \approx 0.681$ is a number related to Euler's constant and $\xi = \omega_2 R / \gamma\beta$, where ω_2 denotes the energy of the equivalent photon in the γA collider frame. In our case ξ is given by $\xi = \frac{Rs}{2E_\gamma}$ with E_γ the energy of the real photon in the rest system of the atom and $R = 1/m$ for elastic scattering. As an approximation to the differential cross section as function of $M_{e^+e^-}$ we obtain the following expression

$$f_1(x_1) \propto \frac{1}{x_1^3} \left\{ \left(2 + \frac{8m^2}{x_1^2} - \frac{16m^4}{x_1^4} \right) \log \left(\frac{x_1 + \sqrt{x_1^2 - 4m^2}}{2m} \right) - \sqrt{1 - \frac{4m^2}{x_1^2}} \left(1 + \frac{4m^2}{x_1^2} \right) \right\} \quad (\text{A.27})$$

$$\times \log \left[\left(\frac{2\delta E_\gamma}{x_1^2 R} \right)^2 + 1 \right], \quad (\text{A.28})$$

which needs to be normalized to fulfill

$$\int_{2m}^{M_{max}} f_1(M_{e^+e^-}) dM_{e^+e^-} = 1. \quad (\text{A.29})$$

The maximum producible invariant mass M_{max} depends on the photon energy E_γ . In Fig. A.2 we present the function $f_1(x_1)$ for three different values of the photon energy $E_\gamma = 10$ MeV,

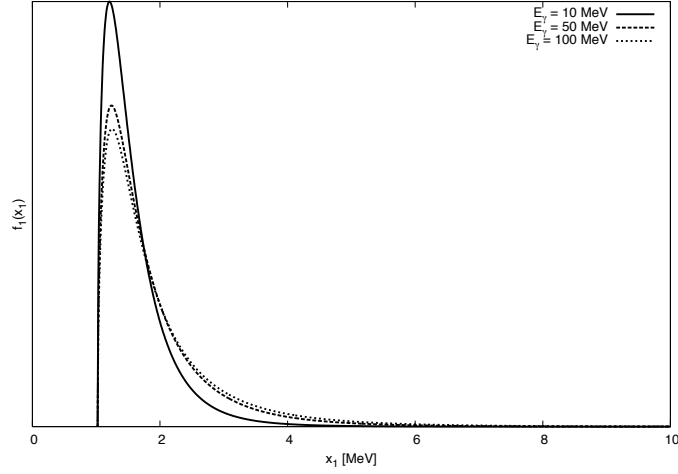


Figure A.2: Approximation f_1 to the differential cross section as function of the invariant mass of the electron-positron pair for different values of the photon energy $E_\gamma = 10$ MeV, 50 MeV, and 100 MeV.

50 MeV, and 100 MeV.

An approximation to the differential cross section $d\sigma/d\cos\Theta_1$ can be obtained by convolving the equivalent photon spectrum of equation (A.25) with the differential cross section of two-photon pair production as function of $\cos\Theta_1$ given in [8, 71] by

$$\frac{d\sigma_{\gamma\gamma}}{d\cos\Theta_1} = \frac{2\pi\alpha^2}{s} \sqrt{1 - \frac{4m^2}{s}} \frac{1 + \left(\frac{8m^2}{s} - \frac{32m^4}{s^2}\right) (1 - \cos^2\Theta_1) - \left(1 - \frac{8m^2}{s} + \frac{16m^4}{s^2}\right) \cos^4\Theta_1}{\left(1 - \left(1 - \frac{4m^2}{s}\right) \cos^2\Theta_1\right)^2} \quad (\text{A.30})$$

Instead of integrating over $M_{e^+e^-}$ in the convolution with the photon spectrum, we evaluate the differential cross section at the value $M_{e^+e^-} = 3m$ and obtain the simple expression

$$f_2(x_2) \propto \frac{121 - 40x_2^2 - 25x_2^4}{(9 - 5x_2^2)^2}. \quad (\text{A.31})$$

This is still a good approximation, since the differential cross section $d\sigma/dM_{e^+e^-}$ peaks around $M_{e^+e^-} = 3m$, see Fig. A.2. As can be seen from equation (A.31) the function f_2 is independent of the photon energy E_γ . The behavior of the differential cross section as function of $\cos\Theta_1$ can be seen in Fig. A.3, where we show the function $f_2(x_2)$.

In the equivalent photon spectrum of equation (A.25) the integration over $\cos\Theta_2$ is already carried out. In order to obtain an approximation to the differential cross section $d\sigma/d\cos\Theta_2$ we have to go back to the form

$$n(\omega_2) = \frac{Z^2\alpha}{\pi^2} \int d^2p_\perp \frac{q_\perp^2}{(q^2)^2} |F_{el}(q^2)|^2 \quad (\text{A.32})$$

of the equivalent photon spectrum with $-q^2 = q_\perp^2 + \left(\frac{\omega_2}{\gamma\beta}\right)^2$ in the elastic case. It is sufficient to set $F_{el} = 1$ in this approximation. The angle Θ_2 enters the equation through

$$q_\perp^2 = |\vec{P}'|^2 \sin^2\Theta_2 \quad (\text{A.33})$$

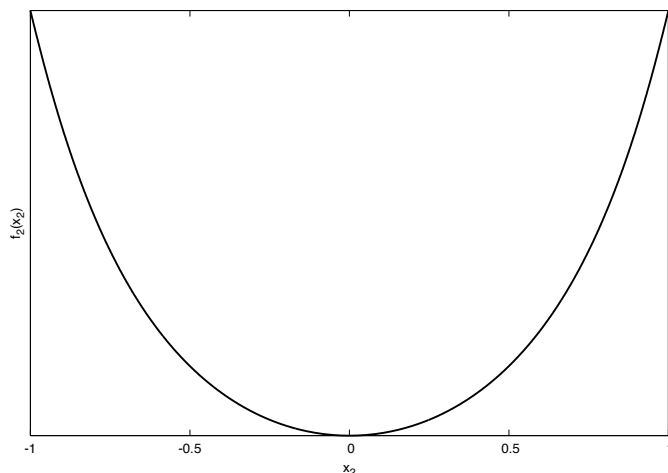


Figure A.3: Approximation f_2 to the differential cross section as function of $\cos \Theta_1$.

with \vec{P}' being the spatial momentum of the atom after the collision in the γA collider frame. The integration variable $d^2 q_\perp$ can be transformed into $d\cos \Theta_2$ using

$$d^2 p_\perp \propto \cos \Theta_2 d\cos \Theta_2. \quad (\text{A.34})$$

Again, we simplify the differential cross section by evaluating it at $M_{e^+e^-} = 3m$ instead of integrating over the invariant mass. This leads to

$$f_3(x_3) \propto \frac{(1 - x_3^2)x_3}{(q^2(x_3))^2}, \quad (\text{A.35})$$

where $q^2(x_3)$ depends on the mass M_A and the charge Z of the atomic nucleus, as well as on the photon energy E_γ in the rest system of the atom. In Fig. A.4 we present the function $f_3(x_3)$ for a photon energy of $E_\gamma = 100$ MeV for ${}^7\text{Li}$.

With these approximations to the differential cross sections, we have an idea of the behavior of the differential cross sections (see Figs A.2-A.4). There are now several strategies how to proceed:

1. We generate the variables x_1 , x_2 , and x_3 according to the density functions f_1 , f_2 , and f_3 , respectively, and assign to each event the weight

$$w_i = \frac{d\sigma}{dx_1^{(i)} dx_2^{(i)} dx_3^{(i)} dx_4^{(i)} dx_5^{(i)}} \cdot \frac{1}{f_1^{(i)} \cdot f_2^{(i)} \cdot f_3^{(i)}}. \quad (\text{A.36})$$

To generate events according to the functions f_j , we can use the rejection method. To this purpose we have to find for each f_j a function \bar{f}_j , which

- is integrable and whose integral can be inverted analytically,
- resembles f_j ,
- is strictly larger than f_j over the interval of interest.

It is complicated to find a function for each density, which fulfills all three requirements. In particular, these functions depend on the external parameters of the scattering process, like the type of atoms and the photon energy E_γ , in a non-trivial way. Therefore, a more general method for the event generation has to be found.

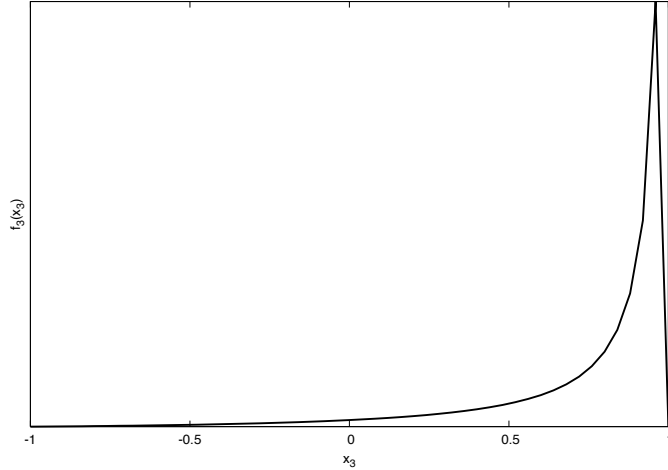


Figure A.4: Approximation f_3 to the differential cross section as function of $\cos \Theta_2$ for $E_\gamma = 100$ MeV and ${}^7\text{Li}$ as target atoms.

2. We can use uniformly distributed random numbers for all phase space variables and use the variable weight method to reconstruct total and differential cross sections. However, this method is very inefficient since especially $M_{e^+e^-}$ and $\cos \Theta_2$ have pronounced peaks (see Figs A.2 and A.4), which are not sampled appropriately using a uniform distribution.
3. In an improved version of strategy 2, we generate the variables x_1 and x_3 according to densities, which mimic the general behavior of f_1 and f_3 , respectively, and subsequently employ the variable weight method. To mimic the peaks of the functions $f_1(x_1)$ and $f_3(x_3)$, we use the probability density

$$\tilde{p}(x) = \frac{C}{\log(C+1)} \frac{1}{Cx+1} \quad (\text{A.37})$$

with $C = 10^7$ to generate random numbers between 0 and 1 and subsequently map them on the intervals, where $f_1(x_1)$ and $f_3(x_3)$ are defined.

In Fig. A.5 we compare the approximation $f_2(x_2)$ of equation (A.31) to the normalized differential cross section as function of $\cos \Theta_1$ for strategy 2 with $N = 5 \cdot 10^6$ generated events and for strategy 3 with $N = 10^6$ generated events. From this figure, it is obvious that a much better approximation of the cross section can be obtained with strategy 3. The same can be seen by looking at the numerical values for the total cross section in table A.1, which we obtain by summing up the weights

$$\sigma \approx \sum_i \frac{w_i}{N}, \quad (\text{A.38})$$

and comparing them to the total cross sections for pair production in the screened nuclear field given in [72]. An estimate of the error in this case is given by

$$\Delta\sigma \approx \sqrt{\frac{\sum_i w_i^2 - \frac{1}{N} (\sum_i w_i)^2}{N(N-1)}} \quad (\text{A.39})$$

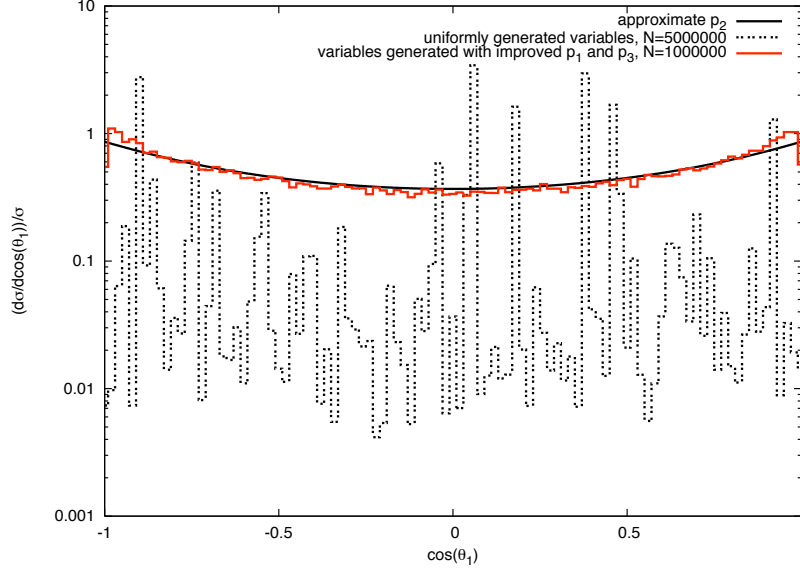


Figure A.5: Comparison between f_2 from equation (A.31) (black solid line) and the normalized differential cross section as function of $\cos \Theta_1$ with $N = 5 \cdot 10^6$ uniformly sampled points (black dashed line) and $N = 10^6$ points sampled according to improved densities p_1 and p_3 (red line).

Table A.1: Total cross sections for the process $\gamma + A \rightarrow e^+ + e^- + A$ for different photon energies E_γ for ${}^7\text{Li}$ as target atoms obtained with strategies 2 and 3 and compared to the cross sections given in [72].

E_γ [MeV]	N	cross section [barn] and estimated error from strategy 2	cross section [barn] and estimated error from strategy 3	cross section [barn] from [72]
10	10^4	$1.72 \cdot 10^{-2} \pm 9.74 \cdot 10^{-3}$	$1.91 \cdot 10^{-2} \pm 7.56 \cdot 10^{-4}$	$1.92 \cdot 10^{-2}$
10	10^5	$1.58 \cdot 10^{-2} \pm 2.24 \cdot 10^{-3}$	$1.89 \cdot 10^{-2} \pm 2.32 \cdot 10^{-4}$	$1.92 \cdot 10^{-2}$
10	$5 \cdot 10^5$	$1.78 \cdot 10^{-2} \pm 1.48 \cdot 10^{-3}$	$1.89 \cdot 10^{-2} \pm 1.03 \cdot 10^{-4}$	$1.92 \cdot 10^{-2}$
10	10^6	$1.82 \cdot 10^{-2} \pm 1.09 \cdot 10^{-3}$	$1.89 \cdot 10^{-2} \pm 7.27 \cdot 10^{-5}$	$1.92 \cdot 10^{-2}$
50	10^4	$6.18 \cdot 10^{-3} \pm 5.17 \cdot 10^{-3}$	$4.44 \cdot 10^{-2} \pm 1.50 \cdot 10^{-3}$	$4.36 \cdot 10^{-2}$
50	10^5	$5.22 \cdot 10^{-2} \pm 1.23 \cdot 10^{-3}$	$4.40 \cdot 10^{-2} \pm 4.70 \cdot 10^{-4}$	$4.36 \cdot 10^{-2}$
50	$5 \cdot 10^5$	$1.08 \cdot 10^{-2} \pm 2.82 \cdot 10^{-3}$	$4.28 \cdot 10^{-2} \pm 2.06 \cdot 10^{-4}$	$4.36 \cdot 10^{-2}$
50	10^6	$1.09 \cdot 10^{-2} \pm 1.86 \cdot 10^{-3}$	$4.30 \cdot 10^{-2} \pm 1.45 \cdot 10^{-4}$	$4.36 \cdot 10^{-2}$
100	10^4	$2.00 \cdot 10^{-3} \pm 1.72 \cdot 10^{-3}$	$5.26 \cdot 10^{-2} \pm 2.03 \cdot 10^{-3}$	$5.32 \cdot 10^{-2}$
100	10^5	$9.75 \cdot 10^{-3} \pm 8.17 \cdot 10^{-3}$	$5.32 \cdot 10^{-2} \pm 6.60 \cdot 10^{-4}$	$5.32 \cdot 10^{-2}$
100	$5 \cdot 10^5$	$4.49 \cdot 10^{-3} \pm 1.30 \cdot 10^{-3}$	$5.23 \cdot 10^{-2} \pm 2.93 \cdot 10^{-4}$	$5.32 \cdot 10^{-2}$
100	10^6	$4.27 \cdot 10^{-3} \pm 8.09 \cdot 10^{-4}$	$5.28 \cdot 10^{-2} \pm 2.09 \cdot 10^{-4}$	$5.32 \cdot 10^{-2}$

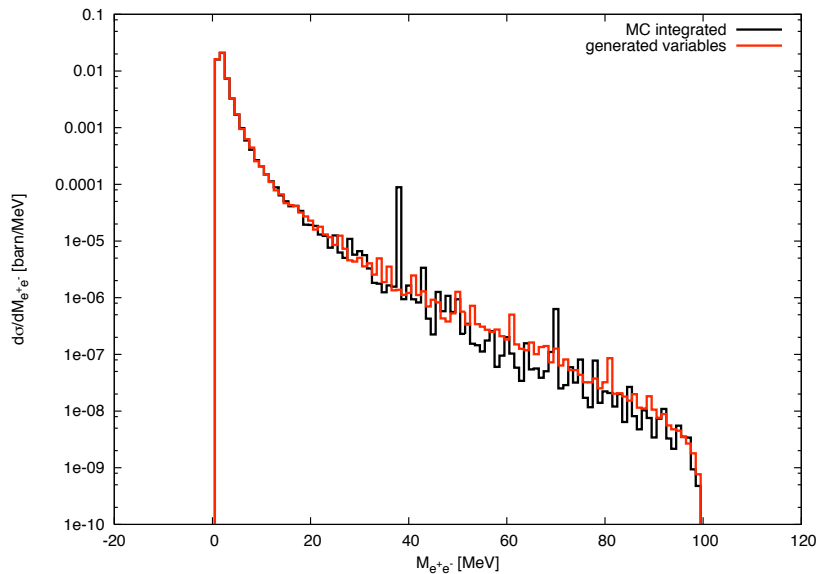


Figure A.6: Differential cross section as function of the invariant mass of the e^+e^- pair for an initial photon energy of $E_\gamma = 100\text{MeV}$ for ${}^7\text{Li}$ as target atom.

A.4 Conclusions

We developed an event generator for electron pair production in the field of an atomic nucleus. It generates events consisting of a set of independent variables, from which the four momenta of the produced pair can be reconstructed. To each event we assign a weight, from which, for a large number N of generated events, the total cross section can be estimated. We tried two strategies: First, we generated all variables according to a uniform distribution. After $N \sim 10^6$ events, the total cross section as given in [72] can still not be reconstructed for high photon energies E_γ . Second, we try a more efficient method, where the two variables $M_{e^+e^-}$ and $\cos \Theta_2$, which are strongly peaked, are generated according to density functions which mimic this peaking structure. Using this method, we get a reasonable estimate of the total cross section (cp. [72]) already for $N = 10^5$ even for high photon energies. As a further test of the event generation with this method, we reproduce various differential cross sections and compare them to the ones obtained by a Monte Carlo integration (see appendix B) of the matrix element (see Figs. A.6-A.11) for a photon energy of $E_\gamma = 100\text{MeV}$ for ${}^7\text{Li}$.

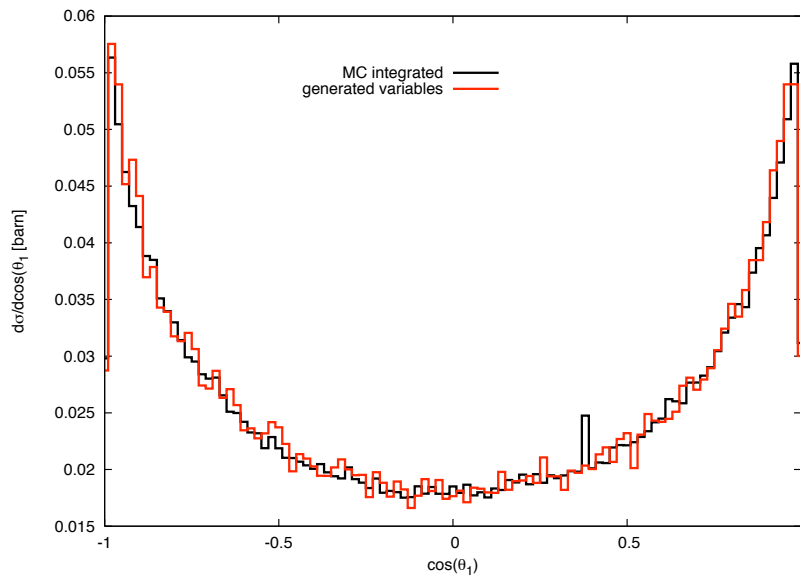


Figure A.7: Differential cross section as function of $\cos \Theta_1$ for an initial photon energy of $E_\gamma = 100\text{MeV}$ for ${}^7\text{Li}$ as target atom.

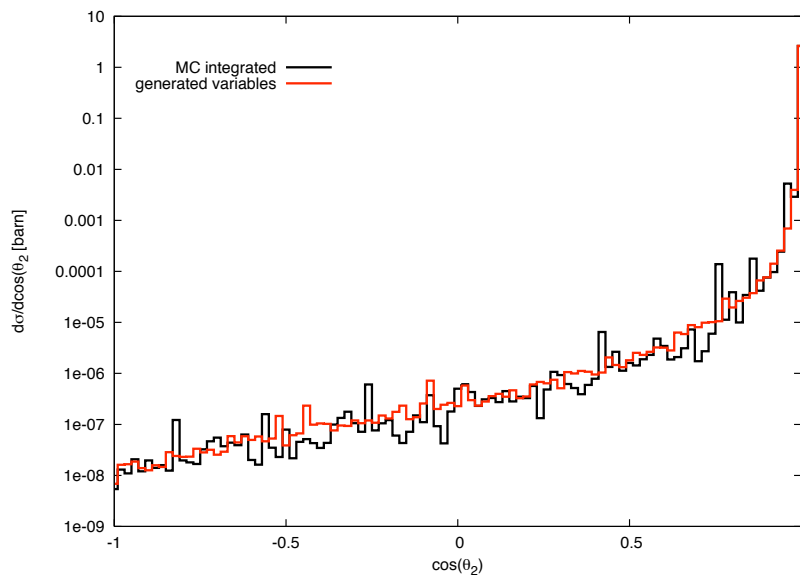


Figure A.8: Differential cross section as function of $\cos \Theta_2$ for an initial photon energy of $E_\gamma = 100\text{MeV}$ for ${}^7\text{Li}$ as target atom.

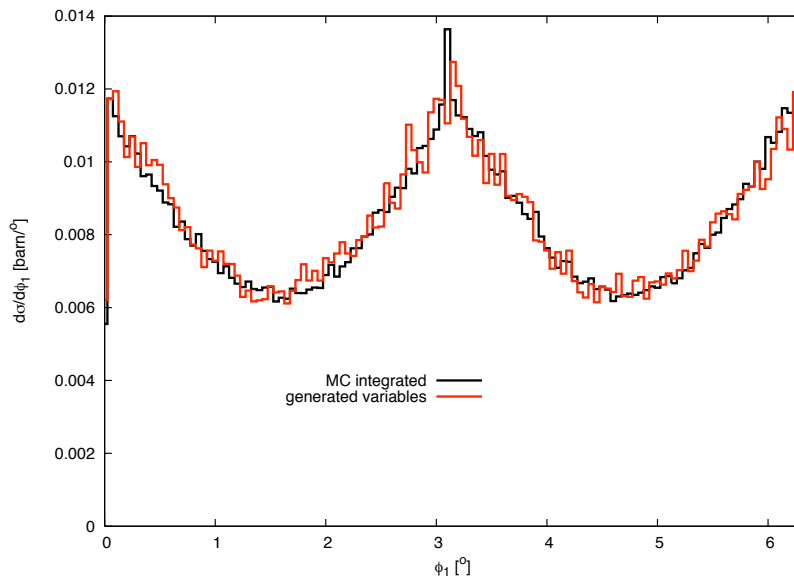


Figure A.9: Differential cross section as function of the angle φ_1 for an initial photon energy of $E_\gamma = 100\text{MeV}$ for ${}^7\text{Li}$ as target atom.

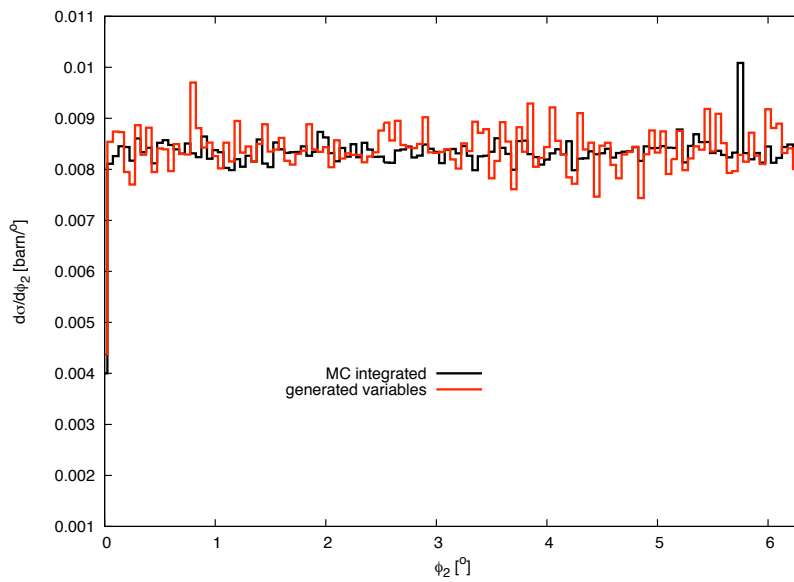


Figure A.10: Differential cross section as function of the angle φ_2 for an initial photon energy of $E_\gamma = 100\text{MeV}$ for ${}^7\text{Li}$ as target atom.

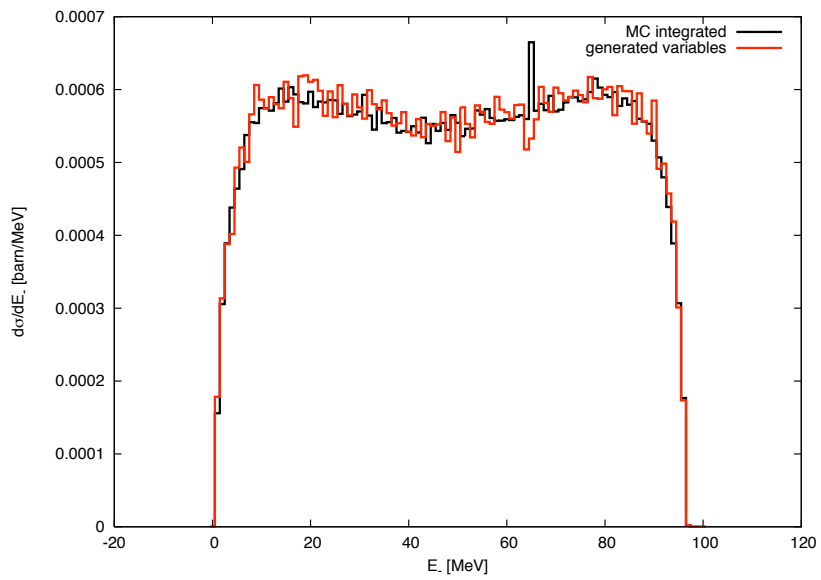


Figure A.11: Differential cross section as function of the energy of the electron ϵ_- for an initial photon energy of $E_\gamma = 100\text{MeV}$ for ${}^7\text{Li}$ as target atom.

Monte Carlo Integration

The calculation of cross sections involves the integration of the squared matrix element over several dimensions. The phase space over which the integration is carried out is a multidimensional hypervolume with a, in general, complicated boundary surface. In the majority of the cases, Monte Carlo integration is the most suitable method to evaluate integrals of this type, i.e. integrals in high dimensions and with a non-trivial boundary surface. We will briefly outline this method here, whereas more detailed descriptions can be found, e.g. in [73, 63]. The basic idea of Monte Carlo integration is to evaluate an integral of the type

$$I := \int f dV \tag{B.1}$$

by evaluating the function f at N randomly chosen sampling points X_1, \dots, X_N in the hypervolume V

$$\langle f \rangle_N = \frac{1}{N} \sum_{i=1}^N f(X_i), \tag{B.2}$$

where

$$\lim_{N \rightarrow \infty} \langle f \rangle_N = \langle f \rangle = \frac{1}{V} \int f dV. \tag{B.3}$$

The integral is therefore estimated based on that random sample

$$\int f dV \approx V \cdot \frac{1}{N} \sum_{i=1}^N f(X_i). \tag{B.4}$$

The multidimensional region V over which the integration in equation (B.1) is performed may have a complicated boundary surface. However, for the Monte Carlo integration it is sufficient to know

- (i) a region with simple boundaries, which includes the complicated region
- (ii) a method of determining whether a random point is inside or outside the region of integration.

This is one of the great advantages of the Monte Carlo method over other numerical integration methods.

If we make several estimates of the integral for different sets of random numbers, we obtain a normal distribution of estimates for sufficiently large N according to the central limit theorem

of probability theory. An estimate of the error of the approximate evaluation of the integral by equation (B.4) is given by the standard deviation

$$\sigma_N = \sqrt{\frac{\langle f^2 \rangle - \langle f \rangle^2}{N-1}} \quad (\text{B.5})$$

with $\langle f^2 \rangle$ defined as

$$\langle f^2 \rangle = \frac{1}{N} \sum_i f^2(X_i) \quad (\text{B.6})$$

and $\langle f \rangle$ as in equation (B.2). This means that 68.3% of the estimates will lie within one standard deviation σ_N of the mean $\langle f \rangle_N$. Or likewise, 95.4% (99.7%) of all estimates lie within two (three) standard deviations of the mean. Thus we can state

$$\int f dV = V \cdot (\langle f \rangle_N \pm \sigma_N) \quad (\text{B.7})$$

with 68.3% confidence. The error in the Monte Carlo integration decreases as $1/\sqrt{N}$, which is rather slow compared to other numerical integration methods. However, for a large number d dimensions, the Monte Carlo integration method is favorable, since the error is reduced by a factor of two if the number of sample points N is increased by a factor of four, independent of the number of dimensions of the integral. Whereas in other methods N has to be increased by a factor of e.g. $2^{d/2}$ for the trapezoidal rule or by a factor of $2^{d/4}$ for Simpson's rule in order to decrease the error by a factor of two.

There are a couple of techniques which are able to enhance the accuracy of the Monte Carlo method.

Importance Sampling

For example, we can exploit information, which we might already have, on the function we want to integrate. Assume, for example, we have an approximate expression g that resembles f to some extent in the relevant region. Consequently, we can write

$$\int \left(\frac{f}{g} \right) g dV. \quad (\text{B.8})$$

Instead of sampling f with a uniform probability density, we sample the almost constant function f/g according to the non-uniform probability density g . This corresponds to a change of variable from X to $Y = G(X)$, the indefinite integral of g . Hence, importance sampling consists, in principle, in placing a large number of sampling points, where the function f is large. The statistical error vanishes for $g = f$, but that would correspond to already knowing the integral of f , since we need it for sampling the points according to $g = f$ and using Monte Carlo methods for the integration would be absolutely needless.

Stratified Sampling

In stratified sampling the hyper-volume V is divided into subvolumes, which are sampled with different numbers of points each. The optimal choice of the number of sample points N_j in a subvolume V_j can be shown to be proportional to the square root of the variance of the function f in this subregion

$$\sqrt{\sigma_j^2} = [\text{Var}_j(f)]^{1/2} = \left[\frac{1}{V_j} \int f^2 dV_j - \left(\frac{1}{V_j} \int f dV_j \right)^2 \right]^{1/2}. \quad (\text{B.9})$$

Thus, stratified sampling concentrates points where the variance is largest. However, this method is not very useful for high dimensional integrals, since the number of variances that have to be estimated along with the integrand increases with powers of d .

VEGAS

The VEGAS algorithm developed by Lepage [62] is widely used for multidimensional integrals which occur in elementary particle physics. The algorithm is primarily based on importance sampling. To this purpose a separable weight function

$$g(x_1, \dots, x_d) = g_1(x_1)g_2(x_2) \dots g_d(x_d) \quad (\text{B.10})$$

is assumed, where x_j denote the coordinates in the d -dimensional hyper-volume V . The optimal separable weight function, in the sense that it minimizes the error σ_N , can be shown to be

$$g_1(x_1) \propto \left[\int dx_2 \dots \int dx_d \frac{f^2(x_1, \dots, x_d)}{g_2(x_2) \dots g_d(x_d)} \right]^{1/2} \quad (\text{B.11})$$

and correspondingly for x_2, \dots, x_d . VEGAS constructs this weight function adaptively and uses it according to equation (B.8). That is, it starts with an initial set of g -functions $g_1^{(0)}, \dots, g_d^{(0)}$, samples the function f , and estimates, simultaneously, the functions $g_j^{(1)}$ according to equation (B.12). These improved g -functions $g_1^{(1)}, \dots, g_d^{(1)}$ are then used for the next step in the iteration.

$$g_1^{(n+1)}(x_1) \propto \left[\int dx_2 \dots \int dx_d \frac{f^{(n)2}(x_1, \dots, x_d)}{g_2^{(n)}(x_2) \dots g_d^{(n)}(x_d)} \right]^{1/2} \quad (\text{B.12})$$

From m statistically independent evaluations of the integral I_j , where each iteration j is used to refine the sampling grid for the next one, a best answer and the corresponding estimated error can be given as

$$I_{best} = \frac{\sum_{j=1}^m I_j}{\sum_{j=1}^m \frac{1}{\sigma_j^2}} \quad (\text{B.13})$$

$$\sigma_{best} = \left(\sum_{j=1}^m \frac{1}{\sigma_j^2} \right)^{-1/2}. \quad (\text{B.14})$$

The quantity

$$\frac{\chi^2}{m} = \frac{1}{m-1} \sum_{j=1}^m \frac{(I_j - I_{best})^2}{\sigma_j^2} \quad (\text{B.15})$$

tests the statistical consistency of the results of the individual iterations.

Another feature of the VEGAS algorithm is, that the integrand function f has an additional argument w_i , which can be used to integrate some additional function or functions along with the principal function f . The integral of such a function h can be estimated by

$$I_h = \sum_i w_i \cdot h. \quad (\text{B.16})$$

Of course, this estimate is better, if the function h resembles the principal function f to some extent, since the sampling grid is optimized for f . We mainly use this feature to obtain differential distributions along with the total cross section according to

$$\frac{d\sigma}{dz} = \frac{n_b \sigma}{(z_{max} - z_{min})N} \sum_{z \in \text{bin}} w \quad (\text{B.17})$$

in our calculations, where n_b is the number of bins, σ is the integral of the principal function, and the differential cross section is given in the interval $[z_{min}, z_{max}]$.

Phase Space Generation

As already explained in section 2.2 the total cross section for the scattering of two incoming particles into a set of n outgoing particles

$$p_a + p_b \longrightarrow p_1 + p_2 + \dots + p_n \quad (\text{C.1})$$

is given by

$$\sigma = \int |\mathcal{M}|^2 dPS_n \quad (\text{C.2})$$

where the phase space of the n final particles is formally given by

$$dPS_n = \prod_{i=1}^n \left(\frac{d^3 p_i}{2\epsilon_i (2\pi)^3} \right) (2\pi)^4 \delta^4 \left(p_a + p_b - \sum_{j=1}^n p_j \right). \quad (\text{C.3})$$

The integration over the phase-space is an $3n - 4$ - dimensional integration, where the integration variables might depend on each other in a non-trivial way. An efficient way to integrate over a n particle phase space is given in the textbook of Byckling and Kajantie [15]. We will briefly outline this method here. For $|\mathcal{M}|^2 = 1$ the phase space integral is

$$R_n(p) = \frac{1}{(2\pi)^{3n-4}} \int \prod_{i=1}^n \frac{d^3 p_i}{2\epsilon_i} \delta^4 \left(p - \sum_{j=1}^n p_j \right). \quad (\text{C.4})$$

with $p = (p_a + p_b)$. The phase space of the process $p_a + p_b \longrightarrow p_1 + \dots + p_n$ can be decomposed into a sequence of two particle decays, where an initial particle of four momentum p decays into a particle of four momentum p_n and the rest, to which we assign a four momentum k_{n-1} and

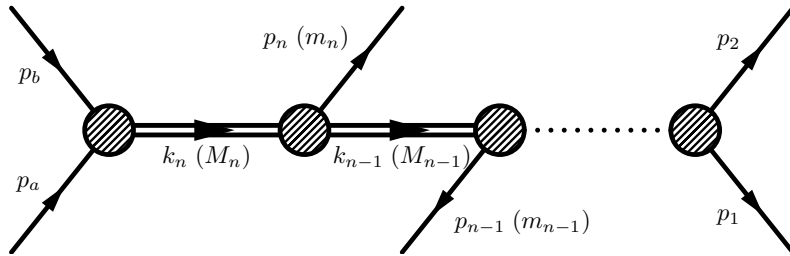


Figure C.1: Schematic picture of the decay cascade describing the process $p_a + p_b \longrightarrow p_1 + \dots + p_n$ and providing an efficient phase space integration

which subsequently decays into particles with four momenta p_{n-1} and k_{n-2} , see Fig. C. For the phase space integral R_n an iterative equation can be derived

$$\begin{aligned} R_n(p) &= \frac{1}{(2\pi)^{3n-4}} \int \frac{d^3 p_n}{2\epsilon_n} \int \prod_{i=1}^{n-1} \frac{d^3 p_i}{2\epsilon_i} \delta^4 \left((p - p_n) - \sum_{j=1}^{n-1} p_j \right) \\ &= \frac{1}{(2\pi)^3} \int \frac{d^3 p_n}{2\epsilon_n} R_{n-1}(p - p_n), \end{aligned} \quad (\text{C.5})$$

where R_{n-1} is a function of $k_{n-1} = (p - p_n)$ and

$$k_i = p_1 + p_2 + \dots + p_i \quad (\text{C.6})$$

$$k_n = p = p_a + p_b. \quad (\text{C.7})$$

Inserting the unities

$$1 = \int dM_{n-1}^2 \delta(M_{n-1}^2 - k_{n-1}^2) \quad (\text{C.8})$$

$$1 = \int d^4 k_{n-1} \delta^4(p - p_n - k_{n-1}), \quad (\text{C.9})$$

where M_i denotes the invariant mass of the subsystem $k_i = p_1 + \dots + p_i$, the phase space integral R_n can be rewritten as

$$\begin{aligned} R_n(M_n^2) &= \frac{1}{(2\pi)^3} \int dM_{n-1}^2 \int d^4 k_{n-1} \int d^4 p_n \delta(k_{n-1}^2 - M_{n-1}^2) \\ &\quad \times \delta(p_n^2 - m_n^2) \delta^4(p - p_n - k_{n-1}) R_{n-1}(M_{n-1}^2). \end{aligned} \quad (\text{C.10})$$

R_2 , the phase space integral for the decay of a particle of mass $\sqrt{p^2}$ into two particles, is given by

$$\begin{aligned} R_2(p^2, m_1^2, m_2^2) &= \frac{1}{(2\pi)^2} \int d^4 p_1 d^4 p_2 \delta(p_1^2 - m_1^2) \delta(p_2^2 - m_2^2) \delta^4(p - p_1 - p_2) \\ &= \frac{\lambda^{1/2}(p^2 = M_2^2, m_1^2, m_2^2)}{8M_2^2} \int d\Omega_1 \end{aligned} \quad (\text{C.11})$$

with

$$\lambda(x, y, z) = (x - y - z)^2 - 4yz. \quad (\text{C.12})$$

Inserting

$$\begin{aligned} R_2(k_n^2, k_{n-1}^2, p_n^2) &= \int d^4 k_{n-1} d^4 p_n \delta(k_{n-1}^2 - M_{n-1}^2) \delta(p_n^2 - m_n^2) \delta^4(k_n - k_{n-1} - p_n) \\ &= \frac{\lambda^{1/2}(M_n^2, k_{n-1}^2, p_n^2)}{8M_n^2} \int d\Omega_1 \end{aligned} \quad (\text{C.13})$$

into the recursive expression for R_n (C.10) results in

$$R_n = \int 2M_{n-1} dM_{n-1} R_{n-1}(M_{n-1}^2) \frac{\lambda^{1/2}(M_n^2, k_{n-1}^2, p_n^2)}{8M_n^2} \int d\Omega_1. \quad (\text{C.14})$$

Together with the definition

$$P_i = \frac{\lambda^{1/2}(M_i^2, M_{i-1}^2, m_i^2)}{2M_i} \quad (\text{C.15})$$

this yields the recursion relation

$$R_n = \frac{1}{2M_n} \int dM_{n-1} d\Omega_{n-1} \frac{1}{2} P_n \dots \int dM_2 d\Omega_2 \frac{1}{2} P_3 \int d\Omega_1 \frac{1}{2} P_2. \quad (\text{C.16})$$

P_i corresponds to the absolute value of the spatial momentum of the particles with four momentum p_i and k_{i-1} in the rest system of the particle with four momentum k_i . The bounds of the integration over the invariant mass of the intermediate particles dM_i are given by

$$m_1 + \dots + m_i \leq M_i \leq M_{i+1} - m_{i+1}. \quad (\text{C.17})$$

The recursion relation (C.16) replaces the $(3n-4)$ -dimensional integration over four momenta by an integration over $(n-2)$ invariant masses $dM_{n-1} \dots dM_2$ and $(n-1)$ solid angles $d\Omega_{n-1} \dots d\Omega_1$. The angles ϑ_i and φ_i of $d\Omega_i$ define the direction of the spatial momenta \vec{k}_i and p_{i+1} in the rest system of the particle with four momentum k_{i+1} .

Bibliography

- [1] U. Dreyer, T. Baier, K. Hencken, and D. Trautmann. Lepton-pair production from deep inelastic scattering in peripheral relativistic heavy ion collisions. *Eur. Phys. J. C*, 45, 2006.
- [2] U. Dreyer et al. Testing the Electroweak Gauge Boson Coupling in Exclusive Photoproduction of Single W Bosons at the LHC. to be published, 2007.
- [3] G. Baur et al. Hot Topics in Ultra-Peripheral Ion Collisions. In *Erice 2001, Electromagnetic probes of fundamental physics*, 2002.
- [4] C. A. Bertulani, S. R. Klein, and J. Nystrand. Physics of Ultra-Peripheral Nuclear Collisions. *Ann. Rev. Nucl. Part. Sci.*, 55, 2005.
- [5] L. D. Landau and E. M. Lifshitz. The production of electrons and positrons by a collision of two particles. *Phys. Z. Sowjetunion*, 6, 1934.
- [6] G. Racah. Sulla simmetria tra particelle e antiparticelle. *Nuovo Cim.*, 14, 1937.
- [7] A. Alscher, K. Hencken, D. Trautmann, and G. Baur. Multiple electromagnetic electron positron pair production in relativistic heavy ion collisions. *Phys. Rev. A*, 55, 1997.
- [8] G. Baur et al. Coherent $\gamma\gamma$ and γA interactions in very peripheral collisions at relativistic ion colliders. *Phys. Rept.*, 364, 2002.
- [9] U. Baur and D. Zeppenfeld. Measuring the $WW\gamma$ vertex in single W production at ep colliders. *Nucl. Phys. B*, 325, 1989.
- [10] U. Baur, J. A. M. Vermaseren, and D. Zeppenfeld. Electroweak vector boson production in high-energy ep collisions. *Nucl. Phys. B*, 375, 1992.
- [11] J. Breitweg et al. W production and the search for events with an isolated high-energy lepton and missing transverse momentum at HERA. *Phys. Lett. B*, 471, 2000.
- [12] K. Piotrkowski. High energy photon interactions at the LHC. In *Photoproduction at collider energies: From RHIC and HERA to the LHC*, 2007.
- [13] H. W. Fearing, M. Patrap, and J. Smith. Spin-One W Boson Production via Muon Beams. *Phys. Rev. D*, 5, 1972.
- [14] H. W. Fearing, M. Patrap, and J. Smith. Photoproduction of Single Spin-One W Bosons at High Energies. *Phys. Rev. D*, 5, 1972.
- [15] E. Byckling and K. Kajantie. *Particle Kinematics*. John Wiley & sons, 1973.

- [16] J. D. Bjorken and S. D. Drell. *Relativistische Quantenmechanik*. B. I. Hochschultaschenbücher, 1966.
- [17] D. Griffiths. *Einführung in die Elementarteilchenphysik*. Akademie Verlag, 1996.
- [18] O. Nachtmann. *Elementarteilchenphysik - Phänomene und Konzepte*. Vieweg Verlag, 1991.
- [19] F. Halzen and A. D. Martin. *Quarks & Leptons*. John Wiley & sons, 1984.
- [20] A. W. Thomas and W. Weise. *The Structure of the Nucleon*. Wiley-VHC, 2001.
- [21] J. D. Bjorken. Asymptotic Sum Rules at Infinite Momentum. *Phys. Rev.*, 179, 1969.
- [22] E. D. Bloom et al. High-Energy Inelastic e-p Scattering at 6^0 and 10^0 . *Phys. Rev. Lett.*, 23, 1969.
- [23] M. Breidenbach et al. Observed Behavior of Highly Inelastic Electron-Proton Scattering. *Phys. Rev. Lett.*, 23, 1969.
- [24] R. D. Field and R. P. Feynman. Quark elastic scattering as a source of high-transverse-momentum mesons. *Phys. Rev. D*, 15, 1977.
- [25] G. Sterman et al. Handbook of perturbative QCD. *Rev. Mod. Phys.*, 67, 1995.
- [26] J. Pumplin et al. New Generation of Parton Distributions with Uncertainties from Global QCD Analysis. arXiv: hep-ph/0201195v3.
- [27] Y.-S. Tsai. Pair production and bremsstrahlung of charged leptons. *Rev. Mod. Phys.*, 46, 1974.
- [28] K. Hencken, D. Trautmann, and G. Baur. Photon-Photon luminosities in relativistic heavy ion collisions at LHC energies. *Z. Phys. C*, 68, 1995.
- [29] G. Piller and W. Weise. Nuclear Deep-Inelastic Lepton Scattering and Coherence Phenomena. *Phys. Rept.*, 330, 2000.
- [30] N. Armesto. Nuclear shadowing. *J. Phys. G: Nucl. Part. Phys.*, 32, 2006.
- [31] L. Frankfurt, V. Guzey, and M. Strikman. Leading twist nuclear shadowing: uncertainties, comparison to experiments and higher twist effects. *Phys. Rev. D*, 71, 2003.
- [32] L. Frankfurt, V. Guzey, M. McDermott, and M. Strikman. Nuclear shadowing in deep inelastic scattering on nuclei: Leading twist versus eikonal approaches. *JHEP*, 0202, 2002.
- [33] K. J. Eskola, V. J. Kolhinen, and C. A. Salgado. The scale dependent nuclear effects in parton distributions for practical applications. *Eur. Phys. J. C*, 9, 1999.
- [34] K. J. Eskola, V. J. Kolhinen, and P. V. Ruuskanen. Scale evolution of nuclear parton distributions. *Nucl. Phys. B*, 1998.
- [35] R. G. Roberts. *The Structure of the Proton - Deep Inelastic Scattering*. Cambridge University Press, 1990.
- [36] N. J. Baker et al. Quasielastic neutrino scattering: A measurement of the weak nucleon axial-vector form factor. *Phys. Rev. D*, 23, 1981.
- [37] W. A. Mann et al. Study of the Reaction $\nu + n \rightarrow \mu^- + p$. *Phys. Rev. Lett.*, 31, 1973.
- [38] Miller et al. Study of the reaction $\nu_\mu d \rightarrow \mu^- pp_s$. *Phys. Rev. D*, 26, 1982.

- [39] Choi et al. Axial and Pseudoscalar Nucleon Form Factors from Low Energy Pion Electroproduction. *Phys. Rev. Lett.*, 71, 1993.
- [40] E. Fermi. On the Theory of the impact between atoms and electrically charged particles (In German). *Z. Phys.*, 29, 1924.
- [41] E. J. Williams. Nature of the high-energy particles of penetrating radiation and status of ionization and radiation formulae. *Phys. Rev.*, 45, 1934.
- [42] C. F. von Weizsäcker. Radiation emitted in collisions of very fast electrons. *Z. Phys.*, 88, 1934.
- [43] A. J. Finch, editor. *PHOTON 2000: International Conference on the Structure and Interactions of the Photon*, 2000.
- [44] M. E. Peskin and D. V. Schroeder. *An Introduction to Quantum Field Theory*. Westview Press, 1995.
- [45] V. N. Baier, V. S. Fadin, and V. H. Khoze. Quasireal electron method in high-energy quantum electrodynamics. *Nucl. Phys. B*, 65, 1973.
- [46] M. Chen and P. Zerwas. Equivalent - Particle Approximations In Electron And Photon Processes Of Higher Order QED. *Phys. Rev. D*, 12, 1975.
- [47] V. M. Budnev, I. F. Ginzburg, G. V. Meledin, and V. G. Serbo. The Two photon particle production mechanism. Physical problems. Applications. Equivalent photon approximation. *Phys. Rept.*, 15, 1974.
- [48] J. D. Jackson. *Classical Electrodynamics*. John Wiley & sons, 1998.
- [49] M. Vidović, M. Greiner, C. Best, and G. Soff. Impact-parameter dependence of the electromagnetic particle production in ultrarelativistic heavy-ion collisions. *Phys. Rev. C*, 47, 1993.
- [50] B. Kniehl. Elastic e p scattering and the Weizsacker-Williams approximation. *Phys. Lett. B*, 254, 1991.
- [51] C. Pisano. Testing the Equivalent Photon Approximation of the Proton in the Process $ep \rightarrow \nu WX$. *Eur. Phys. J. C*, 38, 2004.
- [52] G. Baur and A. Leuschner. Bethe-Heitler cross section for very high photon energies and large muon scattering angles. *Eur. Phys. J. C*, 8, 1999.
- [53] C. A. Bertulani and G. Baur. Electromagnetic Processes in Relativistic Heavy Ion Collisions. *Phys. Rept.*, 163, 1988.
- [54] S. D. Drell and J. D. Walecka. Electrodynamical processes with nuclear targets. *Ann. Phys.*, 28, 1964.
- [55] www.phys.psu.edu/~cteq.
- [56] K. J. Kallianpur. High-energy Photoproduction of W Bosons. *Phys. Rev. D*, 34, 1936.
- [57] T. D. Lee and C. N. Yang. Theory of Charged Vector Mesons Interacting with the Electromagnetic Field. *Phys. Rev. D*, 128, 1962.
- [58] F. A. Berends and G. B. West. Gauge Invariance and the Born Approximation in Pion Electroproduction. *Phys. Rev.*, 188, 1969.

-
- [59] A. M. Bincer. Electromagnetic Structure of the Nucleon. *Phys. Rev.*, 118, 1960.
- [60] S. D. Drell and H. R. Pagels. Anomalous Magnetic Moment of the Electron, Muon, and Nucleon. *Phys. Rev.*, 140, 1965.
- [61] Y. Takahashi. On the generalized Ward identity. *Nuovo Cim.*, 6, 1957.
- [62] G. P. Lepage. Vegas: An Adaptive Multidimensional Integration Program. *J. Comp. Phys.*, 27, 1978.
- [63] W. J. Press. *Numerical Recipes in Fortran 77*. Cambridge University Press, 1986.
- [64] R. Assmann et al. Measurement of the relative luminosity at the LHC. Functional specification, CERN, 2003.
- [65] W. Beenakker, F. A. Berends, and A. P. Chapovsky. Radiative Corrections to Pair Production of Unstable Particles: Results for $e^+e^- \rightarrow 4$ fermions. *Nucl. Phys. B*, 548, 1999.
- [66] Grabmayr et al. Proposal to measure the total photoabsorption cross section of ${}^{6,7}\text{Li}$ below π -threshold. 2004.
- [67] J. Ahrens et al. Total Nuclear Photon Absorption Cross Sections for some Light Elements. *Nucl. Phys. A*, 251, 1975.
- [68] S. Jadach. Practical Guide to Monte Carlo.
- [69] J. Schnakenberg. *Algorithmen in der Quantentheorie und Statistischen Physik*. Verlag Zimmermann-Neufang, 1995.
- [70] F. Salvat et al. Analytical Dirac-Hartree-Fock-Slater screening function for atoms. *Phys. Rev. A*, 36, 1987.
- [71] W. Greiner and A. Schäfer. *Quantenelektrodynamik*. Harri Deutsch, 1989.
- [72] J. H. Hubbell, H. A. Gimm, and I. Overbo. Pair, Triplet, and Total Atomic Cross Sections (and Mass Attenuation Coefficients) for 1MeV-100GeV Photons in Elements $Z=1-100$. *J. Phys. Chem. Ref. Data*, 9, 1980.
- [73] P. L. DeVries. *A First Course in Computational Physics*. John Wiley & sons, 1994.

Curriculum Vitae

Ute Dreyer

14. März 1979	Geboren in Lörrach, Deutschland
09/1989 – 06/1998	Hans-Thoma Gymnasium Lörrach
06/1998	Abitur
10/1998 – 07/2003	Studium an der Universität Basel Hauptfach: Physik Nebenfächer: Mathematik und Astronomie
10/2000	Vordiplom in Physik
11/2002-07/2003	Diplomarbeit über "Paarproduktion durch Zwei-Photon-Prozesse in elastischer und inelastischer Streuung" unter der Anleitung von PD Dr. K. Hencken und Prof. Dr. D. Trautmann
07/2003	Diplom in Theoretischer Physik
seit 10/2003	Dissertation am Institut für Physik an der Universität Basel in der Gruppe von Prof. Dr. D. Trautmann

Meine Ausbildung verdanke ich den folgenden Dozentinnen und Dozenten:

Prof. Dr. C. Bandle, Prof. Dr. G. Baur, Prof. Dr. W. Belzig, Prof. Dr. R. Bennewitz, Prof. Dr. B. Binggeli, Prof. Dr. C. Bruder, Prof. Dr. H. Burkhardt, Prof. Dr. R. Buser, PD Dr. A. Bussmann-Holder, Dr. T. Christen, Prof. Dr. O. Gerhard, Prof. Dr. M. Grote, Dr. T. Gyalog, PD Dr. K. Hencken, Prof. Dr. H.-J. Hug, Dr. M. Kassmann, PD Dr. E. Kolbe, Prof. Dr. H. Kraft, Prof. Dr. D. Loss, Prof. Dr. D. Masser, Prof. Dr. E. Meyer, PD Dr. H. Mühry, Prof. Dr. G.-R. Plattner, Prof. Dr. W. Reichel, Prof. Dr. C. Schönenberger, Prof. Dr. I. Sick, Prof. Dr. G. Tammann, Prof. Dr. L. Tauscher, Prof. Dr. F.-K. Thielemann, Prof. Dr. D. Trautmann, sowie den Dozenten des Internationalen Graduiertenkollegs Basel-Tübingen-Graz

Acknowledgements

At this point I would like to thank all the people who contributed - directly or indirectly - to the completion of this thesis. In particular, I want to thank the following people:

- PD Dr. Kai Hencken for initiating the studies presented in this thesis and for constant support, advice, and stimulating discussions through the years of my doctoral studies. I am very grateful for this. Furthermore, I want to thank him for reviewing this and several other manuscripts.
- Prof. Dr. Dirk Trautmann for giving me the opportunity to join his group and to work on the projects presented in this thesis and for creating a friendly and relaxed working atmosphere.
- Prof. Dr. Gerhard Baur for agreeing to act as second examiner of this thesis, for his kindness, and for inviting me to join the Workshop on "Photoproduction at Collider Energies: from RHIC and HERA to the LHC" in Trento in January 2007, which was very inspiring and motivating.
- My present and former colleagues in the group, especially those I shared an office with.
- Astrid Kalt and Barbara Kammermann for being always very kind and helpful.
- Carla, Stuart, and Patrick for reading and commenting on parts of this thesis.
- Andreas, Carla, Darko, Florian, Fred, Jan, Kai, Lars, Luca, Oded, Oli, Roman, Sabine, Sarah, Stuart, and many more for entertainment and discussions in and around the Institute.
- Angelo and Stephan for the "unisport - brain support"
- Carla, Darko, Hannes, Martina, Philipp, Primo, and Sabine for their friendship over many years and for making life worthwhile.
- My parents for their faith, trust, and loving support.
- The rest of my family for the family parties and the holidays in Saas Fee, which I enjoyed a lot.
- Patrick for his love and seemingly endless patience.

